THE UNIVERSITY OF QUEENSLAND

AUSTRALIA

Modelling of Cavity Optomechanical Magnetometers

Yimin Yu

M. Sc., Karlsruhe Institute of Technology, 2013

M.Sc., Aix Marseille University, 2013

A thesis submitted for the degree Master of Philosophy at

The University of Queensland in 2017

School of Mathematics and Physics

Abstract

Precision magnetometers are widely used in our daily life such as in aircraft navigation, space applications, magnetoencephalography, studies of topological spin configurations, and nuclear magnetic resonance spectroscopy. Magnetometers with optical readout have the advantage of inducing minimal electromagnetic interference in the specimen to be measured. Micro cavity optomechanical magnetic field magnetometers, as a type of miniaturized optical magnetometer developed in our group, is made from the magnetostrictive material Terfenol-D surrounded by a micro toroidal optical cavity operated at room temperature. It converts the magnetic field into stress, thus deforming the magnetostrictive material. The minuscule mechanical deformation can be precisely read out by using an optical cavity attached to it and monitoring the shift of the optical resonance frequency. Such magnetometers have tens of micro-metre lateral and longitudinal sizes, outstanding sensitivity performances, broad bandwidths, large dynamic ranges and a simple operating scheme. The latest experimental result shows that the sensitivity is even competitive to superconducting quantum interference devices of similar sizes which are operated in cryogenic temperature.

In this thesis, I develop a general recipe for predicting the magnetic field sensitivity and bandwidth of magnetostrictive material based cavity optomechanical magnetometry, thus building a bridge connecting to previous experimental results and allowing prediction for future designs of sensors with improved performance. Magnetostrictive nature of the material, displaying a relation between stress and external magnetic field, is added as an external stress tensor term in the elastic wave equation to the intrinsic elasticity term which describes the stress-strain relation without external driving. Finite element analysis is used to solve the modified elastic wave equation numerically, the results of which are then combined with optomechanical analysis to obtain predictions of the sensitivity and bandwidth, limited by the combination of thermal Brownian noise excited at room temperature and laser shot noise. The calculations are performed with several structures with a highest predicted sensitivity of 5 $\mathrm{pT}/\sqrt{\mathrm{Hz}}$ limited by thermal Brownian noise, and a 3 dB bandwidth of a few MHz, which is in good agreement with previous experimental observations, yet demonstrating the potential for improvement. By adjusting Terfenol-Ds' composition and its annealing process, sensitivity as good as 500 $\mathrm{fT}/\sqrt{\mathrm{Hz}}$ maybe possible. The method paves a way for future design of magnetostrictive material based magnetometers, possibly allowing both scalar and vectorial magnetometry.

Declaration by author

This thesis is composed of my original work, and contains no material previously published or written by another person except where due reference has been made in the text. I have clearly stated the contribution by others to jointly-authored works that I have included in my thesis.

I have clearly stated the contribution of others to my thesis as a whole, including statistical assistance, survey design, data analysis, significant technical procedures, professional editorial advice, and any other original research work used or reported in my thesis. The content of my thesis is the result of work I have carried out since the commencement of my research higher degree candidature and does not include a substantial part of work that has been submitted to qualify for the award of any other degree or diploma in any university or other tertiary institution. I have clearly stated which parts of my thesis, if any, have been submitted to qualify for another award.

I acknowledge that an electronic copy of my thesis must be lodged with the University Library and, subject to the policy and procedures of The University of Queensland, the thesis be made available for research and study in accordance with the Copyright Act 1968 unless a period of embargo has been approved by the Dean of the Graduate School.

I acknowledge that copyright of all material contained in my thesis resides with the copyright holder(s) of that material. Where appropriate I have obtained copyright permission from the copyright holder to reproduce material in this thesis.

Publications during candidature

No publications.

Publications included in this thesis

No publications.

Contributions by others to the thesis

My supervisors Prof. Warwick P. Bowen and Prof. Halina Rubinsztein-Dunlop have provided support in the conception and the design of the project, analysis and interpretation of data as well as technical support and revision of written material.

Statement of parts of the thesis submitted to qualify for the award of another degree

None

Acknowledgements

I would like to extend my foremost thanks to my primary supervisor Prof. Warwick Bowen for giving me the opportunity to work in the Queensland quantum optics lab. He gives me the research freedom to explore what I am interested in while carefully working me with his excellent guidance and supervision. I have greatly benefited from his guiding into the exciting realm of cavity optomechanics and insight into problems encountered. I also enjoy the friendly group environment created by Warwick where numerous activities have taken place ranging from gastronomical competition to cricket BBQ events.

Next, I would like to thank my associate supervisor Prof. Halina Rubinsztein-Dunlop for her willingness to help and her patient explanations, as well as the interesting discussion during the weekly group meetings and the modification of the thesis, despite her amazingly busy broad coverage of other work.

I am grateful to all the colleagues who produced fruitful discussions for the work in this thesis. Thanks to Chris Baker for introducing me to the use of COMSOL, Kiran Khosla for clear pedagogical explaining spin 2-level system for me, Stefan Forstner for sharing the experience of magnetometry and George Brawley for helping me catch up on the basics of quantum optics by sacrificing a considerable amount of time from him. I also wound like to thank Etrema Inc., James Bennent, Glen Harris, David McAuslan, Nick Wyatt, Michael Taylor, Bei-Bei Li and Varun Prakash for relevant useful discussions.

The fantastic seminars, workshops and winter schools provided by the Australian Research Council Centre of Excellence for Engineered Quantum Systems (EQuS) are truly memorable, thanks to those who equipped me with the knowledge to make the attendance more enjoyable. Special thanks go to the Advanced Quantum Theory lecture team: Matt Davis, Gerard Milburn and Clemens Mueller, as well as to Sahar Basiri Esfahani, Joshua Combes and Nariman Saadatmand.

Further appreciation goes to administrative staffs: Kaerin Gardiner, Angela Bird, Ruth Forrest, Tara Massingham, Joyce Wang, Poonam Kalwar, Lisa Provoroff and Lisa Walk for their kindness and for quickly sorting out paper works. Particularly, a thank to the postgraduate admin officer in the School of Mathematics and Physics Muray Kane for his willingness and persistence in assisting postgraduates.

Besides, thanks to Gondwana rainforests, Great Barrier Reefs and UQ sports for refreshment and all the friends I've made there.

Last but not the least, thanks for the reliable help throughout from my family who are unyieldingly persistent in witnessing the birth of the thesis.

Keywords

Magnetometer, Cavity optomechanics, Magnetostriction, Finite element

Australian and New Zealand Standard Research Classifications (ANZSRC)

ANZSRC code: 020501 Classical and Physical Optics, 20%
ANZSRC code: 020604 Quantum Optics, 20%
ANZSRC code: 091307 Numerical Modelling and Mechanical Characterisation, 60%

Fields of Research (FoR) Classification

FoR code: 0205, Optical Physics, 20%
FoR code: 0206, Quantum Physics, 20%
FoR code: 0913, Mechanical Engineering, 60%

Table of contents

List of Figures **ix**

List of Tables **xiii**

Symbols **xv**

1 Introduction **1**
1.1 State of the art of miniaturized magnetometry 1
1.2 Basics of cavity optomechanical magnetometry 2
1.3 Previous numerical modelling 3
1.4 Introduction of this thesis 4

2 Optomechanical Analysis for Magnetometry **7**
2.1 System of the optomechanical field magnetometry 7
2.2 Interplay between mechanical motion and optical field 8
2.3 Direct and homodyne detection techniques 11
2.4 Power spectral density with and without laser detuning 13
2.5 Network response for exciting external magnetic field 16

3 Mechanical Properties of Optomechanical Magnetometry from Numerical Simulation **19**
3.1 Time domain structural dynamics 19
3.2 Modelling magnetostrictive material 22
3.3 Damping selection in COMSOL 25
3.4 Magnetic field 27
3.5 Obtaining actuation constant 30
3.6 Towards obtaining the optomechanical coupling strength 32
3.7 Magnetomechanical coupling 36

4 Numerical Prediction of Bandwidth and Sensitivity **41**
4.1 Single mechanical mode analysis 41
4.2 Multiple mechanical modes analysis 45
4.3 The effects of laser detuning and power on bandwidth 48

5 Conclusion and Outlook **51**
5.1 Conclusion 51

5.2 Outlook 51

References **53**

Appendix A: Input parameters and variables to COMSOL **59**

Appendix B: Magnetic Field Inside Magnets **61**

List of Figures

1.1 **Simplified cavity optomechanical magnetometry concept** illustrated by a Fabry-Pérot type optical resonator. 3

1.2 **State-of-the-art miniaturized magnetometers** mentioned in the text is presented as sensitivity vs. lateral size. This numerical work of cavity optomechanical magnetometry is highlighted with red hollow square compared with all other experimental works listed in the text [32, 9–11, 13, 16, 15, 22, 17]. 5

2.1 **Cavity optomechanics concept illustrated by a Fabry-Pérot resonator.** 7

2.2 **Simplest Homodyne detection scheme. a)** The device under test is immersed in magnetic field shown as $\times$ symbol perpendicular to the plane. **b)** An artistic view of a magnetometer being coupled to an optical fibre via an evanescent optical field. . . . 12

3.1 **A pair of Helmholtz coils for generating reference magnetic field.** The intensity of the magnetic field is viewed by colormap projected on three orthogonal slices. As an example, the AC magnetic field is driven by AC current at 7.4 MHz in z direction. The micro device at the center of the intersection of the slices is around 16 times smaller than the coils' diameter. 28

3.2 **Skin depth vs. the frequency of the reference driving magnetic field.** 28

3.3 **Cross-sectional view of magnetometers following ref. [26, 27].** Here the Terfenol-D is modelled as a smooth semi-ellipsoid or an ellipsoid. 29

3.4 **The effect of eddy current on magnetometers of two geometries as sketched in Fig. 3.3a)-b).** The external magnetic field of a)-c) modulates in y direction (the axis of the pair of Helmholtz coils aligns in y direction), while that of d)-f) is in z direction. The magnetic field intensity is viewed by orthonormal slices same as in Fig. 3.1. . . . 29

3.5 **Phase spectrum across mechanical resonances extracted from COMSOL.** At the exact mechanical resonance frequency, the phase is either 90^{o} or -90^{o}. The left plot shows two mechanical resonances while the right one is zoomed into one of the resonances. Proper damping is added to prevent extreme narrow linewidth at the mechanical resonance frequencies. 32

3.6 **Real and absolute value of the displacement based on COMSOLs' phase spectrum. a)** Phase spectrum extracted from COMSOL across a mechanical resonance. **b)** Real and absolute amplitude of the maximum displacement extracted from COMSOL. **c)** Analytical reproducing of the phase spectrum and **d)** the corresponding real and absolute displacement. 33

3.7 **a)-c)Typical Lorentzian fits for mechanical equation of motion with increasing input damping parameters.** The input damping parameter in **b)** is 12.5 times larger than in **a)**, and that of in **c)** is 12500 times larger than in **a)**. **d)-f) Quadratic and linear $\xi(2\Omega_M)$ and $\xi(\Omega_M)$ with increasing input damping. d), e), f)** has the same input damping as **a), b), c)**, respectively. The smaller the damping, the larger the quadratic effect, while the linear rate is constant. In extremely large damping case as displayed in **f)**, some numerical error may be responsible for the unusual ξ value. The mechanical mode used in this analysis has the shape shown in the **b)** inset with scaling factor $\gg 1$ for the displacement. 34
3.8 **The relationship between cavity length change and the optical resonance frequency shift illustrated via a Fabry-Pérot resonator.** 35
3.9 **COMSOL synchronization mechanism within a mechanical resonance.** For frequencies lower than the resonance frequency, the maximum displacement within a period of harmonic oscillation is synchronized to the positive maximum amplitude, while for frequencies higher than the resonance frequency, the amplitudes of which are synchronized to the negative maximum amplitude. The splitting of the synchronization can be understood by the splitting of phase spectrum on resonance as shown in Fig. 3.5. The text explanation is prepared for Fig. 3.7 d)-f). 35
3.10 **COMSOL layout of a pair of Helmholtz coils which can rotate freely.** Examples show the ability of coils to produce magnetic field in y, $y-z$ and z directions. The outermost spheres is created to be filled with air to support the generation of magnetic field in COMSOL. The centre spots are the devices under test. 37
3.11 **Spatial shapes of the mechanical RBMs and rugby-ball modes. a)** Rugby-ball modes and **b)** a radial breathing mode from the Terfenol-D modelled as transversely isotropic material. **c)** A RBM and **d)** rugby-ball modes modelled as isotropic material with Young's Modulus of 30 GPa, density of 9250 kg/m^3 and Poisson's ratio of 0.25. A material with isotropic modelling exhibits more degenerated modes for the rugby-ball mode. The black dotted lines indicate mode shape oscillations at mechanical eigenmodes. From left to right the frequency of the mechanical eigenmodes increases. 38

4.1 **Single mechanical mode analysis** for **a)** the sensitivity and **b)** the vacuum optomechanical coupling rate in the presence of Terfenol-D position offset. **c)** An illustration of the 1st generation optomechanical magnetometer with the evolution of Terfenol-Ds' position. **d)** Actuation constant and noise contributions from **e)** thermal bath, **f)** back-action and **g)** measurement imprecision for the degeneracy-lifted two 2nd order crown modes. Inset between **a)** and **b)** is the spatial profile induced by the reference magnetic field. 42
4.2 **Single mechanical mode analysis for sensitivity as a function of the radius of the Terfenol-D** 44

4.3 **Sensitivity spectrum prediction for the 1st generation magnetometers.** **a)**Top: thermal noise spectral density $S_{\Omega\Omega}(\Omega)$ (blue) is the sum of individual thermal noise peaks (grey) and the normalized (to optical zero-point motion) laser shot noise (red). Middle: network response $N^{\mathrm{BB}}_{\Omega\Omega}$ records the magnetomechanical coupling under in-plane reference magnetic field driving. Bottom: black triangle is the sensitivity for individual mechanical modes. **b)** Thermal noise spectral density shows the first five mechanical modes are not buried under the silica RBM at 42.7 MHz. **c)** Actuation constant, **d)** vacuum optomechanical coupling rate, **e)** cooperativity and effective cooperativity of each individual mechanical eigenmodes. **f)** Mechanical eigenmodes without Terfenol-D offset from left to right corresponding to eigenfrequencies from low to high. 46

4.4 **Thermal noise spectral density, network response and sensitivity for the 2nd generation magnetometers** driven by an in-plane **a)-d)** and axial **e)-h)** reference magnetic field with cooperativity, vacuum optomechanical coupling rate and actuation constant on mechanical resonances of interest. An art view of the cross section is shown in **e)** inset for the 2nd generation magnetometers [27]. 47

4.5 **The effect of laser detuning from optical cavity and power on bandwidth and sensitivity** Dots with blue edges represent for cooling with the red detuned factor $\Delta = \kappa$, while red edges of those are for heating effect when the laser is blue detuned $\Delta = -\kappa$. Input laser power larger than 20 μW would cause instability due to heating effects. Locking the laser on optical resonance frequency with the input power 5 times smaller than in the detuning $\Delta = \pm\kappa$ cases results the same bandwidth increasing trend as shown in the inset. 49

1 **Magnetic field inside a magnet rod using textbook toy models of magnetic current and magnetic dipole.** After applying an external magnetic field B_0 from a current flowing solenoid, **(a)** the aligned magnetic current ensemble shows a total effect equivalent to circular current around the edge (a thin line in the middle) in the magnetic current model. **(b)** In the magnetic dipole model, the total effect of applying $\boldsymbol{B}_0$ is equal to creating negative and positive magnetic charges on the left and right side surfaces of the magnet. 61

2 **The calculation scheme of the magnetic field in the axial direction of a single current loop and solenoid. a)** The current at position A creates a magnetic field d$\boldsymbol{B}$ at the location • on the horizontal axis. The current in a single loop generates a magnetic field $\delta\boldsymbol{B}$. **b)** The direction of the magnetic field d$\boldsymbol{B}$ is clarified where the single current loop is viewed from a front angle. Note that the scale of the red loop shrinks a bit. **c)** A solenoid is modelled as as array of single current loops along the axial direction. The array produces a magnetic field $\boldsymbol{B}$ on the axis x distance away. 62

3 **Magnetic field in the axial direction of a magnetically charge circular plate.** . . 64

List of Tables

3.1 **Coefficients in the magneto-mechanical coupling** [56] 24
3.2 **Fitted parameters with damping for Fig. 3.7 a)-c)** 31
3.3 **Magnetomechanical coupling.** Maximum displacement amplitude as response to the variation of reference external magnetic field direction for transversely isotropic modelling of Terfenol-D. 37

1 **Input global parameters to COMSOL** 59
2 **Input variables to COMSOL** 59

Symbols

Roman Symbols

3D	three dimension/al
c_{act}	magnetic actuation constant (N/T)
C_{eff}	effective cooperativity
CW/CCW	clockwise/counter-clockwise
$\overline{\overline{\boldsymbol{d}}}$	piezomagnetic matrix constant (m/A)
$\overline{\overline{\boldsymbol{e}}}^{\varepsilon}$	$=[\overline{\overline{\boldsymbol{s}}}^{\text{H}}]^{-1} \cdot \overline{\overline{\boldsymbol{d}}}$ (T)
F_{field}	force generated by the magnetic field on the magnetostrictive material $F_{\text{field}} = c_{act}B$, sometimes also termed as F_{sig} (N)
G	optomechanical coupling strength (rad·s^{-1}·m^{-1})
g_0	vacuum (single photon) optomechanical coupling rate (rad·s^{-1})
L	circumference (m)
m_{eff}	effective mass (kg)
N	intra-cavity photon number
N_{in}	input photon number (s^{-1})
$\hat{P}/\hat{Q}$	dimensionless mechanical operator in amplitude/phase quadrature
Q	quality factor
$\overline{\overline{\boldsymbol{s}}}^{\text{H}}$	elastic compliance (Pa^{-1})
$\bar{S}_{XX}$	symmetrized noise spectrum of quantity X
$\bar{S}_{XX}^{BB}$	symmetrized magnetic field signal spectrum of quantity X
T	sample temperature (K)
$\boldsymbol{u}$	displacement in 3 dimension (m)

$\hat{X}/\hat{Y}$ dimensionless optical operator in amplitude/phase quadrature

Greek Symbols

χ mechanical susceptibility

Δ laser detuning $\Delta = \omega_0 - \omega_L$ (rad·s^{-1})

η coupling efficiency

Γ mechanical decay rate (rad·s^{-1})

κ optical decay rate (rad·s^{-1})

$\overline{\overline{\boldsymbol{\lambda}}}^{\mathrm{H}}$ elasticity matrix element under constant magnetic field H (Pa)

$\hat{\mathcal{O}}$ arbitrary system operator

ω_0 optical cavity resonance frequency (rad·s^{-1})

ω_L laser frequency (rad·s^{-1})

Ω_{M} mechanical eigen frequency (rad·s^{-1})

ε mechanical strain

σ mechanical stress (Pa)

ξ the ratio of change of circumference to maximum displacement

Other Symbols

COMSOL a commercial finite element software

Y quadrature Light phase quadrature

Acronyms / Abbreviations

AC Alternating current

BEC Bose-Einstein condensates

DC Direct current

MRFM Magnetic resonance force microscope

NMR Nuclear magnetic resonance

NV nitrogen-vacancy

RBM Radial breathing mode

RBW Resolution bandwidth

SNR Signal-to-noise ratio

SQUID Superconducting quantum interference device

Terfenol – D Magnetostrictive material consists of Tb_xDy_1-xFe_2 (x $\sim$0.3) developed by Naval Ordnance Laboratory (nol) in United States

Chapter 1

Introduction

Precision magnetometers are widely used for aircraft navigation [1], mapping earth's magnetic field and magnetic-based attitude control system in space [2], magnetoencephalography [3], studies of topological spin configurations [4], nuclear magnetic resonance (NMR) spectroscopy etc. NMR techniques can further find applications including identifying chemical composition, molecular structure and dynamics [5], quantum control and computations [6].

1.1 State of the art of miniaturized magnetometry

The sensitivity of the magnetometers scales with size. For instance, the magnetic field noise of superconducting quantum interference devices (SQUIDs) is inversely proportional to the effective flux capture area [7]. Though SQUIDs have the best magnetic flux sensitivity to date, developed in the 1970s the SQUID with 20 aT/$\sqrt{\text{Hz}}$ sensitivity is in a 70 cm long configuration for pick-up loop [8], which is quite bulky and massive.

Miniaturization and low power consumption requirement for magnetometers allows a range of applications such as space applications [2] for lighter loads and high spatial resolution characterization of magnetic materials. Much effort has been put into the miniaturizations in the magnetometers community while reaching good sensitivity.

Magnetometers with electronic readout enjoy a long history. Thin film Hall sensors with lateral size of 800 μm and magnetoresistive magnetometers with flux concentrator of lateral size 500 μm reach $\sim$100 pT/$\sqrt{\text{Hz}}$ sensitivity limited by thermal (or Johnson-Nyquist) noise ($>$1000 Hz) and empirical 1/f noise ($<$1000 Hz) [9, 10]. Miniaturized fluxgates have the sensitivity of sub-hundred pT/$\sqrt{\text{Hz}}$ for a cm array [11]. The sensitivity of an induction coil based magnetometer, boosted by a long ferromagnetic core, scales cubically with the sensors' longitudinal size [12]. Even disregarding the length and scaling a $5\times5\times150$ mm^3 coil sensor with a noise level 50 fT/$\sqrt{\text{Hz}}$ at frequencies larger than 1000 Hz [13] down to 100 μm lateral size gives a sensitivity of 10 nT/$\sqrt{\text{Hz}}$. SQUIDs consisting of two Josephson tunnel junctions and superconducting loops operate in cryogenic temperature. Miniaturization of SQUIDs into sub-micro size brings their application in thermal imaging of quantum system and detection of the momentum of a single electron spin [14]. Note that magnetic momentum sensors, measuring magnetization are a complementary counterpart of magnetic field magnetometer, have very good spatial resolution down to a few spins but are poor at field sensing. A SQUID whose pick-up loop

has a size of 40 μm without counting the millimetre long stripline connecting Josephson junctions and pick-up loop demonstrates a sensitivity of 40 pT/$\sqrt{\text{Hz}}$ [15]. Another three times larger SQUID with 120 μm size exhibits 1.4 pT/$\sqrt{\text{Hz}}$ sensitivity at 1000 Hz [16].

While electronic readout may interfere with the specimen through, for instance, undesired parasitic inductance and capacitance, optical readout is well decoupled from magnetic signal. Atomic vapours, ultracold Bose-Einstein condensates (BEC) magnetometry, nitrogen-vacancy (NV) defect center(s), magnetic resonance force microscope (MRFM) and optomechanical magnetometers use optical readout. Miniaturisation has brought the atomic vapour cell down to 1 mm with 5 fT/$\sqrt{\text{Hz}}$ sensitivity [17]. However, 200^{o}C of heating needs to be applied for an optimised atomic density. A single NV centres' exceptional nm spatial resolution enables it to be placed extremely close (nm scale) to the sample having detected NMR signals from a single electron spin [18], a single protein spin [19, 20] and individual proton spins [21]. However, the sensitivity of a single NV is limited, using an ensemble of NV centres sacrificing some spatial resolution to a volume size of $\sim 100^3$ m^3 pushes the sensitivity down to 1 pT/$\sqrt{\text{Hz}}$ [22]. In this way applications of NV centres are extended to the detection of the magnetic field from the electrical impulse conveying between neurons [23] and NMR spectroscopy of weak signals from small sample solutions of picoliter-volume [24]. However, the remarkable sensitivity of AC NV centres magnetometry is compensated by its narrow bandwidth, typically $\sim$ a few kHz. Small bandwidth limits the detection speed of the NMR spectroscopy. It is likely that multiple frequency spectra are needed to be examined before the fingerprint frequency region of the specimen is found. Furthermore, NV magnetometers need high optical power for excitation (e.g. 400 mW in ref. [22]) and complicated microwave decoupling sequences in NMR spectroscopy, and they are limited by the fabrication reproducibility [7]. DC NV magnetometers have a record bandwidth among NV magnetometers of 1.6 MHz with $\sim$ 5nT/$\sqrt{\text{Hz}}$ sensitivity limited by the available excitation laser power. The input laser power of 2.3 MW/cm^2 [25, 7] used in NV magnetometer is around 3 orders of magnitude larger than the detection laser power of standard optomechanical experiments [26–28]. MRFM [29] and optomechanical magnetization magnetometers [30] are sensitive to magnetization in nano and micro scale respectively, but not to magnetic field. Micro-sized BEC magnetometry has a quantum-enhanced sensitivity of 2 nT/$\sqrt{\text{Hz}}$ [31].

As an alternative, optomechanical field sensors developed in our group [32, 27, 26] are of μm size operated at room temperature. It has pT/$\sqrt{\text{Hz}}$ thermal noise limited sensitivity and is detected by a coherent laser with a few μW input power. This platform offers a simple operational scheme, low energy consumption, large bandwidth and extraordinary field sensitivity among micro-magnetometers. A sensitivity of 30 pT/$\sqrt{\text{Hz}}$ is achieved in the latest experiments [32] comparable to the best SQUIDs of the same orders of size.

1.2 Basics of cavity optomechanical magnetometry

Our optomechanical system consists of an optical cavity attached to a magnetostrictive material, whose shape deforms in response to the external magnetic field. If the frequency of the external magnetic field coincides with the mechanical resonances, the deformation would dramatically enhance. Thus, this type of magnetometer is very sensitive to AC magnetic field signal at mechanical resonance frequencies.

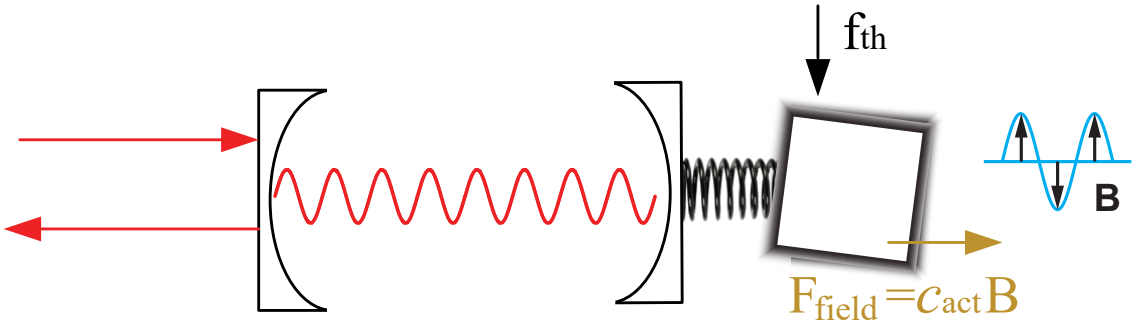

Fig. 1.1 **Simplified cavity optomechanical magnetometry concept** illustrated by a Fabry-Pérot type optical resonator.

Explained via an example of Fabry-Pérot type optical resonator in Fig. 1.1, the optical cavity couples to the magnetostrictive material through one-end-movable mirror. The magnetostrictive material exerts force $F_{\text{field}} = c_{act}B$ (c_{act} being the actuation constant) when immersed in a magnetic field environment to the end-movable mirror. How large c_{act} is depends on how good the magnetomechanical coupling mode describing the mode overlap between the spatial profile created by the F_{field} and the shape of mechanical eigenmodes is. At the same time, there exist noise sources that blur the motion driven by the magnetic field, the dominant noise for this room temperature system comes from thermal excitations. It is described by the equipartition theorem that each degree of freedom of an object has a mean energy of $k_bT/2$ (k_b is the Boltzmann constant and T is the temperature) in a finite temperature environment.

The modulation of the optical resonance frequency due to the change of the cavity length by the end mirror is read out at the front mirror where the input light launches.

Meanwhile, there is an another optomechanical system using magnetostrictive material [33]. In their scheme, the magnetostrictive YIG sphere is put inside a cavity. When driving with magnet field, the YIG sphere deforms thus disturbing the electromagnetic wave confined in the cavity. The readout is measured from the transmission and reflection of a microwave cavity. Their magnetomechanical coupling depends on how good the mode overlap of the spatial profile of the magnon oscillation excited by external magnetic field and the mechanical eigenmode of the YIG sphere is. As the magnetic field influences greatly on shifting the magnon oscillation frequency, the magnetomechanical coupling is magnetic field dependent. Compared with our system, the magnetomechanical coupling is constant within one mechanical eigenmode independent with magnetic field. Thus their system is good for hybridization of magnon and phonon as what has been demonstrated, but is not suitable for magnetometry.

1.3 Previous numerical modelling

Numerical modelling of optomechanical field magnetometry builds the bridge between past experimental results and future designs. Previous numerical modelling [34, 35] predicted the actuation constant c_{act} only at radial-breathing mode (RBM) of a piece of magnetostrictive material, which expands and

contracts ideally only in radial direction due to radial symmetry. It calculates the magnetomechanical coupling in multiple procedures: extracting the mechanical eigenmode profile along one direction (could be extended to a few directions) and then integrating it with a force vector derived from the magnetic field-induced longitudinal stress. This analytical mode-overlap calculation limits the mechanical eigenmode profile to radial symmetrical cases and stress induced spatial profile to only one dimension. Though it is sufficient to estimate the performance of radial-breathing mode, this half numerical and half analytic method is hard to extend to other mechanical eigenmodes. Furthermore, it consists of the piece of magnetostrictive material only, neglecting the optical cavity. Consequently, it overlooks the bending effect due to a bimetallic-strip like mechanism that makes the dominant contribution to the performance of the magnetometers in many configurations.

1.4 Introduction of this thesis

In the model developed here, we modifies the elastic wave equation which governs the linear oscillations of elastic media. The spatial mode overlap is intrinsically included in the elastic wave equation. A magnetostrictive term displaying the relation between stress and external magnetic field, is added as an external stress $\boldsymbol{\sigma}^{ext}$ in the elastic wave equation together with the elasticity stress without driving [36].

The elastic wave equation is solved in 3D numerically by Finite Element Analysis (FEA), using a commercial software package (COMSOL Multiphysics 5.2 Solid Mechanics module) with the input of a vectorial reference magnetic field producing the external stress $\boldsymbol{\sigma}^{ext}$. This model intrinsically includes the anisotropic nature of magnetostrictive materials. Originally coming from the magnetostrictive materials (Terfenol-D [37–43] and Galfenol [44–48]) based actuators and transducers community, this model is exploited by us by combining optomechanical analysis (see **Chapter 2**) with the study of the mechanical properties under the consideration of magnetomechanical coupling (see **Chapter 3**) to derive the sensitivity and bandwidth (see **Chapter 4**). The input parameters to the model are input laser power and empirical optical mechanical quality factors depending on the fabrication. Key mechanical properties include the magnetic actuation constant $c_{act}(\Omega_{\mathrm{M}})$ and geometrical-dependent $\xi(\Omega_{\mathrm{M}})$ parameter. In toroidal geometry as shown in Fig. 1.1c), $\xi(\Omega_{\mathrm{M}})$ is the ratio between the change of the outermost circumference equivalent to the optical path and the maximum displacement, and it quantifies the strength of the coupling of the motion of a given mechanical eigenmode to the optical field in the cavity. Theoretical analysis from the optomechanics community considers the presence of a thermal Langevin force and coherent laser noise under a homodyne detection scheme.

We apply this analysis to the previous experiment [32] predicting an optimal sensitivity of 5 $\mathrm{pT}/\sqrt{\mathrm{Hz}}$ around an order of magnitude better than the experiment results, showing a potential for improvement. We further study the effect of bending and the size of the magnetostrictive material on sensitivity, as well as the improvement of bandwidth as a result of laser detuning and increasing the power for different geometries. Numerical predictions are compared with miniaturized high performance magnetometers demonstrated experimentally in Fig. 1.2. This numerical model would help to specify the orientation of a sample to best boost the magnetomechanical coupling, thus amplifying the detected magnetic field signal for a scalar magnetometer; as well as characterizing the mechanical response with the variation of magnetic field direction allowing a vectorial magnetometer. More conclusions and outlook can be found in **Chapter 5**.

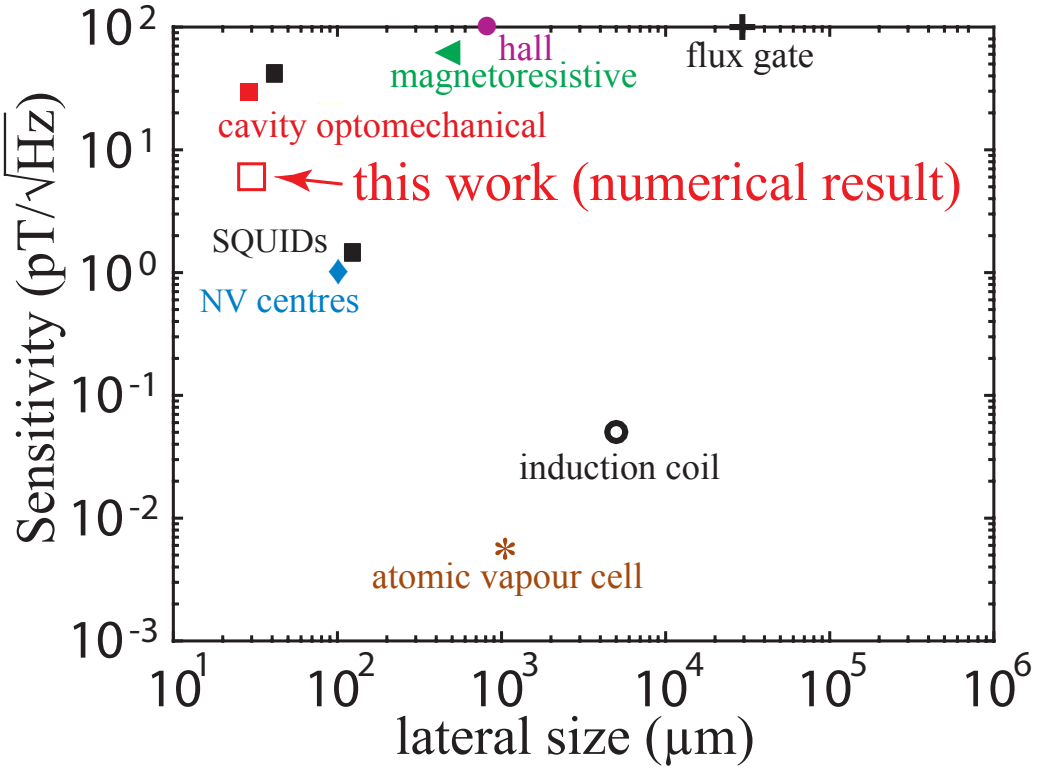

Fig. 1.2 **State-of-the-art miniaturized magnetometers** mentioned in the text is presented as sensitivity vs. lateral size. This numerical work of cavity optomechanical magnetometry is highlighted with red hollow square compared with all other experimental works listed in the text [32, 9–11, 13, 16, 15, 22, 17].

Chapter 2

Optomechanical Analysis for Magnetometry

The magnetometers are built on an optomechanical platform, where AC magnetic field is converted to mechanical motions imprinting on optical field. The amplitude and phase information from optical field can be read out via optical detection scheme. In this thesis, homodyne detection is used. The signal and noise detection from an optomechanical system is based on the derivation of the book by Bowen and Milburn [49] from Chapter 1 to Chapter 3 with an extension to the case where the laser is detuned from the cavity resonance by the factor $\Delta = \omega_0 - \omega_L$ (where ω_0 is the optical resonance frequency and ω_L is the laser frequency).

2.1 System of the optomechanical field magnetometry

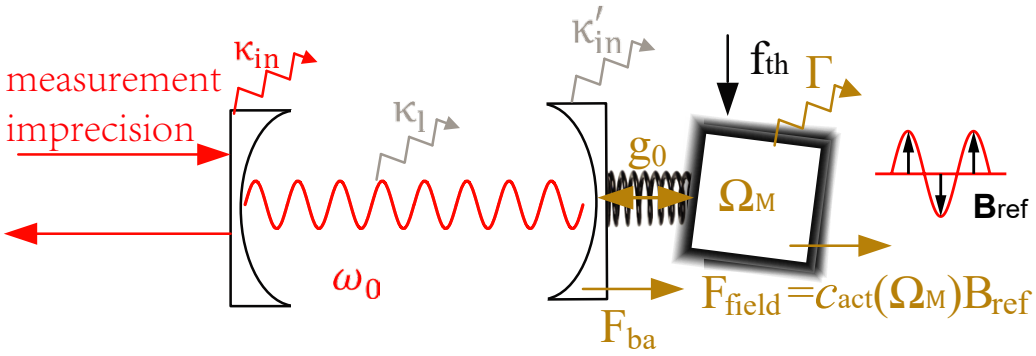

Fig. 2.1 **Cavity optomechanics concept illustrated by a Fabry-Pérot resonator.**

The optomechanical system shown in Fig.2.1 consists of a Fabry-Pérot resonator confining the optical field and a bulk elastic material serving as a mechanical oscillator. The bulk material is magnetostrictive whose shape deforms in response to the external magnetic field, therefore, it converts magnetic field signal (B_{ref}) to a force $F_{field} = c_{act}(\Omega_M)B_{ref}$, where the actuation constant is mechanical mode dependent. A priorly known reference magnetic field B_{ref} is used as signal here for characterization of the sensitivity spectrum. The motion of the magnetostrictive material couples to the optical cavity through dragging one end moveable mirror with vacuum optomechanical coupling rate g_0 (rad·s^{-1}), quantifying the linear dispersive shift of the optical resonance frequency ω_0 at the level of zero-point motion. At finite temperature, an incoherent motion of a mechanical oscillator is excited under finite temperature. The so-called thermal Brownian noise f_{th} will blur the magnetic field driven

motion limiting the sensitivity of the magnetometer. Measurement noise from the light perturbs the end mirror through back-action force F_{ba}, which is rooted from the random kick from the intra-cavity photons due to the optical shot noise. The effect of optical shot noise in the phase quadrature on the readout attributes to measurement imprecision.

The optical cavity is lossy with $\kappa = \kappa_{in} + \kappa_l + \kappa'_{in}$ (rad·s^{-1}) being the total optical decay rate, counting the decay happened at the front mirror, inside optical cavity and at the end mirror. κ_{in} and $\kappa_{loss} = \kappa_l + \kappa'_{in}$ are the input and loss port decay rate. Optical escape efficiency is defined by

$$\eta_0 = \frac{\kappa_{in}}{\kappa_{in} + \kappa_{loss}} \tag{2.1}$$

due to the presence of light absorption in the cavity and scattered by defeats etc. η_0 is an important parameter in the detection process quantifying how much of the output field stands out from noise. The mechanical decay is labelled as Γ (rad·s^{-1}) in Fig. 2.1.

2.2 Interplay between mechanical motion and optical field

Mechanics imprints its information onto optics, and optical measurement influences mechanics. The understanding of the interplay between mechanical motion and optical field is important in knowing the noise source that limits the sensitivity of the magnetometer.

The equation of motion of optical field can be obtained by using quantum Langevin equation under rotation wave approximation for optics with the assumption that $\eta_0 = 1$ [49] and considering the general situation where the detuning from the laser and cavity exists, as

$$\dot{\hat{a}} = -i\Delta\hat{a} - iGNx - \frac{\kappa}{2}\hat{a} + \sqrt{\kappa_{in}}\hat{a}_{in}(t) \tag{2.2}$$

$$\dot{\hat{X}} = -\frac{\kappa}{2}\hat{X} + \Delta\hat{Y} + \sqrt{\kappa}\hat{X}_{in} \tag{2.3}$$

$$\dot{\hat{Y}} = -\frac{\kappa}{2}\hat{Y} - \Delta\hat{X} - \sqrt{2}GNx + \sqrt{\kappa}\hat{Y}_{in} \tag{2.4}$$

where $\hat{X}$ ($\hat{Y}$) refers to the optical amplitude (phase) quadrature, $\hat{a}$ ($\hat{a}_{in}$) describes the loss of the photon number inside (input to) the cavity, N is the time averaged intra-cavity photon number in steady-state, and x is the mechanical position. The mechanical position information is encoded onto optical field via Eq. (2.2) and optical phase quadrature via Eq. (2.4). The optical phase quadrature is related to the optical amplitude quadrature through Eq. (2.3) when the non-zero laser detuning is present.

Using quantum Markovian Langevin equation for mechanics and considering thermal random force due to fluctuation dissipation theorem is the only driving force, resulting the mechanical equation of motion as

$$\dot{\hat{Q}} = \Omega_{\mathrm{M}}\hat{P} \tag{2.5}$$

$$\dot{\hat{P}} = -\Omega_{\mathrm{M}}\hat{Q} - \Gamma\hat{P} + \sqrt{2\Gamma}\hat{P}_{in} - 2g\hat{X} \tag{2.6}$$

where $\hat{P}$ ($\hat{Q}$) is the dimensionless mechanical momentum (position) normalized by zero-point motion $x_{zp} = \sqrt{\hbar/2m\Omega_{\mathrm{M}}}$ (zero-point momentum $p_{zp} = \sqrt{\hbar m\Omega_{\mathrm{M}}/2}$), the dimensionless input momentum has

the expression of

$$\hat{P}_{in}(t) \equiv \frac{x_{zp}\hat{F}(t)}{\hbar\Gamma} \tag{2.7}$$

with $\hat{F}(t)$ being the thermal Brownian force. The optomechanical coupling rate $g = g_0 N$ where the vacuum optomechanical coupling rate g_0 is defined to be linked with the optomechanical coupling strength G as

$$g_0 \equiv G x_{zp}. \tag{2.8}$$

The set of mechanical equations of motion in Eq.(2.5, 2.6) shows that there is no obvious dependence on the laser detuning. However, laser detuning is imprinted on laser amplitude quadrature $\hat{X}$ and can be transferred to mechanical momentum quadrature via Eq. (2.6). With laser detuning, mechanical position imprinted on optical phase quadrature via Eq. (2.4) can be transferred to optical amplitude quadrature via Eq. (2.3) and further influences mechanical momentum via Eq. (2.6) and thus position quadrature via Eq. (2.5). Thus, optic field and mechanical motions are correlated.

Eq. (2.2) can be arranged for input and intra-cavity relation under the consideration of steady-state solution where $\dot{\hat{a}} = 0$ and taking the semi-classical approximation that $\alpha \equiv \langle \hat{a} \rangle$, as

$$\alpha_{ss} = \frac{\sqrt{\kappa_{in}}\alpha_{in}}{\frac{\kappa}{2} + i(\Delta + \sqrt{2}g_0\bar{Q})} \tag{2.9}$$

where $\bar{Q}$ is the time-averaged position $\langle \hat{Q} \rangle$ in steady-state. In practice, the imaginary part $\Delta_{lock} = \Delta + \sqrt{2}g_0\bar{Q}$ can be stabilized to $\Delta_{lock} = 0$ on resonance or other stabilized point, making the detuning to be position dependent. The input-cavity photon number can be related by taking the modulus on both side of Eq. (2.9) as

$$N \equiv |\alpha_{ss}|^2 = \frac{4\eta_0 N_{in}}{\kappa + 4\Delta_{lock}^2/\kappa} \tag{2.10}$$

where Δ_{lock} is labelled as Δ in the following and N_{in} is the input photon number. Eq. (2.10) is important in relating the input laser power to the intra-cavity photon number which interacts with the mechanics.

The interaction of photons and mechanics can be described by the optomechanical cooperativity $|C^{\Delta}(\Omega)|$ and effective cooperativity $|C^{\Delta}_{\text{eff}}(\Omega)|$. They can quantify the precision of the coherent light detection and have the physical meaning of equivalent phonon number created by back-action heating in this thesis, which are defined as

$$C^{\Delta}_{\text{eff}}(\Omega) \equiv \frac{4g_0^2|\alpha_{ss}|^2}{\kappa\Gamma(1-2i\Omega/\kappa)^2} = \frac{16\eta_0\, g_0^2 N_{in}}{\kappa\Gamma(1-2i\Omega/\kappa)^2(\kappa + 4\Delta^2/\kappa)} \tag{2.11}$$

$$C^{\Delta}(\Omega) \equiv C^{\Delta}_{\text{eff}}(\Omega)(1-2i\Omega/\kappa)^2 \tag{2.12}$$

The unique thing here is that $|C^{\Delta}_{\text{eff}}(\Omega)|$ can be determined accurately for a given device with the mechanical property from Eq. (3.61) together with Eq. (2.8). As the numerical solution of Eq. (3.62) is constant across a mechanical resonance as shown in Fig. 3.7d)-e), the effective optomechanical

cooperativity across each mechanical resonance is assumed to be constant as

$$|C_{\text{eff}}^{\Delta}(\Omega_{\text{M}})| = \left(\frac{\delta L}{\max[u(r,\Omega_{\text{M}})]}\right)^2 (\frac{\omega_0}{L})^2 \frac{8\eta_0 \hbar N_{in}}{m\Omega_{\text{M}}\kappa\Gamma|1-2i\Omega_{\text{M}}/\kappa|^2(\kappa+4\Delta^2/\kappa)} \tag{2.13}$$

where $\delta L, L$, $\max[u(r,\Omega_{\text{M}})]$, Ω_{M} and m is taken as the effective motional mass as m_{eff} can be extracted from COMSOL accurately, while κ and Γ can be taken empirically from experimental observations. η_0 and ω_0 are treated as constant. With the input of photon number N_{in} in the unit of laser power (W) and detuning Δ. The accuracy of the $|C_{\text{eff}}^{\Delta}(\Omega_{\text{M}})|$ is only limited by the empirical optical and mechanical damping, which depends on fabrication process and geometry.

Laser detuning would change the mechanical damping and the mechanical resonance frequencies due to a delay for the photon to meet the new boundary condition created by the mechanical oscillation, which is called dynamical back-action [49, 50]. It is interesting to know how the laser detuning affects the bandwidth and sensitivity of our optomechanical magnetometers.

From Eq. (2.3, 2.4) the steady-state solution can be reached after applying Fourier transformation

$$\tilde{X}(\Omega) = \frac{-2g\Delta\tilde{Q} + \sqrt{\kappa}\tilde{X}_{in}\left(\frac{\kappa}{2}-i\Omega\right) + \Delta\sqrt{\kappa}\tilde{Y}_{in}}{\left(\frac{\kappa}{2}-i\Omega\right)^2+\Delta^2} \tag{2.14}$$

$$\tilde{Y}(\Omega) = \frac{-2g(\kappa/2-i\Omega)\tilde{Q} - \Delta\sqrt{\kappa}\tilde{X}_{in} + (\kappa/2-i\Omega)\sqrt{\kappa}\tilde{Y}_{in}}{(\kappa/2-i\Omega)^2+\Delta^2} \tag{2.15}$$

From the input-output relation [49] and Eq. (2.14) followed by a Fourier transform to the frequency domain leads to

$$\begin{aligned}\tilde{X}_{out}(\Omega) &= \tilde{X}_{in}(\Omega) - \sqrt{\kappa}\tilde{X}(\Omega) \\ &= \frac{(\kappa/2-i\Omega)^2+\Delta^2-\kappa(\kappa/2-i\Omega)}{(\kappa/2-i\Omega)^2+\Delta^2}\tilde{X}_{in}(\Omega) - \frac{\Delta\kappa}{(\kappa/2-i\Omega)^2+\Delta^2}\tilde{Y}_{in}(\Omega) \\ &+ \frac{2\sqrt{\kappa}\,\Delta\, g}{(\kappa/2-i\Omega)^2+\Delta^2}\tilde{Q}(\Omega).\end{aligned} \tag{2.16}$$

The equation of motion of the mechanical oscillator from Eq.(2.5, 2.6) is

$$\ddot{\hat{Q}} + \Gamma\dot{\hat{Q}} + \left[\Omega_{\text{M}}^2 - \frac{4g^2\Omega_{\text{M}}\Delta}{(\kappa/2-i\Omega)^2+\Delta^2}\right]\hat{Q} = \sqrt{2\Gamma}\Omega_{\text{M}}\hat{P}_{in} - 2g\Omega\frac{\sqrt{\kappa}\hat{X}_{in}(\kappa/2-i\Omega)+\Delta\sqrt{\kappa}\hat{Y}_{in}}{(\kappa/2-i\Omega)^2+\Delta^2} \tag{2.17}$$

From the mechanical position equation of motion, the modified mechanical susceptibility with $\chi_{\Delta}(\Omega)$ and without $\chi(\Omega)$ laser detuning can be obtained as:

$$\chi(\Omega) = \frac{\Omega_{\text{M}}}{-\Omega^2 - i\Omega\Gamma + \Omega_{\text{M}}^2} \tag{2.18}$$

$$\chi_{\Delta}(\Omega) = \frac{\Omega_{\text{M}}}{-\Omega^2 - i\Omega\Gamma + \Omega_{\text{M}}^2 - \frac{4g^2\Omega_{\text{M}}\Delta}{(\kappa/2-i\Omega)^2+\Delta^2}} \equiv \frac{\Omega_{\text{M}}}{-\Omega^2 - i\Omega(\Gamma+\Gamma_{opt}) + (\Omega_{\text{M}}+\delta\Omega_{\text{M}})^2}, \tag{2.19}$$

and the mechanical position operator can be obtained as:

$$\tilde{Q}(\Omega) = \chi_\Delta(\Omega)\left[\sqrt{2\Gamma}\tilde{P}_{in} - 2\sqrt{C_{\text{eff}}^{\Delta}(\Omega)\,\Gamma}\,\frac{(\kappa/2 - i\Omega)^2\tilde{X}_{in} + \Delta\,(\kappa/2 - i\Omega)\tilde{Y}_{in}}{(\kappa/2 - i\Omega)^2 + \Delta^2}\right] \tag{2.20}$$

where $g = (\kappa/2 - i\Omega)\sqrt{C_{\text{eff}}^{\Delta}(\Omega)\,\Gamma/\kappa}$ is used for replacement. This equation shows that mechanical position is related with input mechanical momentum, amplitude and phase information of the input light. If the detuning factor $\Delta = 0$, then the mechanical position would be unaffected by the light phase fluctuation, and thus in a spectrum analysis the mechanical position spectral density would only be influenced by the correlations between input light amplitude and input mechanical momentum rather than correlations among $\tilde{P}_{in}$, $\tilde{X}_{in}$ and $\tilde{Y}_{in}$. In the optomechanical magnetometers' system considered here, the fluctuations from the incoherent thermally driven input mechanical momentum are assumed to have no correlations with either light amplitude or phase fluctuations. Also the correlations between the light amplitude and phase quadrature is neglected for coherent light source.

From Eq. (2.19) the dynamical back-action modified mechanical damping and eigenfrequency become

$$\frac{\Gamma_\Delta(\Omega_{\text{M}})}{\Gamma(\Omega_{\text{M}})} \equiv \frac{\Gamma + \Gamma_{opt}}{\Gamma} = 1 + C^{\Delta}(\Omega_{\text{M}})\frac{\Omega_{\text{M}}\,\Delta\,\kappa^2}{(\kappa^2/4 + \Delta^2 - \Omega_{\text{M}}^2)^2 + (\kappa\Omega_{\text{M}})^2} \tag{2.21}$$

$$\left(\frac{\Omega_{\text{M}}^{\Delta}(\Omega_{\text{M}})}{\Omega_{\text{M}}(\Omega_{\text{M}})}\right)^2 \equiv \frac{\Omega_{\text{M}} + \delta\Omega_{\text{M}}}{\Omega_{\text{M}}} = 1 - C^{\Delta}(\Omega_{\text{M}})\frac{\kappa\Delta\,(\kappa^2/4 + \Delta^2 - \Omega_{\text{M}}^2)}{Q_{\text{M}}\left[(\kappa^2/4 + \Delta^2 - \Omega_{\text{M}}^2)^2 + (\kappa\Omega_{\text{M}})^2\right]} \tag{2.22}$$

where $Q_{\text{M}} = \Omega_{\text{M}}/\Gamma$. With blue detuning $\Delta < 0$, the mechanical resonance spectrum peak reduces, and eventually when $\Gamma_\Delta(\Omega_{\text{M}}) < 0$ instability will occur leading to chaos [50]. Also the input laser power should be limited to ensure that Eq. (2.22) stays positive.

2.3 Direct and homodyne detection techniques

There are several ways to detect the output light in Eq. (2.16), such as direct and homodyne detection techniques for their signal-to-noise ratio (SNR) performance.

To be detected, light field has to be coupled to the system. Near field coupling scheme is used in cavity optomechanical magnetometry where a tapered fibre is brought to close proximity in the same order as the wavelength of the light to the device. The device could be a toroid surround with magnetostrictive material Terfenol-D, whose artistic depiction is displayed in Fig. 2.2b). The near field evanescent light field goes into the device via a coupling rate κ_{in} when the reflective index of the fibre is larger than that of the device to avoid the total internal reflection from the fibre to the device.

Direct detection technique records intensity of the optical field on the detector, as a common way of detecting optical signals: directing a signal from an optical fibre to a photon detector for instance. The detected photon current can be written as

$$i(t) = \eta_1 \cdot N_{\text{out}}(t) = \eta_1 \cdot a_{\text{out}}^*(t)a_{\text{out}}(t) \tag{2.23}$$

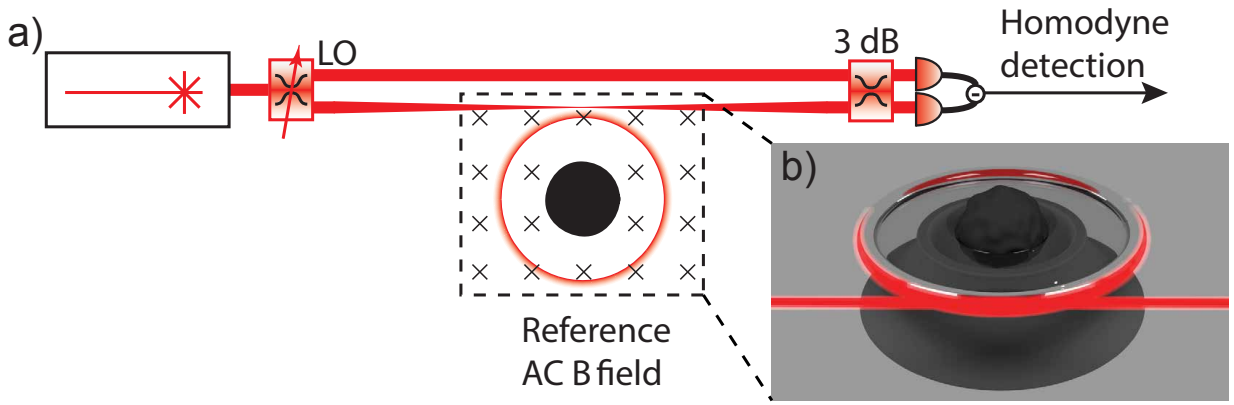

Fig. 2.2 **Simplest Homodyne detection scheme. a)** The device under test is immersed in magnetic field shown as $\times$ symbol perpendicular to the plane. **b)** An artistic view of a magnetometer being coupled to an optical fibre via an evanescent optical field.

where η_1 is the detection efficiency counting the loss when transferring the photon to the electric current at the photon diode, a_{out} is the output field amplitude and N is the output photon flux. If considering only the modulations on the optical field, $a_{\text{out}}(t)$ can be described as: $a_{\text{out}}(t) \to \alpha + \delta a(t)$ where $\langle \delta a(t) \rangle = 0$ and $\langle |\delta a(t)|^2 \rangle = 0$ describes that the modulation has zero mean but not zero over time, and α is a positive complex number. When considering the modulation, Eq. (2.23) then becomes

$$i(t) = \eta_1 [|\alpha|^2 + \alpha \delta a^*(t) + \alpha^* \delta a(t) + |\delta a(t)|^2] \tag{2.24}$$

$$= \eta_1 \frac{|\alpha|}{\sqrt{2}} \left[\frac{\alpha}{|\alpha|} \delta a^*(t) + \frac{\alpha^*}{|\alpha^*|} \delta a(t) \right] = \eta_1 \frac{|\alpha|}{\sqrt{2}} \left[\delta a^*(t) e^{i\theta_{\text{out}}} + \delta a(t) e^{-i\theta_{\text{out}}} \right] \equiv \eta_1 |\alpha| \mathscr{X}^{\theta_{\text{out}}}(t) \tag{2.25}$$

where $\mathscr{X}^0$ ($\mathscr{X}^{\frac{\pi}{2}}$) is the light amplitude (phase) quadrature. Noise product term in Eq. (2.24) is negelected in Eq. (2.25). This approximation is valid when the optical coherent driving field is large compared to the modulation. The constant term $|\alpha|^2$ in Eq. (2.24) is also neglected as its Fourier transformation [51] writes:

$$\tilde{i}(\omega) \propto |\alpha|^2 \delta(0) + \alpha \delta \tilde{a}^*(\Omega_{\text{M}}) + \alpha^* \delta \tilde{a}(\Omega_{\text{M}}) \tag{2.26}$$

where the first term is the coherent average power centred at 0 modulated frequency is a DC signal which can be filtered. Ω_{M} is the modulation frequency, in our cavity optomechanical magnetometry it's the mechanical eigenfrequency and actuation frequency from the external AC magnetic field signal. Under a spectrum analysis, the coherent power part can be distinguished from the rest. Though direct detection is easy to be implemented, its measuring quadrature is limited to the direction of the coherent field.

Balanced homodyne detection is an elegant technique to measure arbitrary quadrature of light for optomechanical system. Shown in Fig. 2.2a), the simplest sketch consists of a 3 dB coupler mixing signal beam with strong reference beam (local oscillator) at the same frequency (Eq.(2.27)), as can be indicated from 'homo' meaning the same. The signal beam consists of a tapered fibre evanescently

coupling coherent light field to the device under test. The detected photon current takes the difference from the two detectors as expressed as $\pm$ in Eq. (2.28). The strong local oscillator, as can be seen in Eq. (2.30), boosts the small signal field. The modulated signal $\delta a(t)$ is mixed with a strong local oscillator field $a_{LO} = \alpha_{LO} + \delta\alpha_{LO}$ at the two detectors as:

$$a_{\pm}(t) = \frac{1}{\sqrt{2}}\Big[a_{LO}(t) \pm \delta a(t)\Big] \tag{2.27}$$

$$i(t) = i_{+}(t) - i_{-}(t) = \eta_1\Big(a_{+}^{*}(t)a_{+}(t) - a_{-}^{*}(t)a_{-}(t)\Big) \tag{2.28}$$

$$= \eta_1\Big[\alpha_{LO}^{*}\delta a(t) + \alpha_{LO}\delta a^{*}(t)\Big] \tag{2.29}$$

$$= \eta_1\frac{|\alpha_{LO}|}{\sqrt{2}}\Big[\frac{\alpha_{LO}^{*}}{|\alpha_{LO}^{*}|}\delta a(t) + \frac{\alpha_{LO}}{|\alpha_{LO}|}\delta a^{*}(t)\Big] \equiv \eta_1|\alpha_{LO}|\mathscr{X}^{\theta}(t) \tag{2.30}$$

where the noise fluctuation from the local oscillator is ignored.

In contrast to direct detection, homodyne detection has the advantage of having access into all the angles in amplitude-phase quadrature of the optical field by varying the phase of the local oscillator. Therefore, direct detection is a special case for homodyne detection, and the following power spectral density calculations will be based on the homodynes' phase and amplitude quadrature operators.

2.4 Power spectral density with and without laser detuning

The photon current $i(t)$ converted from the output photon is directed to electronic device for analysis. To get power spectral density, a spectrum analyser is used which converts the time dependent signal to a spectrum. According to Wiener-Khinchin theorem under stationary statistics the power spectral density of a general time dependent signal $\mathscr{O}(t)$ is

$$S_{\mathscr{O}\mathscr{O}}(\Omega) = \int_{-\infty}^{\infty} d\tau e^{i\Omega\tau}\big\langle\mathscr{O}^{*}(t+\tau)\mathscr{O}(t)\big\rangle_{t=0} = \int_{-\infty}^{\infty} d\Omega'\big\langle\tilde{\mathscr{O}}^{*}(-\Omega)\tilde{\mathscr{O}}(\Omega')\big\rangle \tag{2.31}$$

A current signal directed to a spectrum and network analyser can be expressed in the form of

$$i(t) = I(t) + \varepsilon(t) \tag{2.32}$$

where I is the DC part of the current having a mean of $\langle I(t)\rangle = \alpha_i$, and α_i is a complex constant. $\langle\varepsilon(t)\rangle = 0$ for both incoherent noise and modulated coherent signal. The power spectrum density measured by the spectrum analyser [52] from Eq. (2.26, 2.31, 2.32) then is

$$\mathrm{SA}(\Omega) = \Big\langle\tilde{i}^{*}(\Omega)\tilde{i}(\Omega')\Big\rangle = \Big\langle\Big(\tilde{I}^{*}(\Omega) + \tilde{\varepsilon}^{*}(\Omega)\Big)\Big(\tilde{I}(\Omega') + \tilde{\varepsilon}(\Omega')\Big)\Big\rangle \tag{2.33}$$

$$= \begin{cases} |\alpha_i|^2\delta^2(0) + \alpha_i^{*}\tilde{\eta}_2(\Omega)\big\langle\tilde{\varepsilon}(\Omega)\big\rangle + \alpha_i\tilde{\eta}_2(\Omega)\big\langle\tilde{\varepsilon}(\Omega)\big\rangle + \Big\langle\big|\tilde{\varepsilon}(\Omega)\big|^2\Big\rangle, & \text{incoherent } \varepsilon \\ |\alpha_i|^2\delta^2(0) + \alpha_i^{*}\delta(\Omega_{\mathrm{M}})\big\langle\tilde{\varepsilon}(\Omega)\big\rangle + \alpha_i\delta(\Omega_{\mathrm{M}})\big\langle\tilde{\varepsilon}(\Omega)\big\rangle + \Big\langle\big|\tilde{\varepsilon}(\Omega)\big|^2\Big\rangle, & \text{modulated } \varepsilon \end{cases} \tag{2.34}$$

The first term in Eq. (2.34) is a peak centred at 0 frequency of the spectrum due to the auto-correlation without modulation. The second and third terms are 0 as $\langle\tilde{\varepsilon}(\Omega)\rangle = 0$ and $\langle\tilde{\varepsilon}^*(\Omega)\rangle = 0$. $\tilde{\eta}_2(\Omega)$ counts for white noise spectrum if ε is incoherent noise. For a single modulation frequency Ω_{M}, terms with $\delta(\Omega_{\mathrm{M}}$ are 0. Only the last term is what the spectrum analyser outputs, though $\langle\varepsilon(t)\rangle = 0$, $\langle\varepsilon^*(t)\varepsilon(t)\rangle > 0$. This shows that spectrum analyser measures input with 0 mean no matter whether the input is coherently driven or white noise. In the cavity optomechanical magnetometers system. Spectrum analyser is used to measure noise source of thermal Brownian motion and laser noise, as well as coherently driven reference magnetic field. The analysis of spectrum density considering thermal and laser noise is as follows, while characterization of reference magnetic field is experimental techniques can be referred to ref.[26].

The power spectral density of the output X and Y quadrature of light is obtained by combining Eq. (2.20, 2.16, 2.31) and neglecting the both the correlation between thermal Brownian noise and optical shot noise and inside the optical amplitude and phase quadrature, as

$$\begin{aligned}\bar{S}_{\tilde{X}_{out}\tilde{X}_{out}}(\Omega) &= B1\cdot\bar{S}_{\tilde{X}_{in}\tilde{X}_{in}} + B2\cdot\bar{S}_{\tilde{Y}_{in}\tilde{Y}_{in}} \\ &+ \sum_{\Omega_{\mathrm{M}}} 8\eta\Gamma^2(\Omega_{\mathrm{M}})|C^{\Delta}_{\mathrm{eff}}(\Omega_{\mathrm{M}})|A2|\chi_{\Delta}(\Omega)|^2\Big[\frac{k_BT}{\hbar\Omega_{\mathrm{M}}} + 2|C^{\Delta}_{\mathrm{eff}}(\Omega_{\mathrm{M}})|\Big(A1\cdot\bar{S}_{\tilde{X}_{in}\tilde{X}_{in}} + A2\cdot\bar{S}_{\tilde{Y}_{in}\tilde{Y}_{in}}\Big)\Big]\end{aligned} \tag{2.35}$$

$$\begin{aligned}\bar{S}_{\tilde{Y}_{out}\tilde{Y}_{out}}(\Omega) &= B2\cdot\bar{S}_{\tilde{X}_{in}\tilde{X}_{in}} + B1\cdot\bar{S}_{\tilde{Y}_{in}\tilde{Y}_{in}} \\ &+ \sum_{\Omega_{\mathrm{M}}} 8\eta\Gamma^2(\Omega_{\mathrm{M}})|C^{\Delta}_{\mathrm{eff}}(\Omega_{\mathrm{M}})|A1|\chi_{\Delta}(\Omega)|^2\Big[\frac{k_BT}{\hbar\Omega_{\mathrm{M}}} + 2|C^{\Delta}_{\mathrm{eff}}(\Omega_{\mathrm{M}})|\Big(A1\cdot\bar{S}_{\tilde{X}_{in}\tilde{X}_{in}} + A2\cdot\bar{S}_{\tilde{Y}_{in}\tilde{Y}_{in}}\Big)\Big]\end{aligned} \tag{2.36}$$

$$A1 = \Big|\frac{(\kappa/2 - i\Omega)^2}{(\kappa/2 - i\Omega)^2 + \Delta^2}\Big|^2 \tag{2.37}$$

$$A2 = \Big|\frac{\Delta\,(\kappa/2 - i\Omega)}{(\kappa/2 - i\Omega)^2 + \Delta^2}\Big|^2 \tag{2.38}$$

$$B1 = \Big|1 + \frac{-\kappa^2/2 + i\Omega\kappa}{(\kappa/2 - i\Omega)^2 + \Delta^2}\Big|^2 \tag{2.39}$$

$$B2 = \Big|\frac{\Delta\kappa}{(\kappa/2 - i\Omega)^2 + \Delta^2}\Big|^2 \tag{2.40}$$

where $\eta = \eta_0\cdot\eta_1$ is the efficiency counting the light escaping from the cavity as well as the conversion of photons to electric current in detection process. The first term in the square bracket of Eq. (2.35) is the number of phonons created under thermal bath at mechanical resonance frequency, and the second term with a coefficient of $|c^{\Delta}_{\mathrm{eff}}(\Omega_{\mathrm{M}})|$ has the physical meaning of equivalent phonon created by back-action heating. To get Eq. (2.35), the power spectral density of $\hat{P}_{in}(t)$ is used as a result of a bath force from fluctuation dissipation theorem the same as in Eq. (2.7). Here the thermal noise dominates bath fluctuation than photon noise, therefore n is the phonon number

$$S_{P_{in}P_{in}}(\Omega) = \frac{\Omega}{\Omega_{\mathrm{M}}}\big(\bar{n}+1\big) \tag{2.41}$$

$$S_{P_{in}P_{in}}(-\Omega) = \frac{\Omega}{\Omega_{\mathrm{M}}}\bar{n} \tag{2.42}$$

$S_{P_{in}P_{in}}(\Omega)$ and $S_{P_{in}P_{in}}(-\Omega)$ have different expressions as a result of difference in upwards and downwards going transition rates [49]. For symmetrised bath power spectral density and at high temperature limit

$$\bar{S}_{P_{in}P_{in}}(\Omega) = \frac{1}{2}\left[S_{P_{in}P_{in}}(\Omega) + S_{P_{in}P_{in}}(-\Omega)\right] \tag{2.43}$$

$$= \frac{\Omega}{\Omega_{\mathrm{M}}}\left(\bar{n} + \frac{1}{2}\right) \tag{2.44}$$

$$\approx \frac{\Omega}{\Omega_{\mathrm{M}}}\frac{k_B T}{\hbar\Omega} = \frac{k_B T}{\hbar\Omega_{\mathrm{M}}}. \tag{2.45}$$

When we consider the laser detuning, the mechanical position information encodes both to the light amplitude and phase quadrature. Therefore, the homodyne detection angle can be relaxed.

For simple case of on-resonance optical driving when detuning $\Delta = 0$, there is no dynamical back-action for the optomechancial system and the mechanical motion only imprints on the phase quadrature of the light by its momentum. The power spectrum density for homodyne detection of the light phase quadrature is given in [49] or set $\Delta = 0$ in Eq. (2.35, 2.36, 2.37, 2.38) as follows:

$$\tilde{Y}_{out}(\Omega) = -\left(\frac{\kappa/2 + i\Omega}{\kappa/2 - i\Omega}\right)\tilde{Y}_{in}(\Omega) + 2\Gamma(\Omega)\sqrt{2C_{\mathrm{eff}}(\Omega_{\mathrm{M}})}\chi(\Omega)[\tilde{P}_{in}(\Omega) - \sqrt{2C_{\mathrm{eff}}(\Omega_{\mathrm{M}})}\tilde{X}_{in}(\Omega)] \tag{2.46}$$

$$\begin{aligned} S_{ii}^{homo}(\Omega) &= \bar{S}_{\tilde{Y}_{out}\tilde{Y}_{out}}(\Omega) \\ &= \bar{S}_{\tilde{Y}_{in}\tilde{Y}_{in}}(\Omega) + \sum_{\Omega_{\mathrm{M}}} 8\eta\Gamma^2(\Omega_{\mathrm{M}})|C_{\mathrm{eff}}(\Omega_{\mathrm{M}})| \cdot |\chi(\Omega)|^2 \left[\bar{S}_{\tilde{P}_{in}\tilde{P}_{in}}(\Omega) + 2|C_{\mathrm{eff}}(\Omega_{\mathrm{M}})|\bar{S}_{\tilde{X}_{in}\tilde{X}_{in}}(\Omega)\right] \end{aligned} \tag{2.47}$$

$$= \frac{1}{2} + \sum_{\Omega_{\mathrm{M}}} 8\eta\Gamma^2(\Omega_{\mathrm{M}})|C_{\mathrm{eff}}(\Omega_{\mathrm{M}})| \cdot |\chi(\Omega)|^2 \left[\frac{\Omega}{\Omega_{\mathrm{M}}}\left(\bar{n}_m(\Omega) + \frac{1}{2}\right) + |C_{\mathrm{eff}}(\Omega_{\mathrm{M}})|\right] \tag{2.48}$$

$$= \frac{1}{2} + \sum_{\Omega_{\mathrm{M}}} 8\eta\Gamma^2(\Omega_{\mathrm{M}})|C_{\mathrm{eff}}(\Omega_{\mathrm{M}})| \cdot |\chi(\Omega)|^2 \left(\frac{k_B T}{\hbar\Omega_{\mathrm{M}}} + n_{ba}\right) \tag{2.49}$$

where $|C_{\mathrm{eff}}(\Omega_{\mathrm{M}})|$ is obtained from Eq. (2.11) by setting the detuning $\Delta = 0$. From Eq. (2.48) to Eq. (2.49), the high temperature limit is used where thermal noise excites the number of phonon $\bar{n}(\Omega) + 1/2 \approx k_B T/\hbar\Omega \sim 10^5 - 10^6$ for our devices by the 1st order RBM around 30 MHz is much larger than the photon fluctuation $\bar{S}_{\tilde{Y}_{in}\tilde{Y}_{in}}(\Omega) = \bar{S}_{\tilde{X}_{in}\tilde{X}_{in}}(\Omega) = 1/2$ for coherent light source.

To estimate how the back-action influences our system, the input measurement strength is chosen to be at the standard quantum limit for mechanical position measurement.

The output mechanical position can be obtained through the combination of Eq. (2.46) and the definition of the part of mechanical position without the influence of the measurement, as

$$\tilde{Q}^0(\Omega) \equiv \sqrt{2\Gamma}\chi(\Omega)\tilde{P}_{in}(\Omega), \tag{2.50}$$

where the source of $\tilde{P}_{in}$ is from thermal bath, as

$$\tilde{Q}_{out}(\Omega) = \tilde{Q}^0(\Omega) - \underbrace{\frac{1}{2\sqrt{\Gamma C_{\rm eff}(\Omega_{\rm M})}}\left(\frac{\kappa/2+i\Omega}{\kappa/2-i\Omega}\right)\tilde{Y}_{in}(\Omega)}_{\text{measurement noise}} - \underbrace{2\sqrt{\Gamma C_{\rm eff}(\Omega_{\rm M})}\chi(\Omega)\tilde{X}_{in}(\Omega)}_{\text{back-action noise}}. \tag{2.51}$$

The second term on the right hand side of Eq. (2.51) is linear with the phase quadrature of the light counting for the imprecision noise due to the presence of laser phase noise, meaning the stronger the input laser power cranked up to ($C_{\rm eff} \to \infty$), the more accurate the measurement will be (this term$\to 0$), and η is introduced counting for measurement efficiency. However, the last term boosted by the laser amplitude quadrature takes charge of the radiation back-action heating noise. Therefore, there is an optimised input power for minimum combinations of impression noise and back-action heating noise without taking thermal noise into consideration, which is called standard quantum limit. Normalising the power spectral density of light into mechanical position unit gives

$$\bar{S}_{\tilde{Q}_{out}\tilde{Q}_{out}}(\Omega) = \underbrace{\frac{1}{8\eta\Gamma|C_{\rm eff}(\Omega_{\rm M})|}}_{\text{measurement noise}} + \underbrace{2\Gamma|\chi(\Omega)|^2|C_{\rm eff}(\Omega_{\rm M})|}_{\text{back-action noise}} \tag{2.52}$$

The minimum total optical noise from Eq. (2.52) is reached from mechanical position measurement when the cooperativity is

$$|C_{\rm eff}(\Omega_{\rm M})| = \frac{1}{4\eta^{1/2}\Gamma|\chi(\Omega_{\rm M})|} = \frac{1}{4\eta^{1/2}} \tag{2.53}$$

Assuming detection efficiency $\eta = 1$ gives $|C_{\rm eff}(\Omega_{\rm M})| = 0.25$. This means back-action heating created phonon number is 0.25, which is far less than thermally excited phonon number $k_BT/\hbar\Omega_{\rm M} \sim 10^5 - 10^6$ from Eq. (2.49) in our room temperature operated 100-micrometre sized devices. Therefore, noise from back-action heating could be safely neglected.

2.5 Network response for exciting external magnetic field

Network analyser on the other hand has an inbuilt local oscillator mixing the incoming signal, and the outcome is the Fourier transform of the mean mixture. The current signal of Eq. (2.32) can be expanded to have an additional coherently modulated term $|I_1|e^{-i\Omega_{\rm M}}$ at a frequency $\Omega_{\rm M}$ where $|I_1| > 0$ and $\varepsilon(t)$ is kept as incoherent noise as

$$i(t) = I + |I_1|e^{-i\Omega_{\rm M}} + \varepsilon(t). \tag{2.54}$$

The function of local oscillator is to mix the input $i(t)$ with $e^{i\Omega t}$, therefore, a simplified network response can be obtained as

$$\begin{aligned} {\rm NA}(\omega) &= \mathscr{F}\mathscr{T}\left(e^{i\Omega t}\cdot i(t)\right)\mathscr{F}\mathscr{T}^*\left(e^{i\Omega t}\cdot i(t)\right) &(2.55)\\ &= \mathscr{F}\mathscr{T}\left(\alpha_i e^{-i\Omega t} + |I_1|e^{-i(\Omega_{\rm M}-\Omega)t} + \varepsilon e^{-i\Omega t}\right)\mathscr{F}\mathscr{T}\left(c.c.\right) &(2.56)\end{aligned}$$

$$= |\alpha_i|^2\delta^2(\Omega) + |I_1|\delta^2(\Omega-\Omega_{\rm M}) + |\varepsilon|^2\delta^2(\Omega) \tag{2.57}$$

$$= \begin{cases} |I_1|^2 & \text{if } \Omega = \Omega_{\rm M}, \\ |\alpha_i|^2 + |\varepsilon|^2 & \text{if } \Omega = 0, \\ 0 & \text{otherwise.} \end{cases} \tag{2.58}$$

Therefore, network analyser measures parameters which could be coherently driven and output the phase and amplitude information of the driving. Though thermal Brownian noise has modulation frequencies, its phase is random as it can not be fit into $|I_1|e^{-i\Omega_{\rm M}}$ type. In cavity optomechanical magnetometry, the displacement of the magnetometer driven by AC external magnetic field is measured by network analyser.

To get the network response of the displacement driven by magnetic field, the thermal force spectrum expressed in terms of k_bT in Eq. (2.35, 2.36) derived from input mechanical momentum spectrum with Eq. (2.41, 2.42) needs to be replaced with the mechanical momentum in Eq. (2.7) purely driven by the coherent force $F_{\rm field} = c_{act}{\rm B}_{\rm ref}$ where $B_{\rm ref}$ is the reference magnetic field used to excite the displacement. Here the coherent force means that there exists correlations between magnetic-force-driven mechanical displacement at different mechanical eigenfrequencies. And thus the calculation should first take the sum of harmonic oscillator at all frequencies of interest, and then take the modulus square. In contrast to the uncorrelated thermal force in Eq. (2.35, 2.36) where the modulus square is taken at individual eigenmodes. Interference between the mechanical displacment driven by coherent force at different mechanical eigenmodes is indeed observed in the experiment driven by electric force [53]. The network response of mechanical displacement driven by magnetic field force $F_{\rm field} = c_{act}B_{\rm ref}$ in light amplitude and phase quadrature is

$$\bar{S}^{BB}_{\tilde{X}_{out}\tilde{X}_{out}}(\Omega) = 8\cdot\eta\cdot A2\left|\sum_{\Omega_{\rm M}}\Gamma(\Omega_{\rm M})\sqrt{|{\rm C}^{\Delta}_{\rm eff}(\Omega_{\rm M})|}\;\chi_{\Delta}(\Omega)\frac{c_{act}(\Omega_{\rm M})B_{\rm ref}}{\sqrt{4m_{\rm eff}\Omega_{\rm M}\hbar\Gamma(\Omega_{\rm M})}}\right|^2 \tag{2.59}$$

$$\bar{S}^{BB}_{\tilde{Y}_{out}\tilde{Y}_{out}}(\Omega) = 8\cdot\eta\cdot A1\left|\sum_{\Omega_{\rm M}}\Gamma(\Omega_{\rm M})\sqrt{|{\rm C}^{\Delta}_{\rm eff}(\Omega_{\rm M})|}\;\chi_{\Delta}(\Omega)\frac{c_{act}(\Omega_{\rm M})B_{\rm ref}}{\sqrt{4m_{\rm eff}\Omega_{\rm M}\hbar\Gamma(\Omega_{\rm M})}}\right|^2 \tag{2.60}$$

where the expression for $A1$ and $A2$ can be found in Eq. (2.37, 2.38), and the 4 on the denominator is because the mechanical decay rate is taken as a full-width-half-maximum of the mechanical resonance. Therefore, the classical thermal random force spectrum is $\bar{S}^{class}_{FF} = 4m\Gamma k_BT$.

The quotient of the network response measuring the magnetic field and noise power spectral density gives a combination of SNR and resolution bandwidth (RBW). By checking the unit of the noise power spectral density in Eq. (2.49), we found it has the unit of 1. While the network response driven by $F_{\rm field}$ in Eq. (2.59, 2.60) has the unit of $F^2_{\rm field}/4m_{\rm eff}\Omega_{\rm M}\hbar$ $({\rm Hz}/2\pi)$ when taking parameters κ,Γ with unit of $({\rm rad}\cdot{\rm s}^{-1})$. RBW has the unit of Hz. The minimum detectable magnetic field is defined as

$$B_{\rm min}(\Omega) \equiv \frac{B_{\rm ref}}{\sqrt{{\rm SNR}\cdot{\rm RBW}}} = \frac{B_{\rm ref}}{\sqrt{\bar{S}^{BB}_{\tilde{X}/\tilde{Y}_{out}\tilde{X}/\tilde{Y}_{out}}(\Omega)\Big/\bar{S}_{\tilde{X}/\tilde{Y}_{out}\tilde{X}/\tilde{Y}_{out}}(\Omega)}}\;\underbrace{\left(\frac{\rm T}{\sqrt{\rm Hz/2\pi}}\right)}_{\rm unit} \tag{2.61}$$

which can be obtained from the quotient of Eq. (2.59)/(2.60) and Eq. (2.35)/(2.36). The sensitivity calculated above has to be divided by a factor of $\sqrt{2\pi}$ to reach the commonly used unit of sensing community (T/$\sqrt{\text{Hz}}$).

For single mechanical mode, the minimum detectable magnetic field is square root of the force noise spectrum divided by actuation constant c_{act}. The power spectral density of the noise force driving the mechanics can be related with the normalized power spectrum density of light in the unit of mechanical position [49] as

$$\bar{S}_{FF}(\Omega) = \frac{\hbar m_{\text{eff}} \Omega_{\text{M}}}{|\chi(\Omega)|^2} \bar{S}_{QQ}(\Omega). \tag{2.62}$$

where the $\bar{S}_{QQ}(\Omega)$ includes the thermal noise from Eq. (2.45, 2.50) and measurement noise and back-action noise from Eq. (2.52). There, the magnetic field sensitivity limited by the combination of thermal, measurement and back-action noise can be written as

$$B_{min}(\Omega_{\text{M}}) = \frac{1}{\sqrt{2\pi} c_{act}(\Omega_{\text{M}})} \sqrt{\underbrace{4 m_{\text{eff}} \Gamma k_B T}_{\text{thermal noise}} + \underbrace{\frac{m_{\text{eff}} \hbar Q_{\text{M}}}{8\eta |\chi_\Delta|^2 \left| C_{\text{eff}}^\Delta \right|}}_{\text{measurement noise}} + \underbrace{4 m_{\text{eff}} \Gamma \hbar \Omega_{\text{M}} |C_{\text{eff}}^\Delta|}_{\text{back-action}}} \tag{2.63}$$

where Q_{M} is the mechanical quality factor, and $m_{\text{eff}}, \Gamma, |\chi_\Delta|, Q_{\text{M}}$ and C_{eff}^Δ in the square root are also mechanical eigenmode Ω_{M} dependent in addition to the actuation constant $c_{act}(\Omega_{\text{M}})$. Note that if the thermal noise dominates the sum of the thermal and laser shot noise, then it may be called thermal noise limited. In our system, impression noise depends on the optomechanical coupling strength for individual mechanical modes as well as the laser power.

Chapter 3

Mechanical Properties of Optomechanical Magnetometry from Numerical Simulation

Bulk materials exhibit mechanical oscillations at their mechanical resonance frequencies when they absorb energy from external fields and thermal environment. The behaviour of each mechanical eigenmode can be well simplified as a damped harmonic oscillator. The smaller the damping parameter Γ (rad·s^{-1}) is, the longer the mechanical oscillation will sustain for a single pulsed input or the larger the amplitude will be for a continuous driving. In this specific application of cavity optomechanical magnetometry, the energy input comes from the magnetic field of the specimens while the noise contributions come from the thermal bath at room temperature and the light bath introduced in the process of detecting mechanical oscillation. Numerical solutions of elastic wave equation with a driving term reveal the noise free sensors' performance and give the three dimensional (3D) shape deformation of the magnetometers, which is hard to solve analytically. Combined with the scalar theory of optomechanics (discussed in Chapter 2), the shape deformation information helps to better predict the performances of the magnetometers.

3.1 Time domain structural dynamics

Small mechanical oscillation of an elastic medium can be described by the elastic wave equation. We start with the simple case where there is no driving term and an isotropic material is considered, and later the external driving term will be included as a part of stress (see in Chapter 3.2). The elastic wave equation [36] in the time domain is given by

$$\rho \frac{\partial^2 u_i}{\partial t^2} = \frac{\partial \sigma_{ij}}{\partial x_j} \tag{3.1}$$

where $u_i = x_i' - x_i$ is the displacement with i indicating components in x, y and z directions in the Cartesian coordinate. x_i' and x_i are the position vector after and before the mechanical deformation describing the change of shape and volume of a medium. ρ is material density and σ_{ij} denotes stress tensor. All u_i, σ_{ij} and x_i are both time and spatial dependent, and the time and spatial components are separable as shown in the later part of this section (Eq. (3.20)).

Generally, stress is a function of strain, linked by a tensor coefficient as

$$\sigma_{ij} = \lambda_{ijkl}\varepsilon_{kl} \tag{3.2}$$

where λ_{ijkl} is a tensor of rank four, and is usually termed as elastic modulus tensor or elasticity matrix in COMSOL. If a crystal material possesses any symmetry, the independent elements in the elasticity matrix would be less than 21 [36]. For isotropic materials the stress-strain relation can be reformed into

$$\sigma_{ij} = \lambda \frac{\partial \boldsymbol{u}_k}{\partial \boldsymbol{x}_k}\delta_{ij} + \mu\left(\frac{\partial u_j}{\partial x_i} + \frac{\partial u_i}{\partial x_j}\right) \tag{3.3}$$

where λ and μ are Lamé constants taking charge of the diagonal and off-diagonal part of the strain. $\partial \boldsymbol{u}_k/\partial \boldsymbol{x}_k$ means the sum of the gradient adding all dimensions. The Lamé constants are given by

$$\lambda = \frac{\nu E}{(1+\nu)(1-2\nu)} \tag{3.4}$$

$$\mu = \frac{E}{2(1+\nu)} \tag{3.5}$$

where ν is Poisson's ratio and E is Young's modulus.

To derive the separation of time and spatial components, Eq. (3.1, 3.3) are expanded along x, y, z directions for clearness and are further combined with the mathematical relations of gradient and divergence. The expanded version of Eq. (3.1) is

$$\rho\frac{\partial^2 u_x}{\partial t^2} = \frac{\partial \sigma_{xx}}{\partial x} + \frac{\partial \sigma_{xy}}{\partial y} + \frac{\partial \sigma_{xz}}{\partial z} \tag{3.6}$$

$$\rho\frac{\partial^2 u_y}{\partial t^2} = \frac{\partial \sigma_{xy}}{\partial x} + \frac{\partial \sigma_{yy}}{\partial y} + \frac{\partial \sigma_{yz}}{\partial z} \tag{3.7}$$

$$\rho\frac{\partial^2 u_z}{\partial t^2} = \frac{\partial \sigma_{xz}}{\partial x} + \frac{\partial \sigma_{yz}}{\partial y} + \frac{\partial \sigma_{zz}}{\partial z} \tag{3.8}$$

with the expanded stress tensor σ_{ij} from Eq. (3.3) as

$$\sigma_{xx} = \lambda\left(\frac{\partial u_x}{\partial x} + \frac{\partial u_y}{\partial y} + \frac{\partial u_z}{\partial z}\right) + 2\mu\frac{\partial u_x}{\partial x} \tag{3.9}$$

$$\sigma_{yy} = \lambda\left(\frac{\partial u_x}{\partial x} + \frac{\partial u_y}{\partial y} + \frac{\partial u_z}{\partial z}\right) + 2\mu\frac{\partial u_y}{\partial y} \tag{3.10}$$

$$\sigma_{zz} = \lambda\left(\frac{\partial u_x}{\partial x} + \frac{\partial u_y}{\partial y} + \frac{\partial u_z}{\partial z}\right) + 2\mu\frac{\partial u_z}{\partial z} \tag{3.11}$$

$$\sigma_{yz} = \mu\left(\frac{\partial u_y}{\partial z} + \frac{\partial u_z}{\partial y}\right) \tag{3.12}$$

$$\sigma_{xz} = \mu\left(\frac{\partial u_x}{\partial z} + \frac{\partial u_z}{\partial x}\right) \tag{3.13}$$

$$\sigma_{xy} = \mu\left(\frac{\partial u_x}{\partial y} + \frac{\partial u_y}{\partial x}\right). \tag{3.14}$$

Using the mathematics relation of gradient and divergence

$$\nabla f = \frac{\partial f}{\partial x}\boldsymbol{e}_x + \frac{\partial f}{\partial y}\boldsymbol{e}_y + \frac{\partial f}{\partial z}\boldsymbol{e}_z \tag{3.15}$$

$$\nabla \cdot \boldsymbol{f} = \frac{\partial f_x}{\partial x} + \frac{\partial f_y}{\partial y} + \frac{\partial f_z}{\partial z} \tag{3.16}$$

$$\nabla^2 = \partial_x^2 + \partial_y^2 + \partial_z^2 \tag{3.17}$$

$$\begin{aligned}\nabla\big(\nabla \cdot \boldsymbol{f}\big) = &\left(\frac{\partial^2 f_x}{\partial x^2} + \frac{\partial^2 f_y}{\partial x \partial y} + \frac{\partial^2 f_z}{\partial x \partial z}\right)\boldsymbol{e}_x \\ &+ \left(\frac{\partial^2 f_x}{\partial x \partial y} + \frac{\partial^2 f_y}{\partial y^2} + \frac{\partial^2 f_z}{\partial y \partial z}\right)\boldsymbol{e}_y + \left(\frac{\partial^2 f_x}{\partial x \partial z} + \frac{\partial^2 f_y}{\partial y \partial z} + \frac{\partial^2 f_z}{\partial z^2}\right)\boldsymbol{e}_z,\end{aligned} \tag{3.18}$$

Eq. (3.1) can be recast in to an equation having only one variable defined as $\boldsymbol{u}(\boldsymbol{r},t)$ indicating the vectorial nature of the displacement after it is combined with the material dependent Lamé constants and density as

$$\rho \frac{\partial^2 \boldsymbol{u}(\boldsymbol{r},t)}{\partial t^2} = (\lambda + \mu)\nabla\big(\nabla \cdot \boldsymbol{u}(\boldsymbol{r},t)\big) + \mu \nabla^2 \boldsymbol{u}(\boldsymbol{r},t). \tag{3.19}$$

An Ansatz to Eq.(3.19), which separates of the time $T(t)$ and spatial $\psi(\boldsymbol{r})$ parts of the displacement vector $\boldsymbol{u}(\boldsymbol{r},t)$ has the form of [35]

$$\boldsymbol{u}(\boldsymbol{r},t) = T(t)\psi(\boldsymbol{r}). \tag{3.20}$$

Inserting the Ansatz. (3.20) into Eq. (3.19) results in

$$\frac{\partial^2 T(t)}{\partial t^2} = T(t)\left[\frac{(\lambda + \mu)\nabla\big(\nabla \cdot \psi(\boldsymbol{r})\big) + \mu \nabla^2 \psi(\boldsymbol{r})}{\rho\, \psi(\boldsymbol{r})}\right] \tag{3.21}$$

where the term in the square bracket is time independent but spatial dependent. This demonstrates the validation of the separability of the Ansatz.

In COMSOL implementation, mechanical eigenmode analysis uses Eq.(3.1) to predict the mechanical eigenmode shape. However, as there is no driving term present, the amplitude of each mechanical eigenmode is arbitrary. To obtain the amplitude, driving term needs to be included.

Summary of the notations

u_i is one component of the time and spatial dependent displacement. A sum of all components could be written compactly as

$$\boldsymbol{u}(\boldsymbol{r},t) = \sum_i u_i(\boldsymbol{r},t)\boldsymbol{e}_i. \tag{3.22}$$

The compact version of diagonal strain is in the form of

$$\frac{\partial \boldsymbol{u}_k}{\partial \boldsymbol{x}_k} = \frac{\partial u_x}{\partial x}\boldsymbol{e}_x + \frac{\partial u_y}{\partial y}\boldsymbol{e}_y + \frac{\partial u_z}{\partial z}\boldsymbol{e}_z \tag{3.23}$$

where the bold symbols always mean the sum in all dimensions.

Following the same rule that a bold symbol describes a sum over all dimensions and a symbol with subscribes denotes the physical quantity projected onto a certain dimension, stress and strain can be expressed as

$$\boldsymbol{\sigma} = \sum_{ij} \sigma_{ij}\boldsymbol{e}_{ij} = \sum_k \sigma_k \boldsymbol{e}_k \quad \text{and} \quad \boldsymbol{\varepsilon} = \sum_{ij} \varepsilon_{ij}\boldsymbol{e}_{ij} = \sum_k \varepsilon_k \boldsymbol{e}_k \tag{3.24}$$

where the relation between two and one subscripts in 3D by taking stress as an example lies in

$$\boldsymbol{\sigma} = \begin{bmatrix} \sigma_{xx} & \sigma_{xy} & \sigma_{xz} \\ \sigma_{xy} & \sigma_{yy} & \sigma_{yz} \\ \sigma_{xz} & \sigma_{yz} & \sigma_{zz} \end{bmatrix} = \begin{bmatrix} \sigma_1 & \sigma_6 & \sigma_5 \\ \sigma_6 & \sigma_2 & \sigma_4 \\ \sigma_5 & \sigma_4 & \sigma_3 \end{bmatrix}. \tag{3.25}$$

3.2 Modelling magnetostrictive material

To include the driving term in Eq.(3.1), one straightforward way is to introduce an additional term with the least modification to the original equation. Thanks to the divergence sum relation

$$\nabla \cdot (\boldsymbol{f}_1 + \boldsymbol{f}_2) = \nabla \cdot \boldsymbol{f}_1 + \nabla \cdot \boldsymbol{f}_2 \tag{3.26}$$

that the driving term could be written in the form of an additional stress as

$$\rho \frac{\partial^2 \boldsymbol{u}(\boldsymbol{r},t)}{\partial t^2} = \nabla \cdot \boldsymbol{\sigma}_{\text{total}} = \nabla \cdot \boldsymbol{\sigma}_{\text{ela}} + \nabla \cdot \boldsymbol{\sigma}_{\text{driv}}. \tag{3.27}$$

where $\boldsymbol{\sigma}_{\text{driv}}$ is magnetic field dependent. Stress, strain and external driving magnetic field form the so-called constitutional relation which is described in this section.

The constitutional relation depends on the applications. Therefore, the application required strain property which is related to the choice of the material is discussed first. Terfenol-D and Galfenol are widely used for building ultrasonic transducers, actuators [41, 42], energy harvester [44] etc thanks to their large magnetostriction which enables large mechanical deformation in response to DC or AC external magnetic field. For DC applications, the magnetostrictive saturated strain ε_{max} defined as the ratio of the maximum material elongation to its original length is important, while the so-called magnetostrictive constant, magnetoelasticity or piezomagnetic constant (here we choose piezomagnetic constant [37]), which is the slope on the strain magnetic field plot under a constant stress is key for AC applications. Though Galfenol has good machinability in bulk, Terfenol-D exceeds Galfenol by around 4 times in magnetostrictive saturated strain [45, 54] and more than 3 times in piezomagnetic constant (6.3 nm/A to 310 nm/A vs. 2 nm/A) [46, 54]. For AC magnetometers in our case benefited from the signal enhancement at the mechanical eigenfrequencies, Terfenol-D is chosen.

When a ferromagnetic material is magnetized, its magnetization interacts with external magnetic field causing a body force which can be described by divergence of Maxwell stress tensor [48]. A magnetized material having aligned magnetic dipoles feels the force from the external magnetic field similar to that of a charged particle feeling the force in electrical field. Described in the Lorentz force density in magnetic field $\boldsymbol{f}_L = \boldsymbol{j} \times \boldsymbol{B}$ where $\boldsymbol{j}$ ($\mathrm{A{\cdot}m^{-2}}$) is the current density. In a magnet $\boldsymbol{j} = \boldsymbol{j}_M = \nabla \cdot \boldsymbol{M}$ where $\boldsymbol{M}$ is the magnetization, and $\boldsymbol{j}$ can be further replaced with magnetic field through Ampére's circuital law as $\nabla \times \boldsymbol{B} = \mu_0 \boldsymbol{j}$. This body force can be recast into the form of the Maxwell stress tensor [48, 55] as

$$\boldsymbol{\sigma}_{\mathrm{Maxw}} = \boldsymbol{H} \otimes \boldsymbol{B} - \frac{1}{2\mu_0}(\boldsymbol{B} \cdot \boldsymbol{B})\bar{\bar{\mathbb{I}}} =$$
$$\begin{bmatrix} \frac{1}{2\mu_0}(B_xB_x - B_yB_y - B_zB_z) & H_xB_y & H_xB_z \\ H_xB_y & \frac{1}{2\mu_0}(B_yB_y - B_xB_x - B_zB_z) & H_yB_z \\ H_xB_z & H_yB_z & \frac{1}{2\mu_0}(B_zB_z - B_xaB_x - B_yB_y)\,. \end{bmatrix} \tag{3.28}$$

Assuming the variation of the magnetic field is slow enough for the material to reach deformed equilibrium before further field changes occur and Terfenol-D exhibits reversibility, the stress-strain constitutional relation with modulated AC magnetic field becomes

$$\Delta\boldsymbol{\sigma}_{\mathrm{total}} = \underbrace{\left.\frac{\partial \boldsymbol{\sigma}}{\partial \boldsymbol{\varepsilon}}\right|_H \Delta\boldsymbol{\varepsilon} + \mathscr{O}(\Delta\boldsymbol{\varepsilon}^2)}_{\Delta\boldsymbol{\sigma}_{\mathrm{ela}}} + \underbrace{\left.\frac{\partial \boldsymbol{\sigma}}{\partial \boldsymbol{H}}\right|_\varepsilon \Delta\boldsymbol{H} + \mathscr{O}(\Delta\boldsymbol{H}^2) + \Delta\boldsymbol{\sigma}_{\mathrm{Maxw}}}_{\Delta\boldsymbol{\sigma}_{\mathrm{driv}}} \tag{3.29}$$

$$= \bar{\bar{\boldsymbol{\lambda}}}^{\mathrm{H}} \Delta\boldsymbol{\varepsilon} + \bar{\bar{\boldsymbol{e}}}^{\varepsilon} \Delta\boldsymbol{H} + \Delta\boldsymbol{\sigma}_{\mathrm{Maxw}} \tag{3.30}$$

where $\bar{\bar{\boldsymbol{\lambda}}}^{\mathrm{H}}$ is the elasticity matrix measured under constant magnetic field in COMSOL and it consists of Lamé constants defined by E and ν for isotropic material as can been in Eq.(3.3, 3.4, 3.5). For anisotropic material, the matrix elements of $\bar{\bar{\boldsymbol{\lambda}}}^{\mathrm{H}}$ is governed by Young's molulus and Poisson's ratio with multiple components. $\bar{\bar{\boldsymbol{e}}}^{\varepsilon}$ is a matrix measured under constant strain linking the stress and magnetic field inside the material. Linearised constitutional relation from Eq. (3.30) is under the condition that the magnetic field modulation is small enough and operates far away from $\varepsilon_{\mathrm{max}}$, which is the case in our magnetometers.

The Maxwell stress tensor is added for the sake of physical completeness, it is very small compared with the driving stress. Rough estimation compares $\bar{\bar{\boldsymbol{e}}}$ with $\Delta\boldsymbol{B}$ as they can be think of the coefficients before $\Delta\boldsymbol{H}$. Shown in Tab. 3.1, elements in $\bar{\bar{\boldsymbol{e}}}$ has typical order of 10^3 T while the input AC magnetic field in this thesis is in the order of micro Tesla. Therefore, the contribution from Maxwell stress tensor is negligible.

The expanded constitutional stress-strain and magnetic field relation combined with the elasticity matrix in tensor form is

$$\begin{bmatrix}\Delta\sigma_{\text{total}}\\ \Delta\sigma_{\text{total}}\\ \Delta\sigma_{\text{total}}\\ \Delta\sigma_{\text{total}}\\ \Delta\sigma_{\text{total}}\\ \Delta\sigma_{\text{total}}\end{bmatrix} = \begin{bmatrix}\Delta\sigma^{xx}_{\text{ela}}\\ \Delta\sigma^{yy}_{\text{ela}}\\ \Delta\sigma^{zz}_{\text{ela}}\\ \Delta\sigma^{yz}_{\text{ela}}\\ \Delta\sigma^{xz}_{\text{ela}}\\ \Delta\sigma^{xy}_{\text{ela}}\end{bmatrix} + \begin{bmatrix}\Delta\sigma^{xx}_{\text{driv}}\\ \Delta\sigma^{yy}_{\text{driv}}\\ \Delta\sigma^{zz}_{\text{driv}}\\ \Delta\sigma^{yz}_{\text{driv}}\\ \Delta\sigma^{xz}_{\text{driv}}\\ \Delta\sigma^{xy}_{\text{driv}}\end{bmatrix} = \underbrace{\begin{bmatrix}\lambda^{\text{H}}_{11} & \lambda^{\text{H}}_{12} & \lambda^{\text{H}}_{13} & 0 & 0 & 0\\ \lambda^{\text{H}}_{12} & \lambda^{\text{H}}_{11} & \lambda^{\text{H}}_{13} & 0 & 0 & 0\\ \lambda^{\text{H}}_{13} & \lambda^{\text{H}}_{13} & \lambda^{\text{H}}_{33} & 0 & 0 & 0\\ 0 & 0 & 0 & \lambda^{\text{H}}_{44} & 0 & 0\\ 0 & 0 & 0 & 0 & \lambda^{\text{H}}_{44} & 0\\ 0 & 0 & 0 & 0 & 0 & \lambda^{\text{H}}_{66}\end{bmatrix}}_{\text{elasticity matrix}} \begin{bmatrix}\Delta\varepsilon_1\\ \Delta\varepsilon_2\\ \Delta\varepsilon_3\\ \Delta\varepsilon_4\\ \Delta\varepsilon_5\\ \Delta\varepsilon_6\end{bmatrix}$$
$$+ \underbrace{\begin{bmatrix}0 & 0 & e^{\varepsilon}_{13}\\ 0 & 0 & e^{\varepsilon}_{13}\\ 0 & 0 & e^{\varepsilon}_{33}\\ 0 & e^{\varepsilon}_{15} & 0\\ e^{\varepsilon}_{15} & 0 & 0\\ 0 & 0 & 0\end{bmatrix}\begin{bmatrix}\Delta H_x\\ \Delta H_y\\ \Delta H_z\end{bmatrix} + \begin{bmatrix}\frac{1}{2\mu_0}\left(\Delta B_x\Delta B_x - \Delta B_y\Delta B_y - \Delta B_z\Delta B_z\right)\\ \frac{1}{2\mu_0}\left(\Delta B_y\Delta B_y - \Delta B_x\Delta B_x - \Delta B_z\Delta B_z\right)\\ \frac{1}{2\mu_0}\left(\Delta B_z\Delta B_z - \Delta B_x\Delta B_x - \Delta B_y\Delta B_y\right)\\ \Delta H_y\Delta B_z\\ \Delta H_x\Delta B_z\\ \Delta H_x\Delta B_y\end{bmatrix}}_{\text{external driving stress}}, \tag{3.31}$$

In principle, the external magnetic field changes the material stress, and the additional stress alters the magnetic field through

$$\Delta\boldsymbol{B} = \left.\frac{\partial\boldsymbol{B}}{\partial\boldsymbol{H}}\right|_{\sigma}\Delta\boldsymbol{H} + \left.\frac{\partial\boldsymbol{B}}{\partial\boldsymbol{\sigma}}\right|_{H}\Delta\boldsymbol{\sigma} \tag{3.32}$$
$$= \mu_0\overline{\overline{\boldsymbol{\mu}}}^{\sigma}\Delta\boldsymbol{H} + \overline{\overline{\boldsymbol{d}}}^{\mathsf{T}}\Delta\boldsymbol{\sigma} \tag{3.33}$$

where $\overline{\overline{\boldsymbol{d}}} = [\overline{\overline{\boldsymbol{\lambda}}}^{\text{H}}]^{-1}\cdot\overline{\overline{\boldsymbol{e}}}^{\varepsilon}$ is the piezomagnetic constant and $^{\mathsf{T}}$ indicates the matrix transpose, which in turn modifies the stress. The process then cycles until an equilibrium is reached. Here, equilibrium condition is approximated when using the measurement elasticity and piezomagnetic constants summarized in Tab. 3.1. Therefore, the constitutional relation of magnetic field as a function of stress is not used. However, the relative permeability is still used in defining the Terfenol-D material property. For completeness, the magnetic field stress relation is shown in Eq. (3.33).

In this thesis, measurement data of the elasticity matrix elements $\overline{\overline{\boldsymbol{\lambda}}}^{\text{H}}$ and piezomagnetic constant $\overline{\overline{\boldsymbol{e}}}^{\varepsilon}$ are taken from ref. [56] biased at 60 kA/m and prestressed at 20 MPa summarized in Tab. 3.1.

Table 3.1 **Coefficients in the magneto-mechanical coupling** [56]

unit (GPa)	λ^{H}_{11}	λ^{H}_{12}	λ^{H}_{13}	λ^{H}_{33}	λ^{H}_{44}	λ^{H}_{66}
	107	74.8	82.1	98.1	60	161
unit (T)	e^{ε}_{13}	e^{ε}_{33}	e^{ε}_{15}	no unit	μ^{σ}_{11}=μ^{σ}_{22}	μ^{σ}_{33}
	90	-166	-168		6.9	4.4

The discrepancy from the measurement conditions in ref. [56] leads to the shift of mechanical eigenfrequency, as the eigenfrequency is determined by E and ν which form the elasticity matrix

elements. Nevertheless, the features of magnetomechanical coupling with regard to the driving magnetic field direction are not affected. The axial piezomagnetic constant d_{33} [56] is 10.4 nm/A which is quite conservative compared with other values in the literature (see, e.g. [54] for 310 nm/A). The piezomagnetic constant affects the amplitude of the mechanical oscillation on resonance. The larger the driven amplitude, the larger the actuation will be, thus gaining better thermal noise limited sensitivity.

The external driving stress can be fitted into a 3×3 matrix shown in Eq.(3.25) into the COMSOL solid mechanics module, and the expression for each matrix elements are detailed in Appendix.A.

3.3 Damping selection in COMSOL

In our modelling, damping is manually added to COMSOL to avoid an infinity in amplitude at the mechanical resonance. The selection of damping influences the fitting equation in getting the actuation constant c_{act} in Chapter 3.5, therefore it's important to know how each type of damping in COMSOL affects the mechanical equation of motion.

Damping is added as stress term to Eq.(3.27) as

$$\begin{aligned}\rho\frac{\partial^2\boldsymbol{u}(\boldsymbol{r},t)}{\partial t^2} = \nabla\cdot\boldsymbol{\sigma}_{\text{total}} &= \nabla\cdot\boldsymbol{\sigma}_{\text{ela}} + \nabla\cdot\boldsymbol{\sigma}_{\text{driv}} + \nabla\cdot\boldsymbol{\sigma}_{\Gamma} \\ &= \overline{\overline{\boldsymbol{\lambda}}}^{\text{H}}\nabla^2\cdot\boldsymbol{u}(\boldsymbol{r},t) + \nabla\cdot\overline{\overline{\boldsymbol{e}}}^{\varepsilon}\Delta\boldsymbol{H}(\boldsymbol{r},t) + \nabla\cdot\boldsymbol{\sigma}_{\Gamma}.\end{aligned} \tag{3.34}$$

There are a couple of choice of damping in COMSOL as listed below. In COMSOL the damping stress as a function of damping parameters are given. However how the stress behaves in the equation of motion is not directly known, which is crucial in performing Lorentzian fits in Chapter 3.5. Therefore, the equation of motion in frequency domain including the damping stress term is derived in this section.

The **viscous damping** with manual input parameters η_b and η_v in COMSOL has the form of an additional stress as

$$\boldsymbol{\sigma}_{\Gamma} = \eta_b\dot{\boldsymbol{\varepsilon}}_{bulk} + \eta_v\dot{\boldsymbol{\varepsilon}}_{shear} \tag{3.35}$$

in which η_b is the damping coefficient accounting for the part of the deformation where the volume changes, while η_v is for the part where the material volume stays constant and its shape alters. If we separate Eq. (3.3) into one shear part and the other part of hydrostatic compression with bulk coefficient, one can arrive at [36]

$$\sigma_{ij} = K\frac{\partial\boldsymbol{u}_k}{\partial\boldsymbol{x}_k}\delta_{ij} + 2\mu\left(\varepsilon_{ik} - \frac{1}{3}\frac{\partial\boldsymbol{u}_i}{\partial\boldsymbol{x}_i}\delta_{ij}\right) \tag{3.36}$$

where K and μ are bulk and shear coefficients. For simplicity, we consider one dimensional case where $\sigma = \eta\dot{\varepsilon} = \eta\cdot\partial u(x,t)/\partial x$, together with the one dimensional displacement $u(x,t)$ and magnetic field $H(x,t)$ to examine the influence of viscous damping on the equation of motion in Eq. (3.34). As the separation of bulk ($K = \lambda + \frac{2}{3}\mu$) and shear ($\mu$) part are the linear combinations of Lamé coefficients (λ and μ), it should be safe to simplify the one dimensional stress-strain relation as $\sigma = \lambda^{\text{H}}\varepsilon$.

The integral form of the elastic wave equation is given by

$$\int_S \boldsymbol{\sigma} \cdot \hat{\boldsymbol{n}} dS = \int_V \rho \frac{\partial^2 \boldsymbol{u}}{\partial t^2} dV \tag{3.37}$$

where $\hat{\boldsymbol{n}}$ is the unit vector perpendicular to the surface S.

Taking the Fourier transform of $u(x,t)$ and the driving stress term $H(x,t)$ by inserting

$$u(x,t) = 2\Re\left[\int_0^\infty \tilde{u}(x,\omega) e^{-i\omega t} d\omega\right],\ H(x,t) = 2\Re\left[\int_0^\infty \tilde{H}(x,\omega) e^{-i\omega t} d\omega\right], \tag{3.38}$$

where the tilde $\tilde{H}(x,\omega)$ denotes the AC modulation in frequency domain replacing the ΔH. Then the integral from of the elastic wave equation from Eq. (3.37) when considering the one-dimensional stresses from Eq. (3.34) becomes

$$\lambda^{\mathrm{H}} \int_S \frac{\partial \tilde{u}(x,\omega)}{\partial x} \cdot \hat{n} dS + e^{\varepsilon} \tilde{H}(x,\omega) S_\perp - i\omega\eta \int_S \frac{\partial \tilde{u}(x,\omega)}{\partial x} \cdot \hat{n} dS = -\omega^2 m \tilde{u}(x,\omega) \tag{3.39}$$

where $S_\perp$ denotes the area perpendicular to the magnetic field. To simplify the equation, the frequency domain separation of the displacement, analogous to Eq. (3.20), $u(x,\omega) = X(\omega)\psi(x)$ is used, which results in

$$\lambda^{\mathrm{H}} X(\omega) \int_S \frac{\partial \psi(x)}{\partial x} \cdot \hat{n} dS + e^{\varepsilon} \tilde{H}(x,\omega) S_\perp - i\omega\eta X(\omega) \int_S \frac{\partial \psi(x)}{\partial x} \cdot \hat{n} dS = -\omega^2 m X(\omega)\psi(x). \tag{3.40}$$

Comparing with the standard equation of motion with c_{act} being the actuation constant having the unit of (N/T) as

$$-\omega^2 \tilde{u}(x,\omega) - i\Gamma\omega\tilde{u}(x,\omega) + \Omega_{\mathrm{M}}^2 \tilde{u}(x,\omega) = c_{act}\tilde{B}(x,\omega)/m, \tag{3.41}$$

where Ω_{M} is defined as the mechanical eigenfrequency and Γ (rad·s^{-1}) is the damping parameter, we define the following relation as

$$m\Omega_{\mathrm{M}}^2 = -\lambda^{\mathrm{H}} \frac{1}{\psi(x)} \int_S \frac{\partial \psi(x)}{\partial x} \cdot \hat{n} dS \tag{3.42}$$

$$\Gamma = -\eta \frac{1}{m\psi(x)} \int_S \frac{\partial \psi(x)}{\partial x} \cdot \hat{n} dS. \tag{3.43}$$

As the elements of elasticity matrix λ^{H} have the unit of Pa, the units of the COMSOL input viscous damping η are Pa·s, and that of $\psi(x)$ is m, the derived unit for $m\Omega_{\mathrm{M}}^2$ and Γ from Eq. (3.43) is consistent with the defined unit for mechanical eigenfrequency and damping parameter. c_{act} can be found to be

$$c_{act} = \frac{e^{\varepsilon} S_\perp}{\mu_0 \mu_r}, \tag{3.44}$$

where the relation $\tilde{B}(x,\omega) = \mu_0\mu_r\tilde{H}(x,\omega)$ is used. It can be seen that the actuation constant is determined by the piezomagnetic constant, the area to which the magnetic field is perpendicular and the relative magnetic permeability.

Rayleigh damping also has two input parameters: α_{M} mass damping coefficient and stiffness damping coefficient β_{K}. Their roles in the standard equation of motion are in the form of

$$-\omega^2\tilde{u}(x,\omega) - i(\alpha_{\mathrm{M}} + \beta_K\Omega_{\mathrm{M}}^2)\omega\tilde{u}(x,\omega) + \Omega_{\mathrm{M}}^2\tilde{u}(x,\omega) = c_{act}\tilde{B}(x,\omega)/m \tag{3.45}$$

Loss factor damping is added as external stress with input parameter η as

$$\sigma_\Gamma = \lambda^{\mathrm{H}}(1+i\eta)\varepsilon \tag{3.46}$$

Following the same procedure as in viscous damping: performing Fourier transform to Eq. (3.34) with additional damping stress and followed by an integral, the equation of motion including η then becomes

$$-\omega^2\rho\tilde{u}(x,\omega) + k^2\lambda^{\mathrm{H}}(1+i\eta)\tilde{u}(x,\omega) + \rho\Omega_{\mathrm{M}}^2\tilde{u}(x,\omega) = ik\tilde{H}(x,\omega)e^{\varepsilon}. \tag{3.47}$$

As can be seen the damping term (second term on the right-hand side) is independent of ω, while for both viscous and Rayleigh damping, the damping term is linearly dependent on the velocity. In this model, viscous damping is chosen for the sake of the Lorentzian fitting function in Chapter 3.5.

In later part of the thesis, Ω_{M} is the mechanical eigenfrequencies.

3.4 Magnetic field

The reference magnetic field, which serves as the signal driving the mechanical oscillation of the optomechanical magnetometer, is generated by a pair of Helmholtz coils. As shown in Fig. 3.10, the diameter of the coils is 16 times larger than the lateral size of the device in the centre to ensure that the Terfenol-D in the magnetometers feels the uniformity of the reference magnetic field both in direction and intensity. Therefore, the magnetic field can be simplified to spatial independent expression as $\tilde{B}_0(\omega)$. A subscript 0 indicates the reference magnetic field is characterized in the air media at the location of Terfenol-D.

In COMSOL, the amplitude of the magnetic field is viewed by projection onto the three orthogonal slices. The axis of the pair Helmholtz coils in the Fig.3.1 is in z direction. A sphere filled with air is created to support the generation of the magnetic field as shown in the layout in Fig. 3.10.

A concern with the magnetic field inside the magnetostrictive material is the appearance of eddy current at high frequency driven by the reference magnetic field. When the intensity/direction of the reference magnetic field $\boldsymbol{B}_0$ changes, there creates an induction current. This induction current creates a magnetic field opposing the reference magnetic field and causes most of the magnetic field to exist only between the surface and the skin depth δ_{skin} [57] of the magnetostrictive material. A general form of skin depth is

$$\delta_{\mathrm{skin}} = \frac{1}{\sqrt{\pi f\mu_0\overline{\overline{\boldsymbol{\mu}}}_r\sigma_c}} \tag{3.48}$$

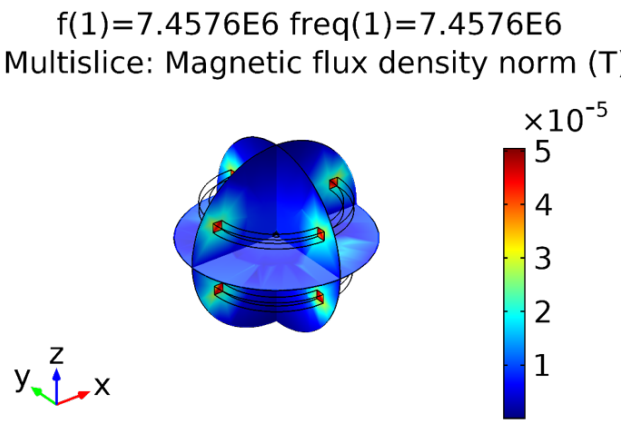

Fig. 3.1 **A pair of Helmholtz coils for generating reference magnetic field.** The intensity of the magnetic field is viewed by colormap projected on three orthogonal slices. As an example, the AC magnetic field is driven by AC current at 7.4 MHz in z direction. The micro device at the center of the intersection of the slices is around 16 times smaller than the coils' diameter.

where σ_c is the conductivity, 1.67×10^6 S/m for Terfenol-D and $\overline{\overline{\boldsymbol{\mu}}}_r$ uses the value from Tab. 3.1. Eq. (3.48) is plotted against driving frequency in Fig. 3.2.

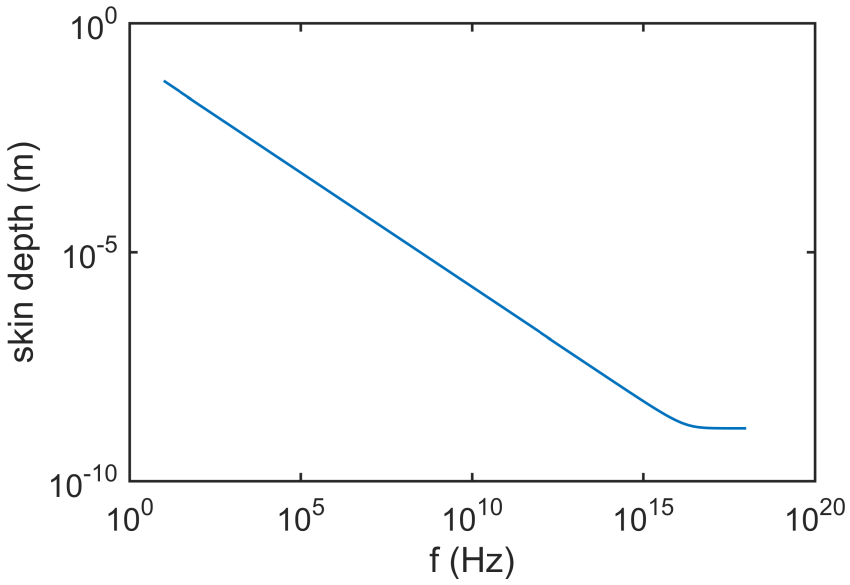

Fig. 3.2 **Skin depth vs. the frequency of the reference driving magnetic field.**

The simulated magnetic field inside Terfenol-D using the COMSOL AC/DC module can be found in Fig. 3.4. The skin effect induced by eddy current starts to play a role when the driving frequency is larger than 1 GHz for a 10s-of-micrometer-sized Terfenol-D droplet, which is consistent with the simple model in Fig. 3.2. For these type of devices whose artistic view in shown in Fig. 3.3, the first order radial breathing mode (RBM) is around 40 MHz, and mechanical modes with eigenfrequency larger than that of the RBM show a decreasing trend of magnetomechanical coupling. Thus, in the

frequency spectrum of interests where mechanical eigenmodes boost the magnetomechanical coupling, the effect of eddy currents can be safely neglected.

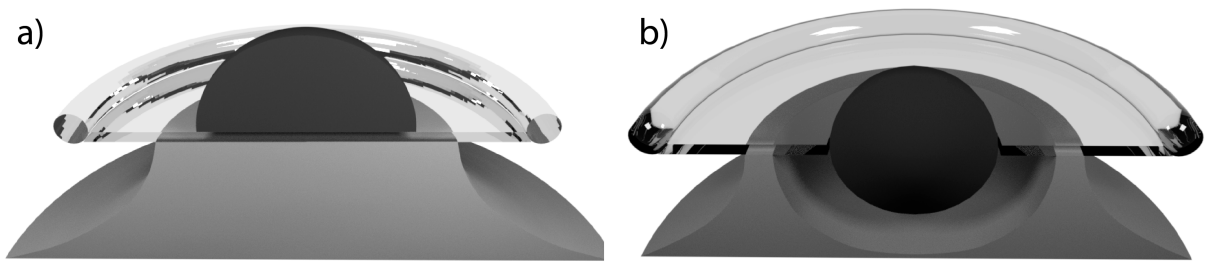

Fig. 3.3 **Cross-sectional view of magnetometers following ref. [26, 27].** Here the Terfenol-D is modelled as a smooth semi-ellipsoid or an ellipsoid.

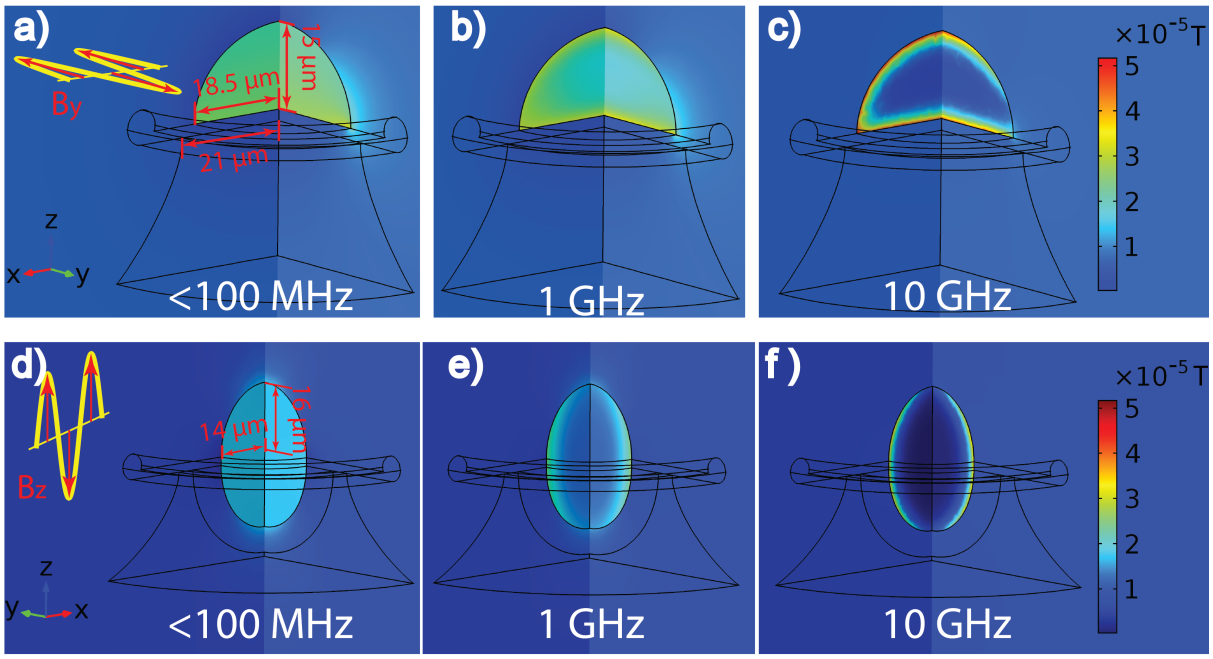

Fig. 3.4 **The effect of eddy current on magnetometers of two geometries as sketched in Fig. 3.3a)-b).** The external magnetic field of a)-c) modulates in y direction (the axis of the pair of Helmholtz coils aligns in y direction), while that of d)-f) is in z direction. The magnetic field intensity is viewed by orthonormal slices same as in Fig. 3.1.

Another concern with the internal magnetic field lies in the fact that the internal magnetic field deforms the magnetostrictive material. Therefore, it is important to know the reference magnetic field polarized the internal magnetic field which is geometric dependent.

Analytical solutions can solve the relation between internal and reference magnetic field in cylindrical geometry. For derivation details of how $\boldsymbol{H}_0$ is related to $\boldsymbol{H}$, please refer to Appendix B. The

result for two simple extreme cases: an infinite long magnetic rod with relative permeability $\overline{\overline{\boldsymbol{\mu}}}_r$ has the internal reference magnetic field relation of

$$\boldsymbol{H}_{\text{inf rod}} = \boldsymbol{H}_0 \tag{3.49}$$

$$\boldsymbol{B}_{\text{inf rod}} = \overline{\overline{\boldsymbol{\mu}}}_r \boldsymbol{B}_0 \tag{3.50}$$

where subscript 0 is the reference magnetic field in the air and this notation is kept throughout this thesis, while the left-hand side is the magnetic field inside the material. And in the other case of thin film with zero thickness, the relation of the reference and internal magnetic field is

$$\boldsymbol{H}_{\text{thin film}} = \boldsymbol{H}_0 / \overline{\overline{\boldsymbol{\mu}}}_r \tag{3.51}$$

$$\boldsymbol{B}_{\text{thin film}} = \boldsymbol{B}_0. \tag{3.52}$$

For COMSOL implementation, the magnetic field in Eq. (3.30) uses the internal magnetic field. The measurement $\overline{\overline{\boldsymbol{e}}}^{\varepsilon}$ parameters summarized in Tab. 3.1 is measured in a cylinder with large axial and traversal aspect ratio [41], where the internal polarized magnetic field is the same as the reference driving magnetic field. When we apply these parameters to our geometry where the scale of the each three dimensions is almost equivalent, the internal and reference magnetic field differs. The COMSOL implementation of internal magnetic field agrees well with the analytical solution.

3.5 Obtaining actuation constant

Actuation constant c_{act} converts the signal magnetic field to a force, which is the key parameter in determining the minimum detectable magnetic field. The way to obtain c_{act} is to fit parameters drawn from COMSOL with modified scaler form of equation of motion from Eq. (3.41) as

$$\frac{\max[\tilde{u}(r,\Omega)] \cdot m_{\text{eff}}}{\tilde{B}(\Omega)} = \frac{c_{act}}{-\Omega^2 - i\Gamma\Omega + \Omega_{\text{M}}^2} \tag{3.53}$$

where $\max[\tilde{u}(r,\Omega)]$ is the maximum displacement of the whole magnetometer. Though it is a vector, for extracting c_{act} by fitting the vectorial information is not important. Ω is adopted instead of previous ω. Maximum displacement and effective mass m_{eff} reduces the calculation for different parts of the whole magnetometer to just one point, which makes the calculation more tangible. m_{eff} quantifies the amount of mass that experiences the maximum displacement in a harmonic oscillation and is calculated through all parts of different material [58, 59]. In one mechanical eigenmode, m_{eff} has the expression of

$$m_{\text{eff}} = \frac{\int_V \rho_i \tilde{u}(r,\Omega)^2 dV}{\max[\tilde{u}(r,\Omega)]^2} = \frac{\int_V \rho_i \psi(r)^2 dV}{\max[\psi(r)]^2} \tag{3.54}$$

where ρ_i is the material density indicating different parts of the device. For devices whose artistic views are shown in Fig.3.3, ρ_i consists of Terfenol-D, silica and silicon pedestal. On the right-hand side of Eq. (3.54), the separation $\tilde{u}(r,\Omega) = \tilde{T}(\Omega)\psi(r)$ is assumed based on the time domain separable

displacement in Eq.(3.20). This separation making the effective mass depends only on the mechanical eigenmodes but not frequency.

All parameters on the left-hand side of Eq. (3.53) can all be drawn from COMSOLs simulation results, while the right-hand side is left for a Lorentzian fit with fitting parameters c_{act}, Γ, and Ω_{M}. As Γ is deliberately input to get rid of unrealistic infinite amplitude, it is chosen to be very small to get rid of possible mechanical interference from neighbouring eigenmodes. However, it is limited by the computer memory and COMSOL numerical tolerance. Then the question can be asked how much would c_{act} change when the input damping varies. Fig. 3.7 a)-c) show the Lorentzian fits for obtaining c_{act} with different input damping parameters to COMSOL. It can be found the relative difference of c_{act} with over 10^4 times variations of the input damping parameters is less than 10%. Therefore, the Lorentzian fitting method in obtaining c_{act} is quite robust against manually input damping. The fitting is based on the toroidal geometry of the magnetometer similar to the art view in Fig. 3.3a). Terfenol-D is modelled as a semi-ellipsoid with transverse radius of 18.5 μm and a height of 5 μm sitting on top of the silica glass. The silica layer has a major radius of 33 μm, thickness of 2 μm and silicon under cut of 9 μm supported by a silicon pedestal. Different from Fig. 3.3a), the Terfenol-D has an offset of 6 μm from the centre. The input elasticity matrix element has the same value as shown in Tab. 3.1, while the magnetostrictive part uses 4 times larger the value of e_{ij}^{ε} than those in Tab. 3.1. The mechanical mode chosen for the analysis is shown in the inset of Fig. 3.7b) with scaling factor $\gg 1$. Fitted parameters and the corresponding input damping is summarised in Tab. 3.2.

Table 3.2 **Fitted parameters with damping for Fig. 3.7 a)-c)**

	a)	b)	c)
input η_b (Pa·s)	2×10^{-4}	2.5×10^{-3}	2.5
input η_v (Pa·s)	1.28×10^{-4}	1.6×10^{-3}	1.6
fitted Γ (rad/s)	$3.2\times2\pi$	$44\times2\pi$	$44000\times2\pi$
fitted $c_{act}(\Omega_{\mathrm{M}})$ (N/T)	3.9×10^{-5}	4.2×10^{-5}	4.2×10^{-5}

In COMSOL implementation, both sides of Eq.(3.53) need to be taken as absolute values. This is due to the phase on a mechanical resonance in COMSOL cannot be written in the form of imaginary part of $[-\Omega^2 - i\Gamma\Omega + \Omega_{\mathrm{M}}^2]^{-1}$ across a mechanical resonance. To extract the COMSOL phase scheme, trigonometry of displacement is used on one or several points on the magnetometers as

$$\phi(\Omega) = \arctan\frac{\Im\tilde{\boldsymbol{u}}(\boldsymbol{r},\Omega)}{\Re\tilde{\boldsymbol{u}}(\boldsymbol{r},\Omega)} = \arctan\frac{\Im\tilde{T}(\Omega)}{\Re\tilde{T}(\Omega)} \tag{3.55}$$

thanks to the decoupling nature of the displacement that the phase and spatial profile are independent. The COMSOL phase across two mechanical resonance is shown in Fig. 3.5 with a zoom-in plot at one mechanical resonance.

To duplicate the numerical phase spectrum across one mechanical resonance. Analytical solution is performed. For frequencies lower than the resonance frequency, the right-hand side of Eq.(3.53) stays as it is by choosing $c_{act} = 1$, while for frequencies higher than the resonance frequency, a π phase shift

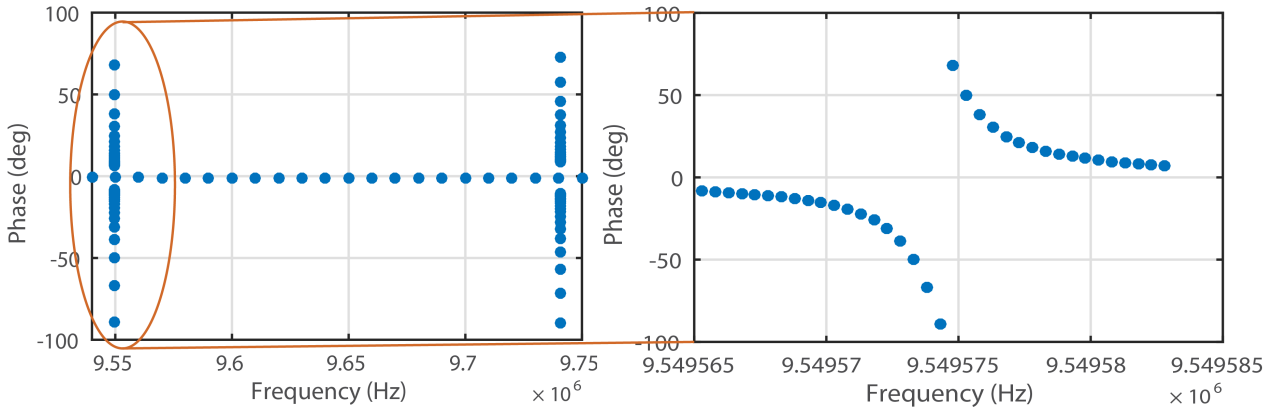

Fig. 3.5 **Phase spectrum across mechanical resonances extracted from COMSOL.** At the exact mechanical resonance frequency, the phase is either 90° or -90°. The left plot shows two mechanical resonances while the right one is zoomed into one of the resonances. Proper damping is added to prevent extreme narrow linewidth at the mechanical resonance frequencies.

is multiplied to the right-hand side as

$$\text{amplitude} = \begin{cases} \dfrac{1}{-\Omega^2 - i\Gamma\Omega + \Omega_{\mathrm{M}}^2}, & \Omega < \Omega_{\mathrm{M}} \\ \dfrac{\exp(i\pi)}{-\Omega^2 - i\Gamma\Omega + \Omega_{\mathrm{M}}^2}, & \Omega > \Omega_{\mathrm{M}}. \end{cases} \tag{3.56}$$

Taking the real part of Eq.(3.56) results the blue scatters in Fig. 3.6d) and taking the absolute value of that gives the orange scatters spectrum. The phase is extracted using Eq.(3.55) as shown in Fig. 3.6c). These analytical plots match the numerical results extracted from COMSOL as shown in Fig. 3.6a)-b). Therefore, taking a modulus to Eq. (3.53) is necessary when one uses COMSOL.

When performing the numerical calculation of the elastic wave equation, damping is chosen to be as small as possible not only to get rid of undesired mechanical interference from neighbouring modes, but also for a clean Lorentzian distributional fit of mechanical displacement spectra.

3.6 Towards obtaining the optomechanical coupling strength

The optomechanical coupling strength G (rad·s^{-1}·m^{-1}) quantifies the shift $\delta\omega_0$ of optical resonance frequency in an optical cavity by the mechanical displacement as

$$G(\Omega_{\mathrm{M}}) = \frac{\delta\omega_0(\Omega_{\mathrm{M}})}{\max[u(r,\Omega_{\mathrm{M}})]} \tag{3.57}$$

The dependence of cavity length change and the shift of optical resonance frequency and thus G is demonstrated via a Fabry-Pérot cavity as shown in Fig. 3.8. Take a lateral breathing mode as an example, standing wave forms when the length L of the cavity equals integer number a of the

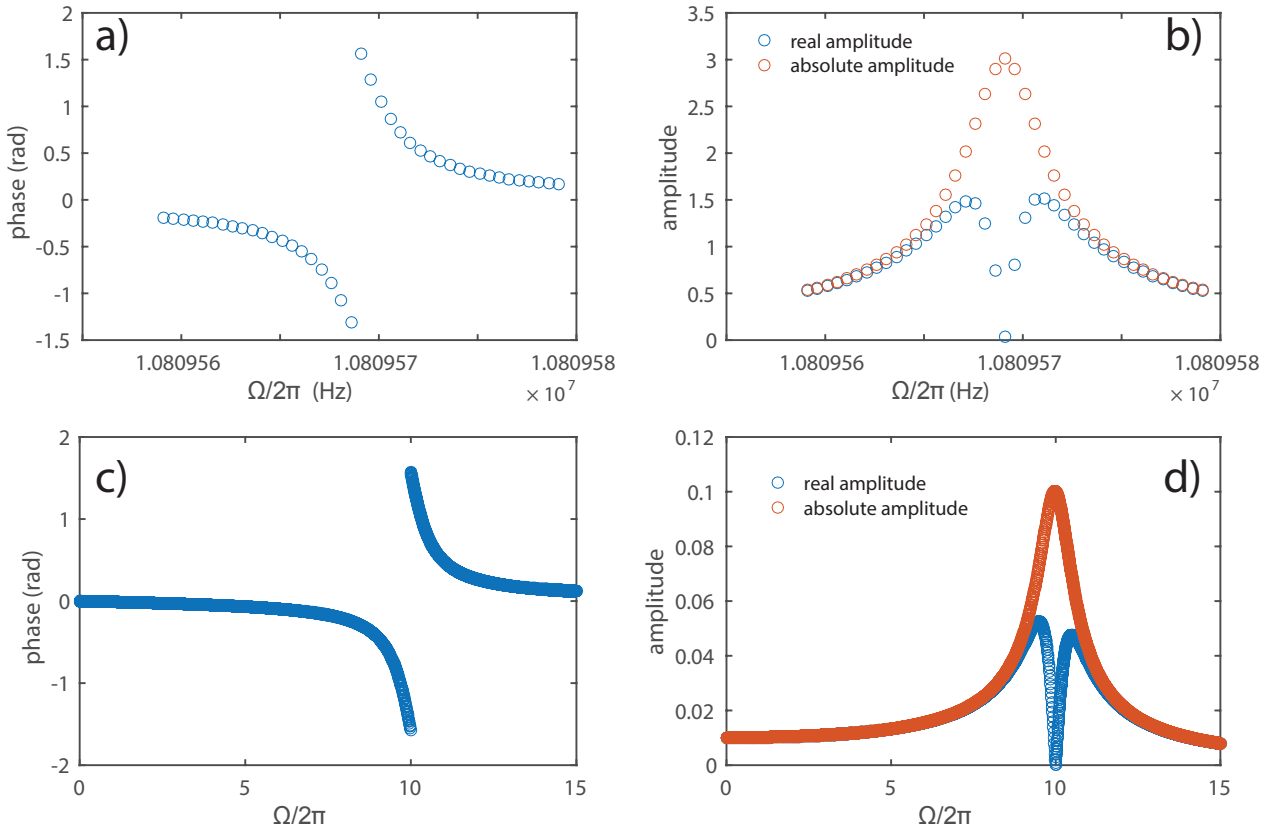

Fig. 3.6 **Real and absolute value of the displacement based on COMSOLs' phase spectrum. a)** Phase spectrum extracted from COMSOL across a mechanical resonance. **b)** Real and absolute amplitude of the maximum displacement extracted from COMSOL. **c)** Analytical reproducing of the phase spectrum and **d)** the corresponding real and absolute displacement.

wavelength λ_o as

$$n_o \cdot L = a \cdot \lambda_o = a \cdot \frac{2\pi c}{\omega_0} \tag{3.58}$$

where $n_o \cdot L$ is the optical path in the cavity counting the refractive index n_0 of the cavity material, c is the vacuum speed of the light. The differential form of Eq. (3.58) is

$$n_o \cdot \delta L = a \cdot \frac{2\pi c \cdot \delta\omega_0}{\omega_0^2}. \tag{3.59}$$

The additional introduced length could be interpreted as a result of breathing mode oscillation. Taking the quotient between Eq.(3.58) and Eq.(3.59) leads to

$$\frac{\delta L}{L} = \frac{\delta\omega_0}{\omega_0}. \tag{3.60}$$

Inserting Eq.(3.60) into the expression of G in Eq.(3.57) results in

$$G = \frac{\delta L \cdot \omega_0}{L \cdot \max[u(r,\Omega_M)]} \equiv \frac{\omega_0}{L} \cdot \xi \tag{3.61}$$

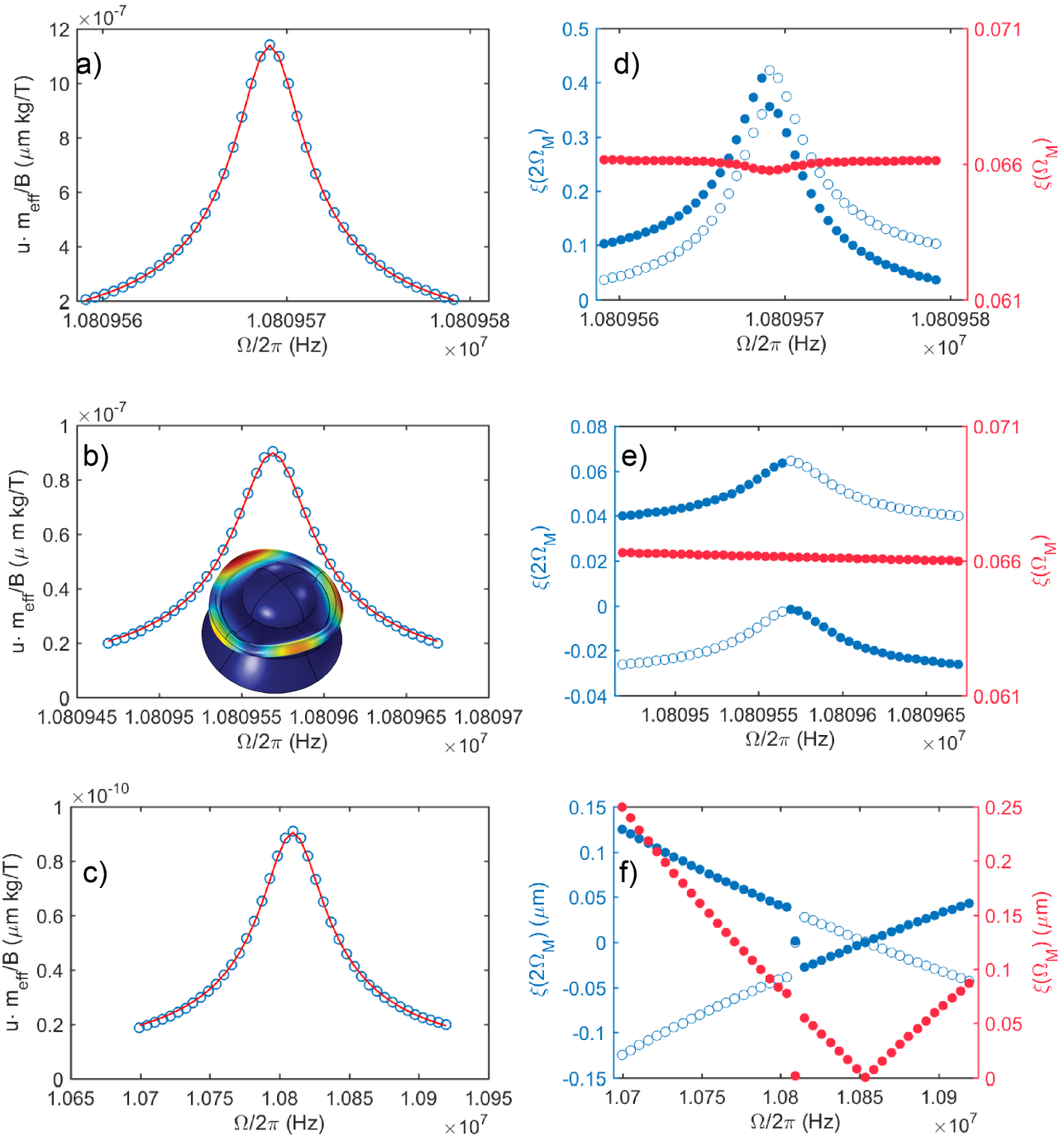

Fig. 3.7 **a)-c)Typical Lorentzian fits for mechanical equation of motion with increasing input damping parameters.** The input damping parameter in **b)** is 12.5 times larger than in **a)**, and that of in **c)** is 12500 times larger than in **a)**. **d)-f) Quadratic and linear $\xi(2\Omega_M)$ and $\xi(\Omega_M)$ with increasing input damping. d), e), f)** has the same input damping as **a), b), c)**, respectively. The smaller the damping, the larger the quadratic effect, while the linear rate is constant. In extremely large damping case as displayed in **f)**, some numerical error may be responsible for the unusual ξ value. The mechanical mode used in this analysis has the shape shown in the **b)** inset with scaling factor $\gg 1$ for the displacement.

$$\xi \equiv \frac{\delta L}{\max[u(r,\Omega_M)]}. \tag{3.62}$$

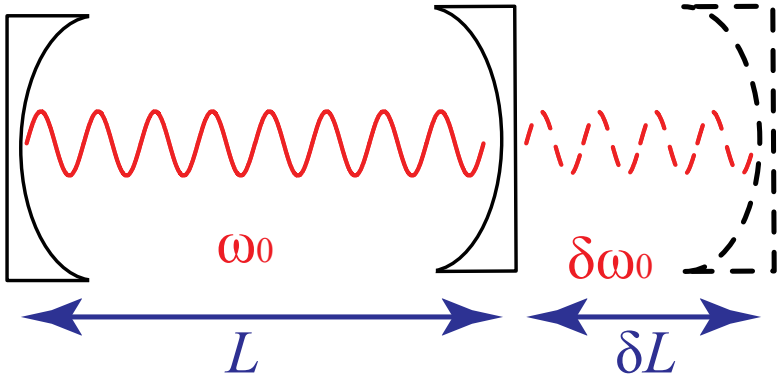

Fig. 3.8 **The relationship between cavity length change and the optical resonance frequency shift illustrated via a Fabry-Pérot resonator.**

For Fabry-Pérot resonator, the maximum displacement is δL, therefore $\xi = 1$ and $G = \omega_0/L$.

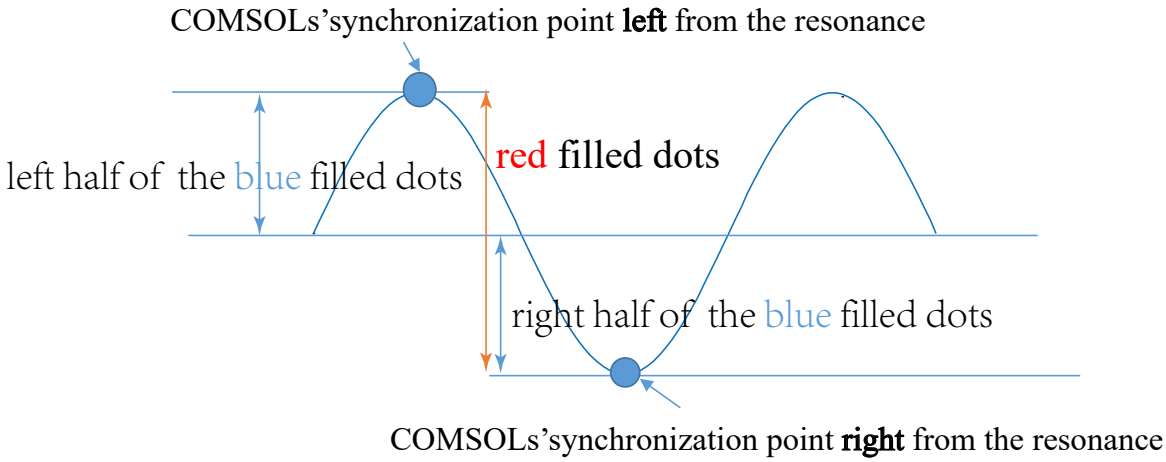

Fig. 3.9 **COMSOL synchronization mechanism within a mechanical resonance.** For frequencies lower than the resonance frequency, the maximum displacement within a period of harmonic oscillation is synchronized to the positive maximum amplitude, while for frequencies higher than the resonance frequency, the amplitudes of which are synchronized to the negative maximum amplitude. The splitting of the synchronization can be understood by the splitting of phase spectrum on resonance as shown in Fig. 3.5. The text explanation is prepared for Fig. 3.7 d)-f).

To obtain ξ, the change of the optical cavity length at the mechanical eigenmodes needs to be extracted from COMSOL. In COMSOL implementation, the optical cavity is in a circular shape which locates at the outermost circumference. The change of the optical cavity length is then equal to the change of the outermost circumference. This is obtained by performing a line integral with integrand 1 along the outermost circumference. However, since it is performed in frequency domain and the change of the circumference needs to be extracted rather than the static geometrical circumference, therefore phase synchronization technique has to be implemented.

The phase synchronization technique is to synchronize the frequency domain amplitudes to the maximum or minimum point of the harmonic oscillation (the synchronization points are show as •

in Fig. 3.9) across the mechanical resonance spectrum. Therefore, the expected outcome from the synchronization is a flat amplitude spectrum instead of a Lorentzian function. The implementation is performed using "moving mesh" in mathematics module of COMSOL. In COMSOL syntax, the implementation is

```
dx=u*exp(-i*atan(imag(u)/(real(u)+1e-16)))
dy=v*exp(-i*atan(imag(v)/(real(v)+1e-16)))
dz=w*exp(-i*atan(imag(w)/(real(w)+1e-16)))
```
(3.63)

where `dx,dy,dz` and `u, v, w` are the displacement after and before synchronization in `x,y,z` directions. 1e-16 in the bracket is an example of adding a small value to eliminate the error of dividing by 0. The circumference obtained from the synchronization of Eq. (3.63) is labelled as $L(0)$. To get a circumference having the phase shift of π a multiplication of $\exp(i\pi)$ to each terms in Eq. (3.63) is needed. The difference of the two circumferences $L(0)$ and $L(\pi)$ results the circumference change at the mechanical frequency. The resulting ξ spectrum is shown in the red dot in Fig. 3.7d)-e) with variations of input damping. The results shows ξ is constant across a mechanical resonance and stays the same for a small variations of input damping with a factor of 12.5 difference. For extremely large damping as shown in Fig. 3.7f), the numerical error is easy to be spotted as ξ is no longer flat.

Out of curiosity, I performed quadratic $\xi(2\Omega_{\mathrm{M}})$ spectrum as shown in blue dots Fig. 3.7d)-f) by calculating $L(0)-L(\pi/2)$ and $L(\pi)-L(\pi/2)$. Two traces are present due to the asymmetry during the oscillation to the maximum and minimum amplitude. Think of a disk (Fig. 3.3) flapping up and down, the disk bending upwards and downwards encounters different boundary conditions (up-Terfenol-D, down-pedestal). Hollow and filled blue dots represent the COMSOL phase splitting scheme which is analytically described by Eq.(3.56). $\xi(2\Omega_{\mathrm{M}})$ is not spectrally flat which is interesting. For high mechanical quality factor, 3×10^6 in the numerical simulation in Fig. 3.7d), the quadratic optomechanical coupling is stronger than the linear coupling. Further studies could be conducted on the quadratic numerical optomechanical coupling combined with experimental observations [60, 61].

3.7 Magnetomechanical coupling

To investigate the mechanical response as a function of the direction of the exciting magnetic field termed as magnetomechanical coupling, the pair of Helmholtz coils used to generate the reference external magnetic field is modelled as having the ability to rotate freely, as shown in Fig. 3.10. Here, the magnetomechanical coupling is demonstrated via a model of Terfenol-D ellipsoid with non-isotropic material nature. Non-isotropy is presented in the elements in elasticity matrix $\overline{\overline{\boldsymbol{\lambda}}}$. Unlike isotropy material where $\overline{\overline{\boldsymbol{\lambda}}}$ is defined by a single-valued Young's modulus E and a single-valued Poisson's ratio ν, the number of irreducible $\overline{\overline{\boldsymbol{\lambda}}}$ elements depends on how asymmetric the material is. Terfenol-D is regarded as transversely isotropic, and thus a little bit complicated than isotropy. The magnetomechanical coupling is performed on transverse isotropic Terfenol-D, and the mechanical eigenmode shape and eigenfrequency are further studied in isotropic consideration of Terfenol-D for comparison.

The Terfenol-D ellipsoid has a radius of 13.4 μm and a height of 14 μm. The transverse isotropic $\overline{\overline{\boldsymbol{\lambda}}}$ matrix elements are taken from Tab. 3.1. Mechanical eigenmode is performed based on the $\overline{\overline{\boldsymbol{\lambda}}}$ input,

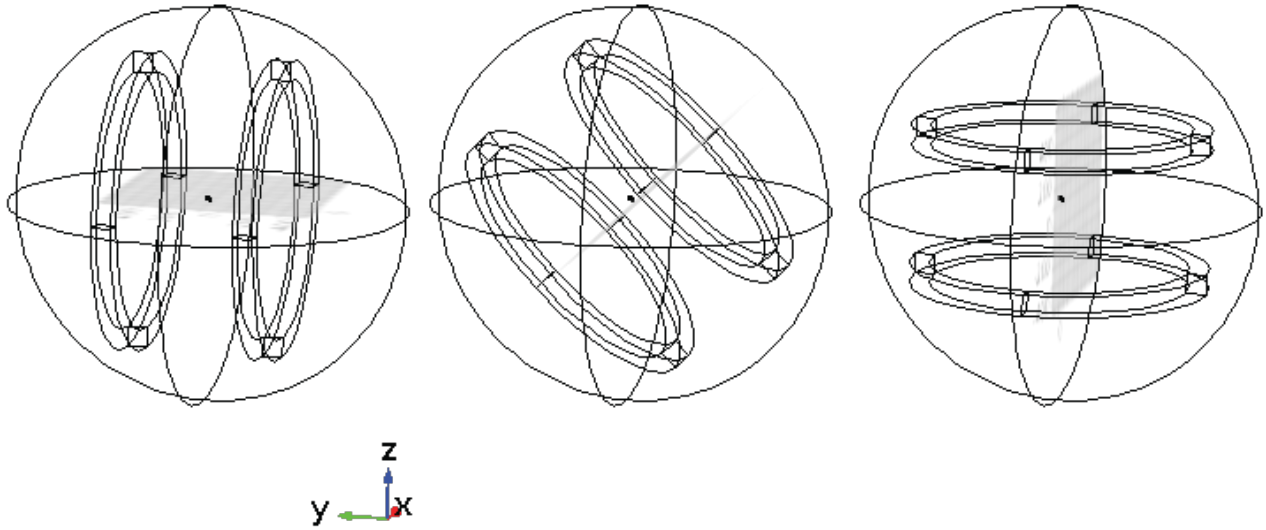

Fig. 3.10 **COMSOL layout of a pair of Helmholtz coils which can rotate freely.** Examples show the ability of coils to produce magnetic field in y, $y-z$ and z directions. The outermost spheres is created to be filled with air to support the generation of magnetic field in COMSOL. The centre spots are the devices under test.

two types of eigenmodes are selected as shown in Fig. 3.11: radial breathing mode (RBM) where most of the mechanical motion takes place in radial direction for a thin disk and due to Poisson's ratio the maximum displacement has both axial and radial components as shown in Fig.3.11b); and Rugby-ball mode where the axial motion swaps orthogonally indicated as dotted line in Fig. 3.11a).

The evaluation parameter of the magnetomechanical coupling is the maximum displacement for simplicity. A complete analysis should be calculating c_{act} as detailed in Chapter 3.5. The tilted rugby-ball mode and RBM are investigated under the excitation of magnetic field in the direction of y, $y-z$ and z axes. The results are summarised in Tab. 3.3.

Table 3.3 **Magnetomechanical coupling.** Maximum displacement amplitude as response to the variation of reference external magnetic field direction for transversely isotropic modelling of Terfenol-D.

	tilted rugby-ball mode at 25.33 MHz	RBM at 29.20 MHz	
coil axial direction	$\max\lvert\tilde{u}(r,\Omega)\rvert$ (μm)	$\max\lvert\tilde{u}(r,\Omega)\rvert$ (μm)	$\xi(\Omega_{\mathrm{M}})$
y	8.6	1.5×10^{-6}	3.4
y-z	4.8	7.8×10^{-3}	6.1
z	3.1×10^{-4}	1.1×10^{-2}	6.1

For the tilted rugby-ball mode, there is a four orders of magnitude increase in the maximum displacement when there is y component of the magnetic field, indicating that an in-plane magnetic field induced stress profile has the similar mode shape as the tilted rugby-ball mode. However, the z direction drive leads to bad magnetomechanical coupling, this is because z direction drive introduces RBM-like stress shape profile having poor mode overlap with the rugby-ball mode. In the case of RBM

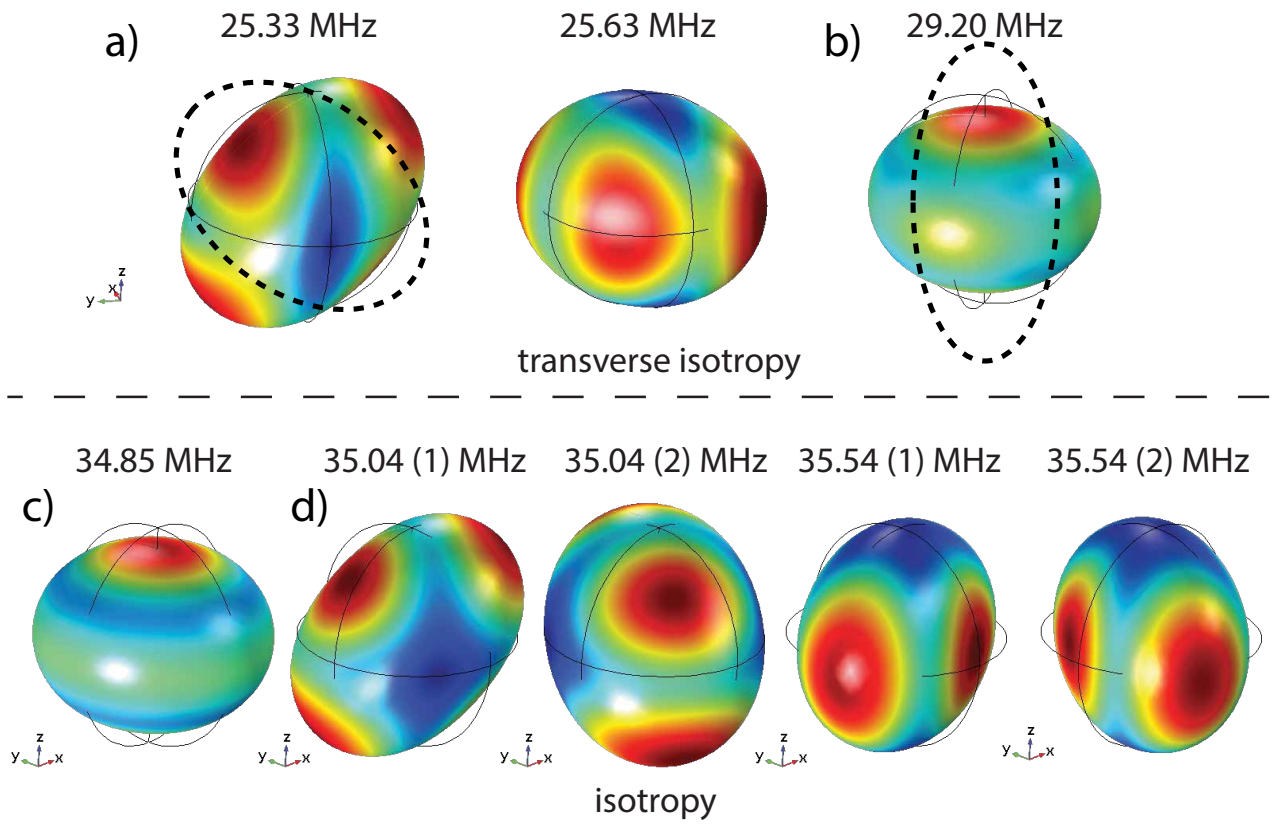

Fig. 3.11 **Spatial shapes of the mechanical RBMs and rugby-ball modes. a)** Rugby-ball modes and **b)** a radial breathing mode from the Terfenol-D modelled as transversely isotropic material. **c)** A RBM and **d)** rugby-ball modes modelled as isotropic material with Young's Modulus of 30 GPa, density of 9250 kg/m^3 and Poisson's ratio of 0.25. A material with isotropic modelling exhibits more degenerated modes for the rugby-ball mode. The black dotted lines indicate mode shape oscillations at mechanical eigenmodes. From left to right the frequency of the mechanical eigenmodes increases.

there is also a four orders of magnitude difference in axially driving and in-plane driving showing a good mode overlap between the driven stress induced RBM-like spatial profile and the mechanical eigen RBM. As well as a poor mode overlap between the in-plane drive induced stress shape and mechanical internal RBM. Note the relative displacement between the rugby-ball mode and RBM is incomparable due to the difference in input damping here.

Though this rough evaluation of magnetomechanical coupling acts on transversely isotropic modelling of Terfenol-D, it can be seen from Fig. 3.11c)-d) that the 1st order RBM and tilted rugby-ball mode indeed exist in isotropic modelling of Terfenol-D where instead of input 6×6 matrix elements (with 12 non-zero) only E and ν is used. The obvious difference lies in the shift of their eigenfrequencies. And for isotropic material, the number of degenerated modes for rugby-ball modes are more than that of in transversely isotropic material, which is reasonable as the axial difference in material crystalline structure lifts the degeneracy for transverse isotropic materials.

The magnetomechanical coupling response is highly sensitive to the direction of the magnetic field as demonstrated with RBM and rugby-ball mode, indicating a possible extension of optomechanical field magnetometer into vectorial magnetometers. The difference of mechanical eigenmode shape between transverse isotropic and isotropic material is relative small for RBM and rugby-ball modes.

However, the eigenfrequency shifts largely. The eigenfrequency of isotropic materials can be analytically solved for thin disk [62, 63] and ellipsoid [33], for traverse isotropic material analytical solution does not necessarily exist [64].

Chapter 4

Numerical Prediction of Bandwidth and Sensitivity

The mechanical properties derived from the numerical simulation in Chapter 3 combined with the optomechanical anaylsis for homodyne detection scheme in Chapter 2 are applied to previous experimental devices [26, 27, 32] showing that the predicted sensitivity is still one order of magnitude better than the experiments have achieved. This analysis is further applied to study the effect of bending and the size of the magnetostrictive material on sensitivity and optomechanical coupling rate, as well as whether the bandwidth can be improved as a result of laser detuning and increased optical power for different geometries.

4.1 Single mechanical mode analysis

For a single isolated mechanical eigenmode without interference from other eigenmodes, the minimum detectable magnetic field in the presence of thermal Brownian noise, imprecision noise and back-action noise in homodyne detection scheme is given by Eq.(2.63) with the mechanical susceptibility in Eq. (2.19) and the effective cooperativity expressed in Eq. (2.13). In this section I use these equations to determine the idealized single-mode performance of the optomechanical magnetometer assuming the overall detection efficiency $\eta = 1$, which leads to the input laser power being smaller than real situations when loss is considered.

The first edition magnetometer developed in our laboratory [26] is a standard toroid resonator with a silica major radius of 33 μm, torus radius of 3 μm, thickness of 2 μm and silicon undercut of 9 μm, and with an empirical optical quality factor of 2×10^7 after a CO_2 laser reflow process. The Terfenol-D blob sitting on top of the silica is modelled as a semi-sphere with a transverse radius of 18.5 μm and a height of 15 μm. The mechanical quality factor is assumed to be 200 for all modes which is a simplification compared to experimental observations, but is broadly in line with the experimentally observed quality factors. A cross-sectional art view is shown in Fig. 4.1c) for Terfenol-D in the centre and being displaced.

Mechanical properties including eigenfrequency Ω_{M}, actuation constant c_{act}, the ratio of circumference change to maximum displacement ξ and effective mass m_{eff} are extracted from COMSOL where the magnetometer is driven by an external reference magnetic field B_{ref} with a direction in

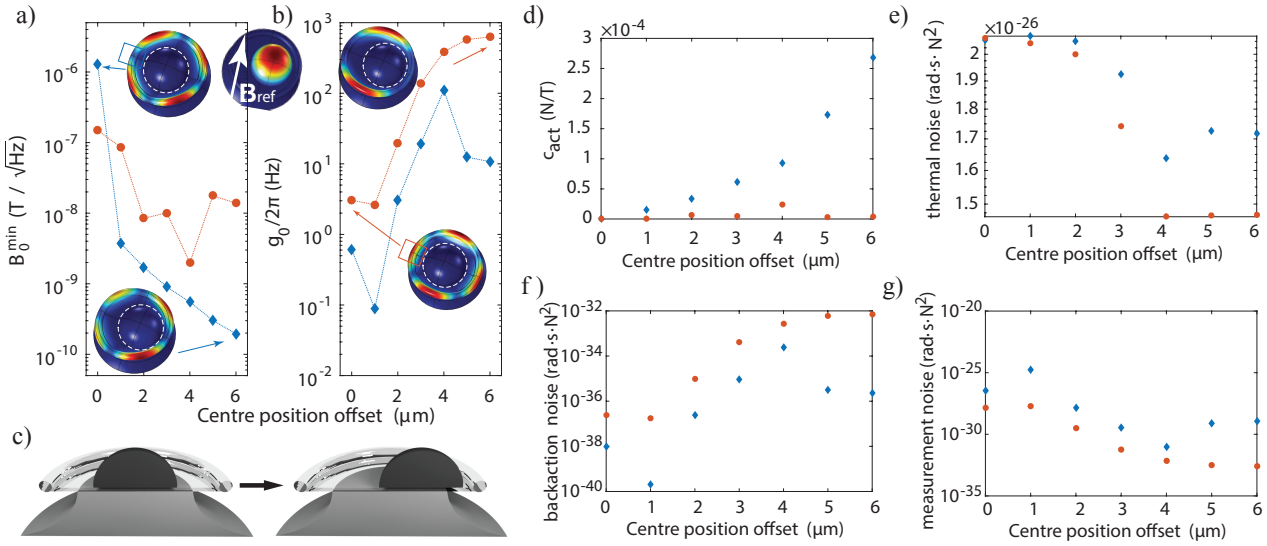

Fig. 4.1 **Single mechanical mode analysis** for **a)** the sensitivity and **b)** the vacuum optomechanical coupling rate in the presence of Terfenol-D position offset. **c)** An illustration of the 1st generation optomechanical magnetometer with the evolution of Terfenol-Ds' position. **d)** Actuation constant and noise contributions from **e)** thermal bath, **f)** back-action and **g)** measurement imprecision for the degeneracy-lifted two 2nd order crown modes. Inset between **a)** and **b)** is the spatial profile induced by the reference magnetic field.

plane. With the input of laser power, detuning from the optical cavity and wavelength, we can arrive at the quantitative contribution from each noise source, and thus the noise limited sensitivity of the magnetometer can be derived.

Start with centred Terfenol-D, without loss of generality, a pair of frequency-degenerated 2nd order crown modes are chosen because they have been experimentally observed quite often [65, 66]. The mechanical mode shape shown in Fig. 4.1a) upper inset is called mode 1, and in Fig. 4.1b) lower inset is called mode 2. The scaling factor of the eigenmodes are $\gg 1$ demonstrating only the relative displacement amplitude in the device matters. The difference between the two modes lies in the torus displacement amplitude at the location highlighted by a blue and orange rectangular. The usage of the color in the plots of Fig. 4.1 is associated with the mechanical mode: mode 1 for blue and mode 2 for orange. The effective motional mass is $m_{\text{eff}} = 3.9$ pg with eigenfrequency at 10.1 MHz and $\xi < 10^{-3}$, $c_{act} \sim 10^{-6}$ (N/T) for the magnetometer with centred Terfenol-D. This ξ is 10^4 smaller than that of the thin disk radial breathing mode which is 4π, showing the hardness of the optical detection of the mechanical motion of the 2nd order crown mode. The numerical accuracy affected by the mesh is characterized using a thin isotropic disk where no less than 10 mesh points are distributed along the radius, a half cycle $\xi(2\Omega)$ parameter is used for characterization with the numerical value of 6.194. Compared with analytical value of 2π, mesh induced inaccuracy is as low as a relative 1.4%, thus this fineness of the mesh is kept.

The parameters of the coherent input laser is chosen to be: a wavelength of 980 nm, a power of 2 μW, and the laser frequency is locked on one resonance of the optical cavity. The power spectral density of the noise force can then be calculated via Eq. (2.63), so that the dominant noise source can be derived. The thermal noise force spectral density of $2{\cdot}10^{-26}$ rad·s·N^2 (Fig. 4.1e)) is more than 5 orders of magnitude smaller than the back-action noise (Fig. 4.1f)) around $10 \cdot 10^{-38}$ rad·s·N^2 for mode

1 ($2 \cdot 10^{-31}$ rad·s·N^2 for mode 2), and more than 1 order of magnitude smaller than the measurement imprecision noise (Fig. 4.1g)) around $1 \cdot 10^{-27}$ rad·s·N^2 for mode 1 ($1 \cdot 10^{-28}$ rad·s·N^2 for mode 2), showing a thermal noise dominated nature of this optomechanical magnetometers system. Though vacuum optomechanical coupling rate g_0 (Eq. (2.8)) is independent on the input laser power, it relies on the laser wavelength and geometry of the device, and it is replacing ξ in the following as g_0 is one of the key parameters in the optomechanical community quantifying how well the mechanical motion can be optically read out. An exampled conversion between optomechanical coupling strength and ξ parameter for the 2nd crown modes is $g_0/2\pi = 8.5 \cdot 10^3$ Hz for $\xi = 4\pi$ for the 1st generation optomechanical magnetometer's geometry. The thermal noise limited sensitivity for the two 2nd crown modes are around microtesla, which can be viewed from Fig. 4.1a).

As Terfenol-D is moved away from the centre, mode 1 experiences a monotonous increase in sensitivity while an overall increasing trend is visible for the mode 2 as shown in Fig. 4.1a). The evolution of the offset of the Terfenol-D is depicted in Fig. 4.1c). Fig. 4.1b) shows more than 2 orders of magnitude enhancement in g_0 with only a few micrometre Terfenol-Ds' offset. The improvement in sensitivity and optomechanical coupling rate is likely due to the bending effect taking place at the edge of the pedestal. Similar to the bimetallic bending effect, Terfenol-D with offset gives additional strain to silica during the downwards flipping thus increasing the flipping amplitude and consequently sensitivity. While the Terfenol-D helps increase silica amplitude when flipping downwards, it obstructs silica to flip upwards, thus creating a large circumference difference between flipping upwards and downwards and consequently increasing g_0. Mode 1 has better optomechanical coupling than mode 2, which depends on the position of the Terfenol-D as well as the direction of the external magnetic field. The reference-magnetic-field-induced mode profile can be viewed in Fig. 4.1a)-b) inset. It has a maximum displacement towards the direction of B_{ref} creating a single direction height slope along B_{ref}. And crown mode 1 with Terfenol-D offset (see in Fig. 4.1a) lower inset) where the neighbouring quarters of torus having opposite flipping directions also have a height slope along the direction of B_{ref}, while in B_{ref} direction mode 2 has quarter toruses both flipping in the same direction (see in Fig. 4.1b) upper inset) having no height slope across the device. On the other hand, mode 2 has better g_0 because the Terfenol-D (highlighted with white dot line on the shape of the mechanical eigenmodes in Fig. 4.1a)-b) inset) is moving towards the torus amplitude anti-node where the highlighted rectangle is. Thus, the Terfenol-D enhances the the amplitude of the displacement of the quarter torus nearby more efficiently than in mode 1 where the Terfenol-D is moving towards the node of the displacement amplitude of the torus when the torus flips downwards, and the Terfenol-D suppresses the torus motion more efficiently when the tours flips upwards in mode 2 than in mode 1, thus creating larger circumference change and larger g_0 in crown mode 2 than in mode 1.

The numerical results predict that sub-nano T/$\sqrt{\text{Hz}}$ sensitivity is possible with optimal offset, which is 3 orders of magnitude better than experimental result [26]. The experimental results are likely to be degraded not only due to a lack of Terfenol-D offset, but also by the glue associated with the Terfenol-D deposition, which reduces the expansion of the silica disk.

Linear optomechanical coupling depending on g_0 should be 0 for perfect symmetrical crown modes of the toroidal/disk structure as there is no change of circumference in one harmonic oscillation. However, thermal noise of crown mode is observed with very high signal-to-noise ratio (SNR) [66, 65], the uniformity of mass and geometrical symmetry broken by defects [67] could be one

explanation. Fig. 4.1b) offers a numerical proof of the fact that symmetry break of the devices enhances optomechanical coupling. Quadratic optomechanical coupling of a lower frequency mode could be an alternative explanation of resolvable thermal noise spectrum for crown modes. However, it is very hard to distinguish between the contributions from the quadratic optomechanical coupling of a lower order crown mode at half the eigenfrequency and the linear optoemechanical coupling thanks to the defects. For instance, the 2nd order and 3rd order crown modes in ref.[66] are of half the frequency from one to the other.

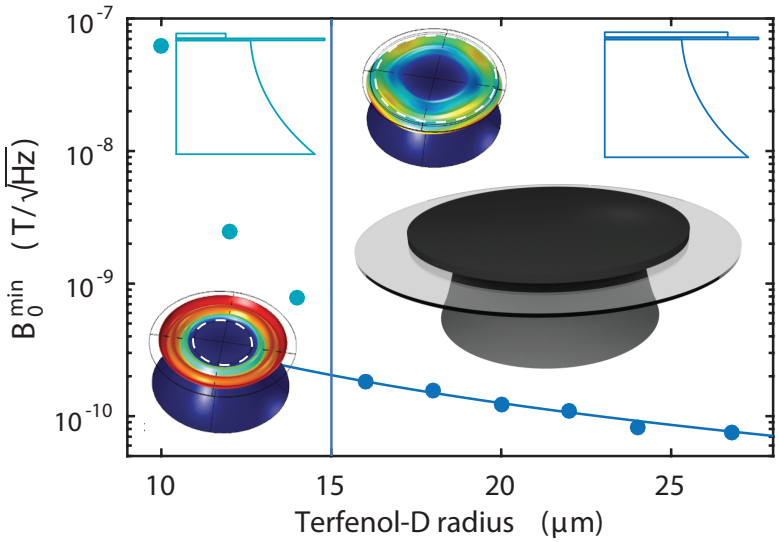

Fig. 4.2 **Single mechanical mode analysis for sensitivity as a function of the radius of the Terfenol-D**

The single mechanical mode analysis is then applied to a thin disk structure with 1-μm-sputter-coated-Terfenol-D film on top of a 400-nm-thick silica disk. Magnetometers with sputter coated Terfenol-D have the advantage of high repeatability ready for characterization of elasticity matrix elements and piezomagnetic constants under experimental environment for accurate modelling prediction and for further improvement. The silica disk has a radius of 30 μm and the pedestal has a top facet of 15 μm in radius which serves as a vertical guideline in Fig. 4.2 for comparison with the size of Terfenol-D. The optical quality factor is set to be 1×10^6, and 12.8 μW of input laser at 1550 nm is sent to the homodyne detection with zero detuning. The effective mass, m_{eff}, extracted from numerical simulation various from 1 pg to 3.8 pg with the expansion of Terfenol-D size of the radial breathing mode.

Fig. 4.2 shows the relation of sensitivity and Terfenol-Ds' size for the 1st order RBM. The external reference magnetic field sweeps in the axial direction to create a stress-induced-profile having a large mode overlap with RBM, thus boosting the amplitude of radial displacement. The part of Terfenol-D (highlighted with white dotted line in mechanical eigenmode simulation) inside the top pedestal facet is motionless, while the rim outside the top pedestal facet of the Terfenol-D has the mechanical motion hybridized with the silica disk mode. The sensitivity scales with the motional part of the Terfenol-D in addition to the magnetomechanical coupling. Sub-hundred $\text{pT}/\sqrt{\text{Hz}}$ sensitivity is predicted when the diameter of the Terfenol-D disk covers more than 2/3 of the silica disk. A powers fit (y(x)=a$\cdot x^b$ with

fitting results of a=2×10^{-8} and b=-1.7) is exploited to the data with Terfenol-D radius larger than the pedestal, indicating that a 300-μm-radius of Terfenol-D would lead to 1 pT/$\sqrt{\text{Hz}}$ sensitivity. To get better sensitivity, the size of the Terfenol-D has to be larger than the pedestal so as to have large portion of motional Terfenol-D, which could be realised by increasing the silicon pedestal undercut and the size of Terfenol-D.

4.2 Multiple mechanical modes analysis

Depending on the relative $g_0(\Omega_M)$ among multiple mechanical eigenmodes, the thermal Brownian motion of some of the mechanical modes with small optomechanical coupling would be buried under that of other mechanical modes in a broad spectrum. That is to say even if one mechanical mode has high coupling to the force from the magnetostrictive material, it might still be unresolvable due to the large thermal mechanical noise of nearby mechanical modes imprinted on the optical field. Fortunately, in experiments those high actuation mechanical modes are still resolvable thanks to the defects and asymmetry discussed in Chapter 4.1. To gain the knowledge of optomechanical coupling strength in a broad spectrum consisting of multiple mechanical eigenmodes, the thermal noise spectral density of the light phase quadrature (Eq. (2.36)), the network response (Eq. (2.60)) and the minimum detectable magnetic field (Eq. (2.61)) is calculated accordingly. The calculation is based on accurate extraction of mechanical properties from COMSOL, combined with input laser parameters. Only optical and mechanical quality factors are empirically determined. The network response is the sensor response spectrum to the magnetic field including mechanical interference among eigenmodes induced by coherent magnetic force driving.

Fig. 4.3a) shows the thermal noise spectral density when the input 980 nm laser is locked on the optical cavity resonance with 2 μW of power for a 1st generation magnetometer. Shot noise from a coherent laser is 1/2 uniformly across all frequencies, because the optical field having high frequency is assumed in a vacuum state and normalised to zero point motion [49]. Mechanical eigenmodes for the first five low frequency modes are simulated in the inset (scaling factor $\gg$1) with the Terfenol-Ds centre position offset. Without offset, the mechanical modes with frequency from low to high is shown in Fig. 4.3f). Fig. 4.3b) ensures that the silica RBM having a high optomechanical coupling rate g_0 hybridized with the Terfenol-D motion does not cover the thermal motion of the first five modes. As there seems to be existing of infinity number of mechanical eigenmodes for a given geometry and the number of eigenmodes being analysed is limited, it is important to include high g_0 mode even if it's not within the region of interest to make sure the thermal noise peak of the modes of interest can be resolved. The network response is obtained with the external reference magnetic field sweeping in plane. Black triangles in the sensitivity spectrum are calculated for individual modes (Eq. (2.63)) neglecting the back-action noise, while the blue continuous line presents the sensitivity as a result of interference in the signal between different mechanical modes. Fig. 4.33) shows comparison of cooperativity C (Eq. (2.12)) which is the approximation with bad cavity limit and effective cooperative $|C_{\text{eff}}|$ (Eq. (2.11)) for each individual eigenfrequency, showing a bad cavity limit is not very accurate here, therefore C_{eff} is used. The vacuum optomechanical coupling rate of several hundred on average for the first five mode is comparable to the radial breathing mode thanks to the enhancement for the Terfenol-Ds offset (Fig. 4.3d)). The predicted sensitivity is 100 pT/$\sqrt{\text{Hz}}$ at 12 MHz among the

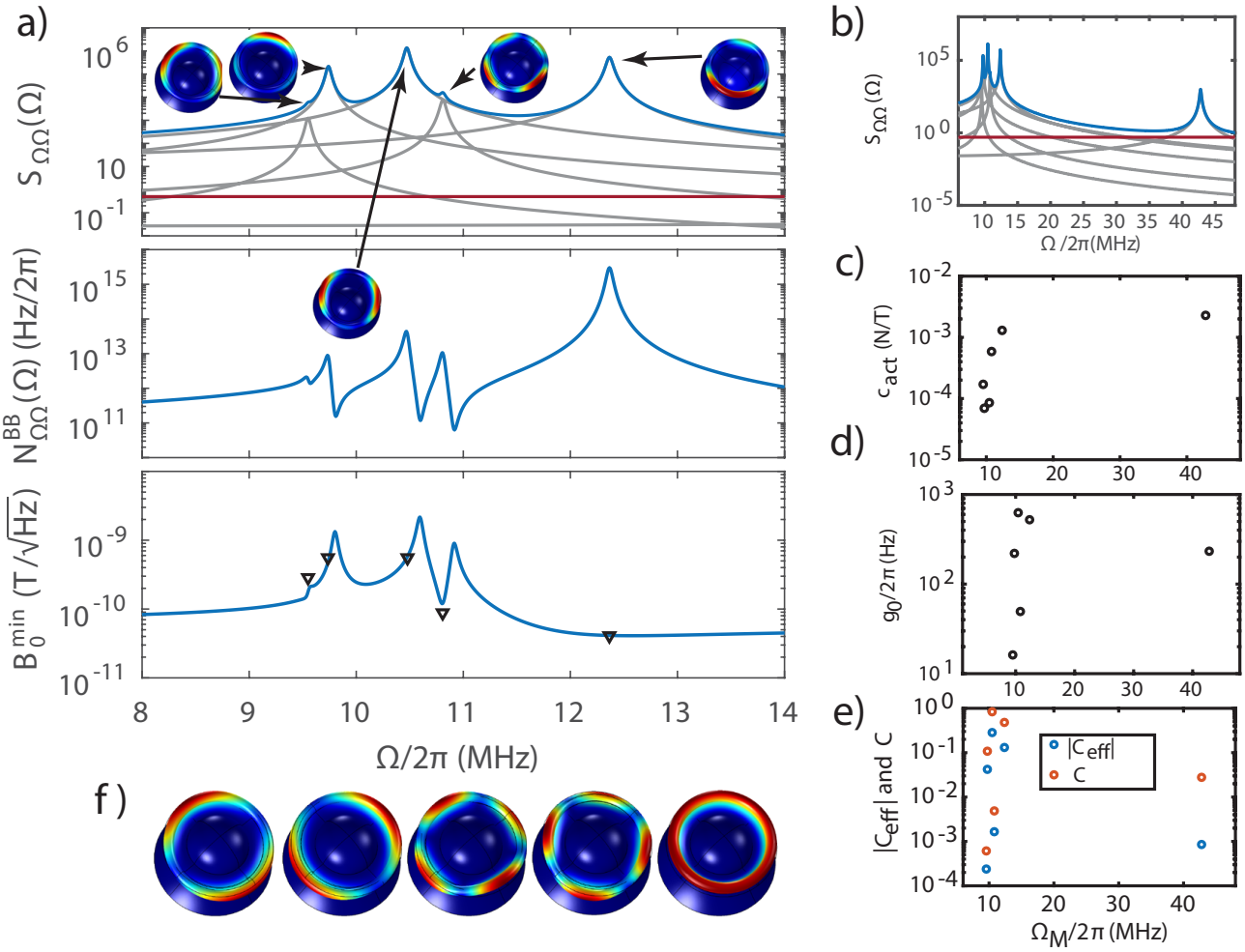

Fig. 4.3 **Sensitivity spectrum prediction for the 1st generation magnetometers. a)**Top: thermal noise spectral density $S_{\Omega\Omega}(\Omega)$ (blue) is the sum of individual thermal noise peaks (grey) and the normalized (to optical zero-point motion) laser shot noise (red). Middle: network response $N^{BB}_{\Omega\Omega}$ records the magnetomechanical coupling under in-plane reference magnetic field driving. Bottom: black triangle is the sensitivity for individual mechanical modes. **b)** Thermal noise spectral density shows the first five mechanical modes are not buried under the silica RBM at 42.7 MHz. **c)** Actuation constant, **d)** vacuum optomechanical coupling rate, **e)** cooperativity and effective cooperativity of each individual mechanical eigenmodes. **f)** Mechanical eigenmodes without Terfenol-D offset from left to right corresponding to eigenfrequencies from low to high.

first five modes, which is consistent with its highest actuation constant c_{act} as shown in Fig. 4.3c). Mechanical eigenmodes with high SNR of thermal Brownian motion and high c_{act} lead to resolvable high sensitivity.

Mechanical modes upto 45 MHz are selectively analysed in three windows (in the inset of Fig. 4.4a) displays thermal noise around ∼7 MHz, ∼26 MHz and ∼43 MHz) of interest with external reference magnetic field sweeping in plane, the same condition in experiments [27, 32] of the 2nd edition magnetometers, the artistic view of which is shown in Fig. 3.3b) and the geometry of which is labelled in Fig. 3.4. High order mechanical modes (eigenfrequency > 1st silica RBM) are difficult to drive, leading to relative poor sensitivities. Though these modes have small thermal noise, it it unlikely for them to have large g_0 to stand out among other thermal noise peaks. Therefore, they are not here for consideration in this numerical simulations.

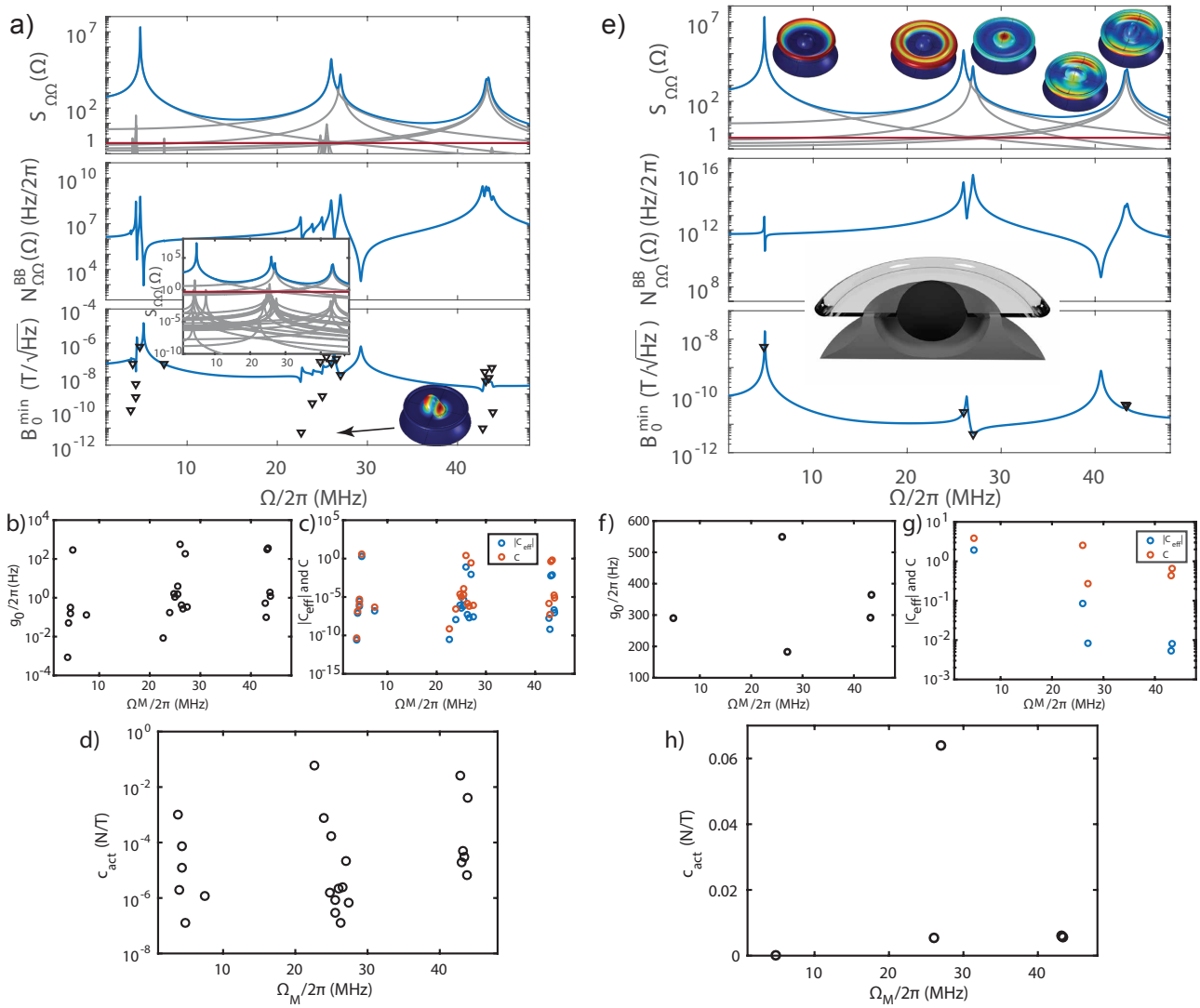

Fig. 4.4 **Thermal noise spectral density, network response and sensitivity for the 2nd generation magnetometers** driven by an in-plane **a)-d)** and axial **e)-h)** reference magnetic field with cooperativity, vacuum optomechanical coupling rate and actuation constant on mechanical resonances of interest. An art view of the cross section is shown in **e)** inset for the 2nd generation magnetometers [27].

From mechanical property analysis, the effective mass m_{eff} is obtained as 13.4 pg, 10.4 pg, 39 pg, 25 pg and 18 pg for the resolved thermal noise peak at 4.8 MHz, 26 MHz, 27 MHz, 43.2 MHz and 43.4 MHz. The larger the Terfenol-D motional part is, the heavier the effective mass would be, which is consistent with the material density that $\rho_{\text{Terfenol}-\text{D}}$ (9250 kg·m^{-3}) $> 3\rho_{\text{silica}}$ (2203 kg·m^{-3}). If the Terfenol-Ds' eigenmode motion could be coupled well to the driven induced spatial profile, then that eigenmode would leads to high sensitivity.

The coherent input laser has parameters: 5 μW input power, 1550 nm wavelength and on-resonance homodyne detection scheme. Analysis shows that though a single mechanical mode (dominated by Terfenol-D motion) at $\Omega_{\text{M}}/2\pi$=23 MHz having large $c_{act}^{\parallel}$ =0.058 N/T reaches 5.6 pT/$\sqrt{\text{Hz}}$ thermal noise limited sensitivity, this particular mode with heaviest m_{eff}=57 pg indicating a largest portion of motional Terfenol-D has very weak optomechanical coupling when the device is modelled uniformly and transverse-symmetrically (see Fig. 4.4a) inset for (scaling factor $\gg$1) numerical mechanical eigenmode). Note this Terfenol-D mode is termed as tilted rugby-ball in Chapter 3.7.

Mechanical modes having radial breathing motion components stand out in the thermal noise spectrum shown in Fig. 4.4a) inset, for their large vacuum single photon optomechanical coupling rate g_0 as shown in Fig. 4.4b), e) on the order of 100-1000 Hz. Without modelling the influence of defects in increasing the optomechanical coupling, we focus on RBMs driven with reference magnetic field in the axial direction. Stress induced spatial profile exhibits RBM-like motion under axial magnetic field driving due to Poisson's ratio in elastic materials, having a good spatial mode overlap with the mechanical radial breathing eigenmodes to boost radial displacement amplitude thus achieving large $c_{act}(\Omega_M)$. Thermal noise spectral density, signal response and minimum detectable magnetic field plots with axial reference magnetic field driving are shown in Fig. 4.4d). Among the 5 high g_0 mechanical modes, the Terfenol-D RBM at $\Omega_M/2\pi = 27$ MHz reaches a sensitivity of 5 pT/$\sqrt{\text{Hz}}$ (see Fig. 4.5 for the zoom-in sensitivity of the same mechanical mode) where single (in black triangle using Eq. (2.63)) and multiple (in blue line using Eq. (2.61)) mode analysis overlaps. The corresponding $c_{act}^{\perp}(\Omega_M/2\pi$=27 MHz)=0.064 N/T for axial reference magnetic field sweep, while the same mode has a $c_{act}^{\parallel}(\Omega_M/2\pi$=27 MHz)=$2\times10^{-5}$ N/T for in-plane sweep, showing a substantial difference of good and bad magnetomechanical coupling. A hybridized Terfenol-D RBM (large c_{act}) with silica RBM (large g_0 for being resolved) is an idea case, which needs carefully matching the sound propagation time in different part of the materials in the magnetometer for future design.

Several interesting parameters of each individual modes are shown in Fig. 4.4b)-d),f)-h). Note that thermal noise spectral density, g_0 and C_{eff} are independent on the reference magnetic field driving direction, while c_{act} strongly relies on the driven direction dependent mode overlap.

The discrepancy between numerical simulation and experimental results [27, 32] of the eigenfrequency of the most sensitive mechanical mode driven with in-plane magnetic field signal mainly lies in the value of input elasticity matrix elements, which share matrix relation with Young's Modulus, Poisson's ratio and piezomagnetic constants, rely strongly on operation conditions including initial mechanical prestress, DC bias magnetic field, external load, temperature, and external driving magnetic field [68, 69]. With high repeatable sputter coating method and elasticity measurement technique under experimental condition rather than use literature parameters, the eigenfrequency mismatch would be solved.

4.3 The effects of laser detuning and power on bandwidth

The mechanical mode at $\Omega_M/2\pi$=27 MHz is further chosen for analysis of the influence of bandwidth as a result of laser power variation and detuning ($\Delta = \omega_0 - \omega_L$). Bandwidth is defined as a 3 dB decay of the minimum detectable magnetic field from the mechanical resonance. Laser detuning would change the mechanical damping as well as mechanical resonance frequencies (refer to Eq.(2.19)) physically due to a delay (caused by finite κ) for the photon to meet the new boundary condition created by the oscillation mechanics termed as dynamical back-action [50, 49]. Input laser power is controlled below 20 μW for blue detuning when $\Delta = -\kappa$ as further cranking the laser power would cause instability ($\Gamma < 0$). Both red $\Delta = \kappa$ and blue detuning has the same effect on bandwidth and sensitivity as shown in Fig. 4.5. The bandwidth saturates with the increasing laser power due to the presence of the neighbouring thermal noise (peak at $\Omega_M/2\pi = 26$ MHz and 43 MHz in Fig. 4.4a)). For linear oscillators, sensitivity doesn't benefit from cooling or heating with increasing laser power

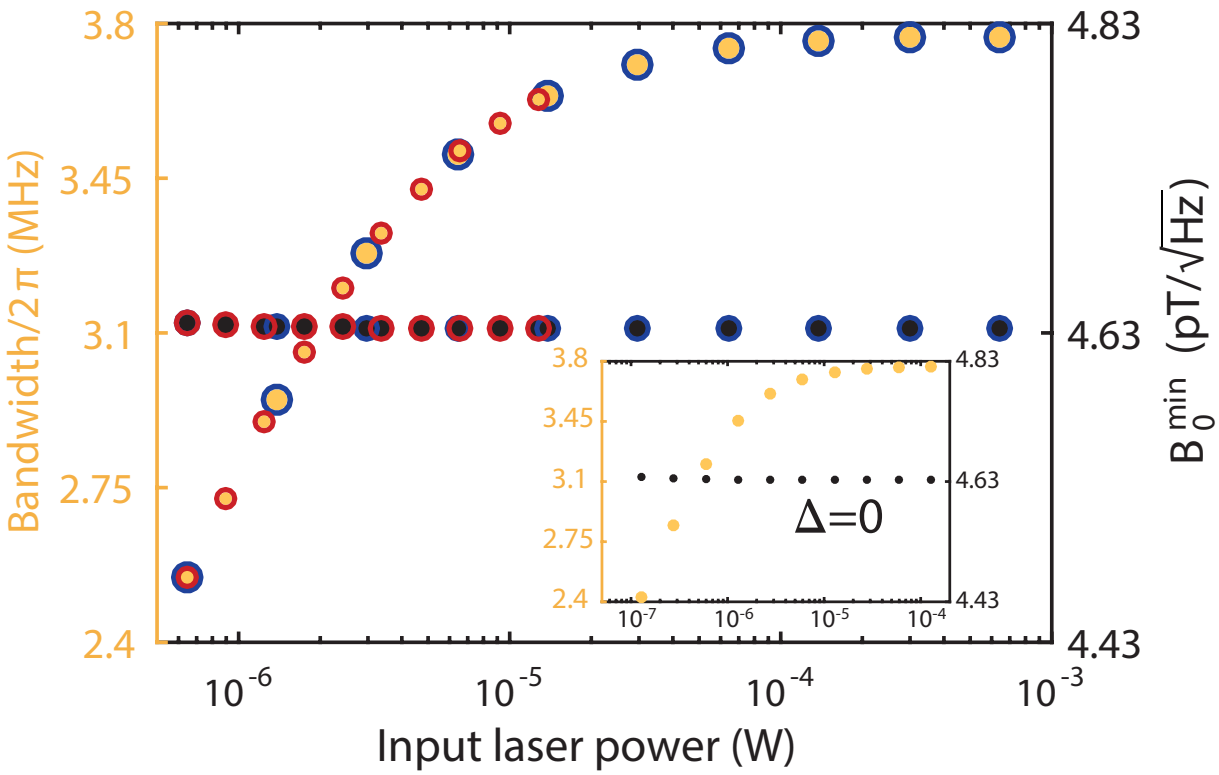

Fig. 4.5 **The effect of laser detuning from optical cavity and power on bandwidth and sensitivity** Dots with blue edges represent for cooling with the red detuned factor $\Delta = \kappa$, while red edges of those are for heating effect when the laser is blue detuned $\Delta = -\kappa$. Input laser power larger than 20 μW would cause instability due to heating effects. Locking the laser on optical resonance frequency with the input power 5 times smaller than in the detuning $\Delta = \pm\kappa$ cases results the same bandwidth increasing trend as shown in the inset.

as the action of feedback, equivalent to filtering, prevents the enhancement in sensitivity [70], with which our sensitivity plot as a function of laser power agrees. Lock the laser on optical resonance frequency and set the power to be 5 times smaller than in the case when the detuning factor is set to be $\Delta = \pm\kappa$ ensures the same amount of intra-cavity photon numbers (Eq. (2.13)). This in turn results the same bandwidth increasing trend as shown in the inset of Fig. 4.5. This result demonstrates that the increase of bandwidth relies on the input laser power which can be implemented both in detuned and on resonance manner.

A few MHz bandwidth is reachable within one single mechanical mode, which is quite impressive for micro optical magnetometers of $\mathrm{pT}/\sqrt{\mathrm{Hz}}$ sensitivity operated at room temperature. Large bandwidth enables faster readout of NMR signals of different materials with the frequency separation of their fingerprints. If the Lamor frequency is polarized to the best sensitivity region of our magnetometer ~ 20 MHz and with MHz bandwidth, the chemical contrast NMR signal of ^{19}F and ^{1}H in ref. [71] can be read out simultaneously rather than using multiple microwave pulse sequences to map the signals as the operational scheme from nitrogen-vacancy centres based magnetometers.

Chapter 5

Conclusion and Outlook

5.1 Conclusion

To summarize, by implementing the linear constitutional stress-magnetic field relation of magnetostrictive materials as external stress into the elastic wave equation, together with magnetic fields with changeable directions, as modelled by a pair of Helmholtz coils in COMSOL, sensitivity for magnetometers with geometries both experimentally demonstrated and not-yet fabricated have been predicted. The sensitivity from the modelling is within one order of magnitude better than the experimental result [32], showing the potential for improvement. With the help of highly repeatable sputter coated fabrication of Terfenol-D as well as measurements of the elasticity matrix elements and piezomagnetic constants, we expect the method developed here to accurate predict both in terms of the sensitivity and frequency response of optomechanical magnetometers.

Possible ways to improve the sensitivity of optomechanical magnetometers are to increase the size of the Terfenol-D and to use the bending effect which arises from a magnetic equivalent of the bimetallic strip effect. The bandwidth can be broadened by increasing the laser power on resonance and using the optomechanical dynamic back-action which arises from detuning the laser from cavity resonance.

5.2 Outlook

The method developed here is applicable to other geometries of magnetostrictive material based optomechanical magnetometers, and can be extended to include quantum noise analysis for quantum enhanced optomechanical sensors [14].

A full characterization of the response of magnetomechanical coupling to the variation of reference magnetic fields direction may allow vectorial optomechanical magnetometry, as complementary to the vectorical optomechanical force sensors [72, 73]. In ref. [73] the vectorial force sensor is realized by using two orthogonal quasi-frequency-degenerate mechanical modes in a one-dimensional nanowire. The direction of the force signal alters the ratio of the thermal noise peaks and the eigenfrequency of the two nearly degenerated mechanical modes. A full characterization of the variations of the force vector in two dimensions gives a thermal noise peak ratio map, which could serve as a reference for force signals to be measured. In our case, the magnetomechanical coupling changes the height

of the signal peak under driving. We could use two or more mechanical eigenmodes as references, and fully characterize how their peak changes under a reference magnetic field as a function of field direction. In this way, a 4π solid angle might be achievable due to the combinational response at multiple eigenfrequencies.

Optimizations of the Terfenol-D annealing process may lead to sensitivity below 500 $\mathrm{fT}/\sqrt{\mathrm{Hz}}$, given the axial piezomagnetic constant used (10.4 nm/A) is still 30 times smaller than in ref. [54] (6.3 nm/A-310 nm/A). To test the nonlinear stress-magnetic field behaviour of optomechanical field magnetometer where Terfenol-D is operated near saturated strain $\varepsilon_{\mathrm{max}}$, numerical methods such as ref. [48] can be implemented with optomechanical analysis. Micro-optomechanical field magnetometers with $\mathrm{pT}/\sqrt{\mathrm{Hz}}$ sensitivity can be applied to detect signals from micrometre neurons similar to recent results with nitrogen-vacancy centres based magnetometers [23] and atomic magnetometer [74], but with benefits of a simpler and energy-saving scheme, as well as a large bandwidth capacity.

References

[1] W. L. Webb. Aircraft navigation instruments. *Electrical Engineering*, 70(5):384–389, 1951.

[2] M. Diaz-Michelena. Small magnetic sensors for space applications. *Sensors (Basel)*, 9(4):2271–88, 2009.

[3] Matti Hämäläinen, Riitta Hari, Risto J. Ilmoniemi, Jukka Knuutila, and Olli V. Lounasmaa. Magnetoencephalography—theory, instrumentation, and applications to noninvasive studies of the working human brain. *Reviews of Modern Physics*, 65(2):413–497, 1993.

[4] A. Mehlin, F. Xue, D. Liang, H. F. Du, M. J. Stolt, S. Jin, M. L. Tian, and M. Poggio. Stabilized skyrmion phase detected in mnsi nanowires by dynamic cantilever magnetometry. *Nano Lett*, 15(7):4839–44, 2015.

[5] K. V. R. Chary and Girjesh Govil. *NMR in Biological Systems-From Molecules to Humans*. Focus on Structural Biology 6. Springer, the Netherlands, 2008.

[6] L. M. K. Vandersypen and I. L. Chuang. Nmr techniques for quantum control and computation. *Reviews of Modern Physics*, 76:1037–1069, 2004.

[7] Asaf Grosz, Michael J. Haji-Sheikh, and Subhas C. Mukhopadhyay, editors. *High Sensitivity Magnetometers*, volume 19 of *Smart Sensors, Measurement and Instrumentation*. Springer International Publishing, 2017.

[8] M. Simmonds, W. Fertig, and R. Giffard. Performance of a resonant input squid amplifier system. *IEEE Transactions on Magnetics*, 15(1):478–481, Jan 1979.

[9] A. Guedes, J. M. Almeida, S. Cardoso, R. Ferreira, and P. P. Freitas. Improving magnetic field detection limits of spin valve sensors using magnetic flux guide concentrators. *IEEE Transactions on Magnetics*, 43(6):2376–2378, 2007.

[10] A. Persson, R. S. Bejhed, F. W. Østerberg, K. Gunnarsson, H. Nguyen, G. Rizzi, M. F. Hansen, and P. Svedlindh. Modelling and design of planar hall effect bridge sensors for low-frequency applications. *Sensors and Actuators A: Physical*, 189:459–465, 2013.

[11] C. C. Lu, J. Huang, P. K. Chiu, S. L. Chiu, and J. T. Jeng. High-sensitivity low-noise miniature fluxgate magnetometers using a flip chip conceptual design. *Sensors (Basel)*, 14(8):13815–29, 2014.

[12] Slawomir Tumanski. Induction coil sensors—a review. *Measurement Science and Technology*, 18(3):R31–R46, 2007.

[13] R.J. Prance, T.D. Clark, and H. Prance. Ultra low noise induction magnetometer for variable temperature operation. *Sensors and Actuators A: Physical*, 85(1–3):361 – 364, 2000.

[14] C. L. Degen, F. Reinhard, and P. Cappellaro. Quantum sensing. *arXiv:1611.02427v1*, 2016.

[15] J. R. Kirtley, M. B. Ketchen, K. G. Stawiasz, J. Z. Sun, W. J. Gallagher, S. H. Blanton, and S. J. Wind. High-resolution scanning squid microscope. *Applied Physics Letters*, 66(9):1138–1140, 1995.

[16] F. Baudenbacher, L. E. Fong, J. R. Holzer, and M. Radparvar. Monolithic low-transition-temperature superconducting magnetometers for high resolution imaging magnetic fields of room temperature samples. *Applied Physics Letters*, 82(20):3487, 2003.

[17] W. Clark Griffith, Svenja Knappe, and John Kitching. Femtotesla atomic magnetometry in a microfabricated vapor cell. *Optics Express*, 18(26):27167–27172, 2010.

[18] M. S. Grinolds, S. Hong, P. Maletinsky, L. Luan, M. D. Lukin, R. L. Walsworth, and A. Yacoby. Nanoscale magnetic imaging of a single electron spin under ambient conditions. *Nature Physics*, 9(4):215–219, 2013.

[19] Fazhan Shi, Qi Zhang, Pengfei Wang, Hongbin Sun, Jiarong Wang, Xing Rong, Ming Chen, Chenyong Ju, Friedemann Reinhard, Hongwei Chen, Jörg Wrachtrup, JunfengWang, and Jiangfeng Du. Single-protein spin resonance spectroscopy under ambient conditions. *Science*, 347(6226):4, 2015.

[20] I. Lovchinsky, A. O. Sushkov, E. Urbach, N. P. de Leon, S. Choi, K. De Greve, R. Evans, R. Gertner, E. Bersin, C. Müller, L. McGuinness, F. Jelezko, R. L. Walsworth, H. Park, and M. D. Lukin. Nuclear magnetic resonance detection and spectroscopy of single proteins using quantum logic. *Science*, 2016.

[21] A. O. Sushkov, I. Lovchinsky, N. Chisholm, R. L. Walsworth, H. Park, and M. D. Lukin. Magnetic resonance detection of individual proton spins using quantum reporters. *Phys Rev Lett*, 113(19):197601, 2014.

[22] Thomas Wolf, Philipp Neumann, Kazuo Nakamura, Hitoshi Sumiya, Takeshi Ohshima, Junichi Isoya, and Jörg Wrachtrup. Subpicotesla diamond magnetometry. *Physical Review X*, 5(4), 2015.

[23] J. F. Barry, M. J. Turner, J. M. Schloss, D. R. Glenn, Y. Song, M. D. Lukin, H. Park, and R. L. Walsworth. Optical magnetic detection of single-neuron action potentials using quantum defects in diamond. *Proc Natl Acad Sci USA*, 113(49):14133–14138, 2016.

[24] P. Kehayias, A. Jarmola, N. Mosavian, I. Fescenko, F. M. Benito, A. Laraoui, J. Smits, L. Bougas, D. Budker, A. Neumann, S. R. J. Brueck, and V. M. Acosta. Solution nuclear magnetic resonance spectroscopy on a nanostructured diamond chip. *ArXiv: 1701.01401v1*, 2017.

[25] Chang S. Shin, Claudia E. Avalos, Mark C. Butler, David R. Trease, Scott J. Seltzer, J. Peter Mustonen, Daniel J. Kennedy, Victor M. Acosta, Dmitry Budker, Alexander Pines, and Vikram S. Bajaj. Room-temperature operation of a radiofrequency diamond magnetometer near the shot-noise limit. *Journal of Applied Physics*, 112(12):124519, 2012.

[26] S. Forstner, S. Prams, J. Knittel, E. D. van Ooijen, J. D. Swaim, G. I. Harris, A. Szorkovszky, W. P. Bowen, and H. Rubinsztein-Dunlop. Cavity optomechanical magnetometer. *Physical Review Letters*, 108(12), 2012.

[27] S. Forstner, E. Sheridan, J. Knittel, C. L. Humphreys, G. A. Brawley, H. Rubinsztein-Dunlop, and W. P. Bowen. Ultrasensitive optomechanical magnetometry. *Adv Mater*, 26(36):6348–53, 2014.

[28] T. J. Kippenberg, H. Rokhsari, T. Carmon, A. Scherer, and K. J. Vahala. Analysis of radiation-pressure induced mechanical oscillation of an optical microcavity. *Phys Rev Lett*, 95(3):033901, 2005.

[29] D. Rugar, R. Budakian, H. J. Mamin, and B. W. Chui. Single spin detection by magnetic resonance force microscopy. *Nature*, 430(6997):329–332, 2004. 10.1038/nature02658.

[30] Marcelo Wu, Nathanael L. Y. Wu, Tayyaba Firdous, Fatemeh Fani Sani, Joseph E. Losby, Mark R. Freeman, and Paul E. Barclay. Nanocavity optomechanical torque magnetometry and radiofrequency susceptometry. *Nature Nanotechnology*, 2016.

[31] W. Muessel, H. Strobel, D. Linnemann, D. B. Hume, and M. K Oberthaler. Scalable spin squeezing for quantum-enhanced magnetometry with bose einstein condensates. *Phys Rev Lett*, 2014.

[32] Beibei Li, Eoin Sheridan, Stefan Forstner, Halina Rubinsztein-Dunlop, and Warwick Bowen. Ultrasensitive cavity optomechanical magnetometry. In *Conference on Lasers and Electro-Optics*, page STu1E.8. Optical Society of America, 2016.

[33] Xufeng Zhang, Chang-Ling Zou, Liang Jiang, and Hong X. Tang. Cavity magnomechanics. *Science Advances*, 2016.

[34] S. Forstner, J. Knittel, H. Rubinsztein-Dunlop, and W. P. Bowen. Model of a microtoroidal magnetometer. In Francis Berghmans and Anna Grazia Mignani, editors, *SPIE Proceedings: Optical Sensing and Detection II*, volume 8439, 2012.

[35] Stefan Forstner, Joachim Knittel, Eoin Sheridan, Jon D. Swaim, Halina Rubinsztein-Dunlop, and Warwick P. Bowen. Sensitivity and performance of cavity optomechanical field sensors. *Photonic Sensors*, 2(3):259–270, 2012.

[36] L. D. Landau and E. M. Lifshitz. *Theroy of Elasticity*, volume 7 of *Course of therotical physics*. Pergamon Press, 3rd edition, 1986.

[37] G. Engdahl. *Handbook of Giant Magnetostrictive Materials*. Academic Press, 1999.

[38] Jonathan G. Benatar. *FEM implementations of magnetostrictive-based applications*. Masters thesis, University of Maryland, 2005.

[39] Kidambi S. Kannan. *Galerkin finite element scheme for magnetostrictive structures and composites*. Phd thesis, University of Maryland, 1997.

[40] X. J. Zheng and X. E. Liu. A nonlinear constitutive model for terfenol-d rods. *Journal of Applied Physics*, 97(5):053901, 2005.

[41] F. Claeyssen, N. Lhermet, R. Le Letty, and P. Bouchilloux. Actuators, transducers and motors based on giant magnetostrictive materials. *Journal of Alloys and Compounds*, 258(1):61 – 73, 1997.

[42] E. Quandt. Giant magnetostrictive thin film materials and applications. *Journal of Alloys and Compounds*, 258:126–132, 1997.

[43] Marcelo J. Dapino, Ralph C. Smith, and Alison B. Flatau. Structural magnetic strain model for magnetostrictive transducers. *IEEE TRANSACTIONS ON MAGNETICS*, 36(3), 2000.

[44] J. H. Yoo and A. B. Flatau. A bending-mode galfenol electric power harvester. *Journal of Intelligent Material Systems and Structures*, 23(6):647–654, 2012.

[45] Arthur E. Clark, Marilyn Wun-Fogle, James B. Restorff, and Thomas A. Lograsso. Magnetostrictive properties of galfenol alloys under compressive stress. *MATERIALS TRANSACTIONS*, 43(5):881–886, 2002.

[46] J. P. Domann, C. M. Loeffler, B. E. Martin, and G. P. Carman. High strain-rate magnetoelasticity in galfenol. *Journal of Applied Physics*, 118(12):123904, 2015.

[47] P. R. Downey and A. B. Flatau. Magnetoelastic bending of galfenol for sensor applications. *Journal of Applied Physics*, 97(10):10R505, 2005.

[48] Suryarghya Chakrabarti. *Modeling of 3D Magnetostrictive Systems with Application to Galfenol and Terfenol-D Transducers*. Thesis, Ohio State University, 2011.

[49] W. Bowen and G. Milburn. *Quantum Optomechanics*. CRC, 2015.

[50] Markus Aspelmeyer, Tobias J. Kippenberg, and Florian Marquardt. Cavity optomechanics. *Reviews of Modern Physics*, 86(4):1391–1452, 2014.

[51] H.-A. Bachor and T. C. Ralph. *Quantum Noise Transfer Functions: A Practical Tool in Quantum Optics. Directions in Quantum Optics*. Springer, 1999.

[52] Warwick Bowen. *Experiments towards a Quantum Information Network with Squeezed Light and Entanglement*. Phd thesis, Australia National University, 2003.

[53] K. H. Lee, T. G. McRae, G. I. Harris, J. Knittel, and W. P. Bowen. Cooling and control of a cavity optoelectromechanical system. *Phys. Rev. Lett.*, 104(12):123604, 2010.

[54] J.D. Verhoeven, E.D. Gibson, O.D. Mcmasters, and J.E. Ostenson. Directional solidification and heat treatment of terfenoi-d magnetostrictive materials. *Metallurgical Transactions A*, 21A:2249–2255, 1990.

[55] David J. Griffiths. *Introduction to Electrodynamics*. Prentice Hall International. Inc., 3rd edition, 1999.

[56] F. Claeyssen, R. Bossut, and D. Boucher. Modeling and characterization of the magnetostrictive coupling. In B. F. Hamonic et al, editor, *Power Transducers for Sonics and Ultrasonics*, pages 132–151. Springer-Verlag Berlin Heidelberg, 1991.

[57] John Buck William Hayt. *Engineering Electromagnetics, 8th Edition*. McGraw-Hill, 2011.

[58] Simon Groeblacher. *Quantum opto-mechanics with micromirrors: combining nano-mechanics with quantum optics*. Thesis, University of Vienna, 2010.

[59] B. D. Hauer, C. Doolin, K. S. D. Beach, and J. P. Davis. A general procedure for thermomechanical calibration of nano/micro-mechanical resonators. *Annals of Physics*, 339:181–207, 2013.

[60] G. A. Brawley, M. R. Vanner, P. E. Larsen, S. Schmid, A. Boisen, and W. P. Bowen. Nonlinear optomechanical measurement of mechanical motion. *Nature Communication*, 7:10988, 2016.

[61] Rick Leijssen, Giada La Gala, Lars Freisem, Juha T. Muhonen, and Ewold Verhagen. Nonlinear cavity optomechanics with nanomechanical thermal fluctuations. *ArXiv:1612.08072*, 2016.

[62] Morio Onoe. Contour vibrations of isotropic circular plates. *The Journal of the Acoustical Society of America*, 28(6):1158–1162, 1956.

[63] Christopher Baker. *On-chip nano-optomechanical whispering gallery resonators*. Thesis, Universite Paris-Diderot - Paris VII, 2013.

[64] Haojiang Ding, Weiqiu Chen, and L. Zhang. *Elasticity of Transversely Isotropic Materials*, volume 126 of *Solid Mechanics and It's Applications*. Springer, 2006.

[65] D. J. Wilson, V. Sudhir, N. Piro, R. Schilling, A. Ghadimi, and T. J. Kippenberg. Measurement-based control of a mechanical oscillator at its thermal decoherence rate. *Nature*, 524(7565):325–9, 2015.

[66] A. Schliesser, G. Anetsberger, R. Rivière, O. Arcizet, and T. J. Kippenberg. High-sensitivity monitoring of micromechanical vibration using optical whispering gallery mode resonators. *New Journal of Physics*, 10(9):095015, 2008.

[67] T. J. Kippenberg, S. M. Spillane, and K. J. Vahala. Modal coupling in traveling-wave resonators. *Optics Letter*, 19(27):1669, 2002.

[68] M.J. Dapino, A.B. Flatau, and F.T. Calkins. Statistical analysis of terfenol-d material properties. *Journal of intelligent material systems and structures*, 17(7):587–599, 2006.

[69] R. Kellogg and A. Flatau. Experimental investigation of terfenol-d's elastic modulus. *Journal of Intelligent Material Systems and Structures*, 19(5):583–595, 2007.

[70] G. I. Harris, D. L. McAuslan, T. M. Stace, A. C. Doherty, and W. P. Bowen. Minimum requirements for feedback enhanced force sensing. *Phys Rev Lett*, 111(10):103603, 2013.

[71] T. Haberle, D. Schmid-Lorch, F. Reinhard, and J. Wrachtrup. Nanoscale nuclear magnetic imaging with chemical contrast. *Nat Nanotechnol*, 10(2):125–8, 2015.

[72] N. Rossi, F. R. Braakman, D. Cadeddu, D. Vasyukov, G. Tutuncuoglu, I. Morral A. Fontcuberta, and M. Poggio. Vectorial scanning force microscopy using a nanowire sensor. *Nat Nanotechnol*, 2016.

[73] L. M. de Lepinay, B. Pigeau, B. Besga, P. Vincent, P. Poncharal, and O. Arcizet. A universal and ultrasensitive vectorial nanomechanical sensor for imaging 2d force fields. *Nat Nanotechnol*, 2016.

[74] K. Jensen, R. Budvytyte, R. A. Thomas, T. Wang, A. M. Fuchs, M. V. Balabas, G. Vasilakis, L. D. Mosgaard, H. C. Staerkind, J. H. Muller, T. Heimburg, S. P. Olesen, and E. S. Polzik. Non-invasive detection of animal nerve impulses with an atomic magnetometer operating near quantum limited sensitivity. *Sci Rep*, 6:29638, 2016.

[75] Kaihua Zhao and Ximou Chen. *Electromagnetism (in Chinese)*, volume 3 of *New concept physics*. Higher Education Press, 2003.

Appendix A: Input parameters and variables to COMSOL

Table 1 **Input global parameters to COMSOL**

Name	Value [unit]	Description
I0	1.25e-3[A]	Coil current
theta0	0[deg]	Coil direction
ch11	10.7e10[Pa]	Elasticity matrix element 11
ch12	7.48e10[Pa]	12
ch13	8.21e10[Pa]	13
ch33	9.81e10[Pa]	33
ch44	0.6e10[Pa]	44
ch66	1.61e10[Pa]	66
e31	-0.9e2[Pa*m/A]	magnetostrictive coefficent 31
e33	1.66e2[T]	33
e15	1.68e2[T]	15
mu0	4*pi e-7 [N/A^2]	vacuum permeability
muT11	6.9*mu0 [N/A^2]	relative permeability matrix element 11
muT33	4.4*mu0 [N/A^2]	33
f	0[Hz]	sweeping frequency

Table 2 **Input variables to COMSOL**

Name	Expression [Pa]
sigma1	e31*mf.Hz+mf.Hx*mf.Bx-0.5/mu0*(mf.Bx*mf.Bx+mf.By*mf.By+mf.Bz*mf.Bz)
sigma2	e31*mf.Hz+mf.Hy*mf.By-0.5/mu0*(mf.Bx*mf.Bx+mf.By*mf.By+mf.Bz*mf.Bz)
sigma3	e33*mf.Hz+mf.Hz*mf.Bz-0.5/mu0*(mf.Bx*mf.Bx+mf.By*mf.By+mf.Bz*mf.Bz)
sigma4	e15*mf.Hy+mf.Hy*mf.Bz
sigma5	e15*mf.Hx+mf.Hx*mf.Bz
sigma6	mf.Hx*mf.By

Appendix B: Magnetic Field Inside Magnets

The magnetic current and dipole models for insight into the magnetic field inside ferromagnet is based on textbook [75].

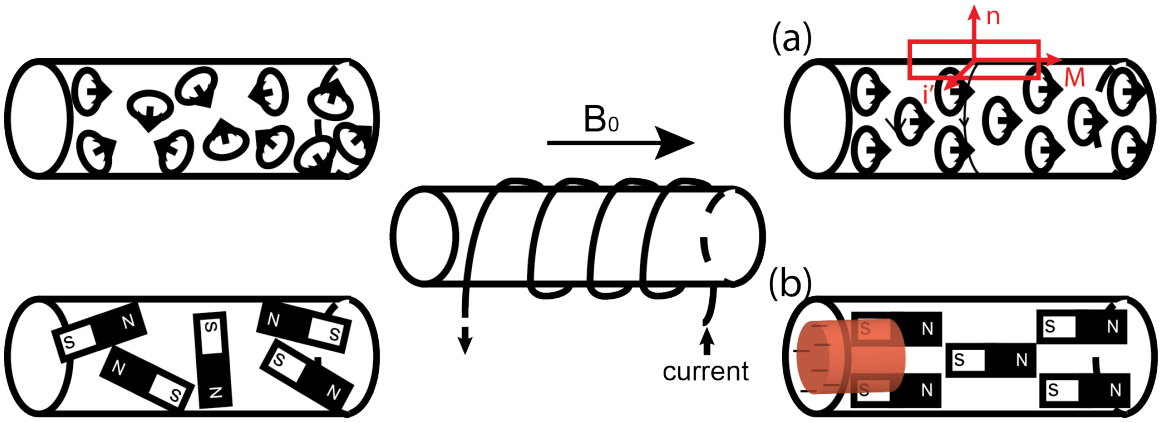

Fig. 1 **Magnetic field inside a magnet rod using textbook toy models of magnetic current and magnetic dipole.** After applying an external magnetic field B_0 from a current flowing solenoid, **(a)** the aligned magnetic current ensemble shows a total effect equivalent to circular current around the edge (a thin line in the middle) in the magnetic current model. **(b)** In the magnetic dipole model, the total effect of applying $\boldsymbol{B}_0$ is equal to creating negative and positive magnetic charges on the left and right side surfaces of the magnet.

Magnetic current point of view

From **magnetic current point of view**, the total magnetic field strength $\boldsymbol{B}$ inside the cylindrical magnetic rod as shown in Fig. 1a) is

$$\boldsymbol{B} = \boldsymbol{B}_0 + \boldsymbol{B}' \tag{1}$$

where $\boldsymbol{B}_0$ is the external magnetic field strength and $\boldsymbol{B}'$ is the additional magnetic field strength resulting from the alignment of the magnetic currents. This alignment cancels the current loops inside the magnet leaving only the current flowing around the edges of the cylinder displayed as a thin line in the middle of the cylinder in Fig. 1a). Defining magnetization vector $\boldsymbol{M}$ as $\boldsymbol{M} = nI\boldsymbol{a}$, where n is the density of the current loops, $\boldsymbol{a}$ is the loop covered area and I is the current of each tiny loops. Given a close path with length of Δl and negligible height across the magnet edge as shown in the red rectangle

in Fig. 1a), the integration of $\boldsymbol{M}$ along the closed path L across multiple current loops leads to

$$\oint_L \boldsymbol{M} \cdot \mathrm{d}\boldsymbol{l} = \sum_{\text{inside L}} \boldsymbol{I}' \tag{2}$$

in which $\boldsymbol{I}' = \boldsymbol{i}'\Delta l$ with $\boldsymbol{i}'$ being the surface current density at the edge of the magnet cylinder. The integrand is only none zero inside the magnet, written as a vectorial equation:

$$\boldsymbol{M} \times \boldsymbol{n} = \boldsymbol{i}'. \tag{3}$$

$\boldsymbol{B}'$ at the centre of the magnet can be calculated as the magnetic field created by a solenoid with current density of $\boldsymbol{M}$ as

$$\boldsymbol{B}' = \mu_0 \boldsymbol{M} \frac{l/d}{\sqrt{1+(l/d)^2}} \tag{4}$$

with $2l$ and d being the length and diameter of the magnet rod.

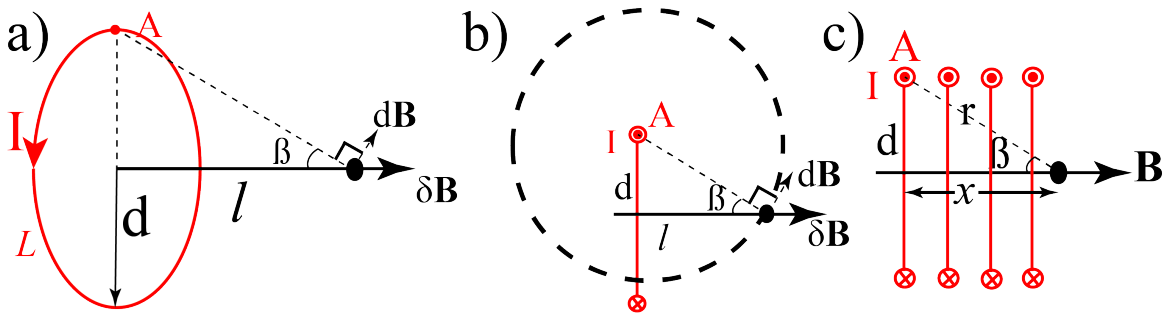

Fig. 2 **The calculation scheme of the magnetic field in the axial direction of a single current loop and solenoid. a)** The current at position A creates a magnetic field d$\boldsymbol{B}$ at the location • on the horizontal axis. The current in a single loop generates a magnetic field $\delta\boldsymbol{B}$. **b)** The direction of the magnetic field d$\boldsymbol{B}$ is clarified where the single current loop is viewed from a front angle. Note that the scale of the red loop shrinks a bit. **c)** A solenoid is modelled as as array of single current loops along the axial direction. The array produces a magnetic field $\boldsymbol{B}$ on the axis x distance away.

Note that the magnetic field created by a solenoid above is calculated first from the contribution from a single current loop with a current density $\boldsymbol{I}$ and a circumference L as shown in Fig. 2a)-b) by applying Biot-Savart law as

$$\delta\boldsymbol{B} = \oint \mathrm{d}\boldsymbol{B} \cdot \cos\beta = \frac{\mu_0}{4\pi} \cdot \frac{\boldsymbol{I}\mathrm{d}L}{l^2} \cos^2\beta \sin\beta \int \mathrm{d}L = \frac{\mu_0 d^2 \boldsymbol{I}}{2(d^2+l^2)^{3/2}} \tag{5}$$

where d is the radius of a loop and l is the distance between the loop centre and the observation point. The sum of the contributions from an array of single current loops is

$$\boldsymbol{B} = \int_{-l}^{l} \frac{\mu_0 d^2 \boldsymbol{I}}{2(d^2+x^2)^{3/2}} \mathrm{d}x = \frac{\mu_0 \boldsymbol{I}}{2} \int_{\beta_1}^{\beta_2} \sin\beta \mathrm{d}\beta = \frac{\mu_0 \boldsymbol{I}}{2}(\cos\beta_1 - \cos\beta_2) \tag{6}$$

where the relation shown in Fig. 2c) $r^2 = x^2 + d^2$ and $x/d = \cot\beta$, as well as the differentiation $\mathrm{d}x/d = \mathrm{d}\beta/\sin^2\beta$ are used. At the centre of a solenoid, β_1, β_2 have the relation of

$$\cos\beta_1 = \frac{l}{\sqrt{d^2+l^2}},\ \cos\beta_2 = -\frac{l}{\sqrt{d^2+l^2}}. \tag{7}$$

Therefore, the total magnetic field $\boldsymbol{B}$ at the centre of the solenoid has the expression of

$$\boldsymbol{B} = \mu_0 \boldsymbol{I} \frac{l/d}{\sqrt{1+(l/d)^2}}. \tag{8}$$

Magnetic dipole point of view

In light of **magnetic dipole point of view**, the total magnetic field $\boldsymbol{H}$ inside a magnet rod is the vector sum of the external magnetic field and the polarized magnetic field as

$$\boldsymbol{H} = \boldsymbol{H}_0 + \boldsymbol{H}'. \tag{9}$$

As shown in Fig. 1b), we assume the direction of the external magnetic field pointing to the right, then the effect of all aligned tiny magnets equals to the distribution of negative magnetic charge on the left surface and positive on the right. This magnetic charge distribution creates a magnetized field $\boldsymbol{H}'$ in opposite direction to the external magnetic field. Therefore, $\boldsymbol{H}'$ is also termed as demagnetization field. According to Coulomb's law, $\boldsymbol{H}'$ at the axial centre with magnetic charge density of σ_m on each surfaces is first calculated through one circular surface shown as in Fig. 3. The magnetic field generated by an area ds at the location A from the charged surface detected on the axis l distance away fro the centre of the surface is

$$\mathrm{d}\boldsymbol{H} = \frac{1}{4\pi\mu_0} \cdot \frac{\sigma_m}{l^2+r^2} \cdot \mathrm{d}s. \tag{10}$$

For the convenience of integration, ds is chosen to be the area of a ring r distance away from the centre of the charged circular plate. The magnetic field from ds then is

$$\delta\boldsymbol{H} = \frac{1}{4\pi\mu_0} \cdot \frac{\sigma_m}{l^2+r^2} \cdot \frac{2\pi l \mathrm{d}r}{\sqrt{l^2+r^2}}. \tag{11}$$

The magnetic field contributed from the whole circular plate to a specific location on the axis is the integral over the radius of the plate as

$$\boldsymbol{H} = \frac{2\pi l\sigma_m}{4\pi\mu_0} \int_0^d \frac{r\mathrm{d}r}{(l^2+r^2)^{3/2}} = \frac{\sigma_m}{2\mu_0}\left(1 - \frac{1}{\sqrt{l^2+d^2}}\right). \tag{12}$$

Adding another magnetically charged circular plate on the other side with opposite charges is equivalent to multiplying a factor of 2 in Eq.(12).

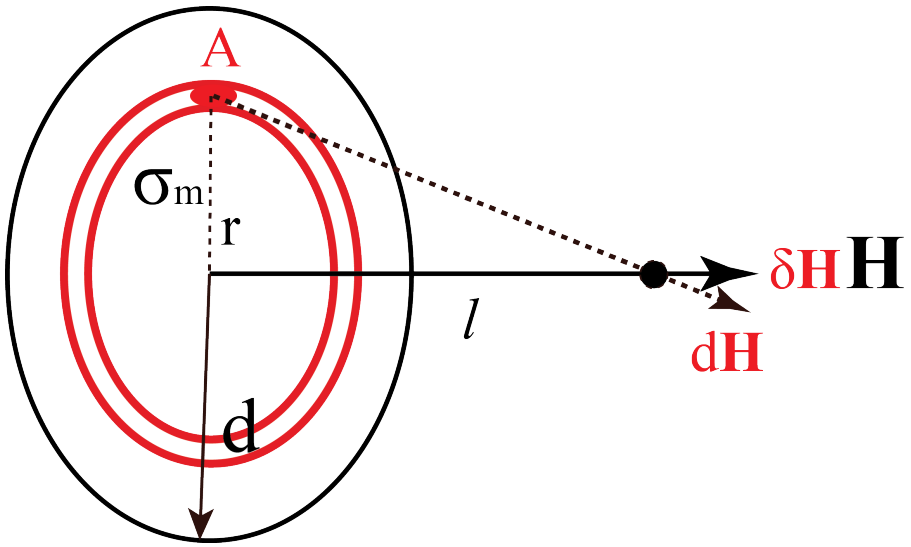

Fig. 3 **Magnetic field in the axial direction of a magnetically charge circular plate.**

The relationship between the magnetic charge density σ_m and magnetization $\boldsymbol{J}$ can be derived from Gauss's law, where $\boldsymbol{J}$ is defined as volume averaged vector sum of magnetic dipole momentum. Similar to Gauss's law for electric charges, a closed surface integral of magnetization $\boldsymbol{J}$ equals to the magnetic charges inside the surface.

$$\oiint_s \boldsymbol{J} \cdot \mathrm{d}\boldsymbol{s} = -\sum_s q_\mathrm{m} = \oiint_s \sigma_\mathrm{m} \mathrm{d}\boldsymbol{s}, \tag{13}$$

which results the relation $\sigma_\mathrm{m} = \boldsymbol{J}\cos\theta$.

Replacing $\boldsymbol{J}$ with the expression of σ_m for Eq.(12) results in

$$\boldsymbol{H}' = \frac{\boldsymbol{J}}{\mu_0}\left[1 - \frac{l/d}{\sqrt{1+(l/d)^2}}\right] \equiv \frac{\boldsymbol{J}\mathrm{N_D}}{\mu_0} \tag{14}$$

in which $\mathrm{N_D}$ is a geometry dependent demagnetization factor having a value between 0 and 1. Generally speaking, $\mathrm{N_D}$ is a tensor for 3D object.

From Eq. (4) and Eq. (14), the link between the magnetic current and magnetic dipole models can be drawn as

$$\boldsymbol{H}' = \boldsymbol{M} - \frac{\boldsymbol{B}'}{\mu_0}. \tag{15}$$

Link between the two models and the resulting internal external magnetic field relation

Given the ad hoc assumption for the magnetization defined from magnetic current and dipole point of views as

$$\boldsymbol{J} = \mu_0 \boldsymbol{M} \tag{16}$$

the $\boldsymbol{B}$-$\boldsymbol{H}$ relation for both magnetic current and magnetic dipole models becomes

$$\boldsymbol{B} = \mu_0(\boldsymbol{H} + \boldsymbol{M}) = \mu_0 \boldsymbol{H} + \boldsymbol{J}. \tag{17}$$

With the knowledge of Eq. (14, 15, 16, 17) and the relative permeability in a tensor form defined as

$$\boldsymbol{B} = \mu_0(\boldsymbol{H} + \boldsymbol{M}) \equiv \mu_0 \overline{\overline{\boldsymbol{\mu}}}_r \boldsymbol{H}, \tag{18}$$

the magnetic field inside a magnet can be finally written as

$$\boldsymbol{H} = \frac{\boldsymbol{B}}{\mu_0} - \boldsymbol{M} = \frac{\boldsymbol{B}_0 + \boldsymbol{B}'}{\mu_0} - \boldsymbol{M} = \frac{\boldsymbol{B}_0}{\mu_0} - \boldsymbol{H}' \tag{19}$$

$$= \frac{\boldsymbol{B}_0}{\mu_0} - \frac{\mathrm{N_D} \boldsymbol{J}}{\mu_0} = \frac{\boldsymbol{B}_0}{\mu_0} - \mathrm{N_D} \boldsymbol{M} = \frac{\boldsymbol{B}_0}{\mu_0} - \boldsymbol{H}' - \mathrm{N_D}(\overline{\overline{\boldsymbol{\mu}}}_r - 1)\boldsymbol{H}. \tag{20}$$

Rearranging the internal magnetic field $\boldsymbol{H}$ to one side results in

$$\boldsymbol{H} = \frac{\boldsymbol{B}_0}{\mu_0 \left[\mathrm{N_D}(\overline{\overline{\boldsymbol{\mu}}}_r - 1) + 1\right]} = \frac{\boldsymbol{H}_0}{\mathrm{N_D}(\overline{\overline{\boldsymbol{\mu}}}_r - 1) + 1} \tag{21}$$

where $\boldsymbol{B}_0$ can be obtained by replacing air with the Terfenol-D at the location of Terfenol-D in numerical simulation. When the magnet is a infinite long rod, $\mathrm{N_D}$ approaches to 0, then the inside magnetic field $\boldsymbol{H}$ equals the external field $\boldsymbol{H}_0$. This is probably the case when the value of the elasticity matrix elements and piezomagnetic constants are measured in the literature [41] from which we take the value. For thin film structure, $\mathrm{N_D}$=1 for the extreme case when the thickness is 0. This results the internal magnetic field to be

$$\boldsymbol{H}_{\text{thin film}} = \frac{\boldsymbol{H}_0}{\overline{\overline{\boldsymbol{\mu}}}_r}. \tag{22}$$

Magnetic field inside Terfenol-D in the numerical simulation is checked by the value from several selected points in Terfenol-D with Eq. (21), showing excellent agreement with the simulation results from COMSOL.